NIST Technical Note
NIST TN 2267

Fire Resilience of a Steel-Concrete Composite Floor System: Full-Scale Experimental Evaluation for Influence of Slab Reinforcement and Unprotected Secondary Beam (Test #3)

Selvarajah Ramesh
Lisa Choe
Matthew Hoehler
Matthew Bundy
Rodney Bryant
Giovanni Di Cristina Torres
Brian Story
Anthony Chakalis
Artur Chernovsky
Phillip Deardorf
Michael Selepak

This publication is available free of charge from:
https://doi.org/10.6028/NIST.TN.2267

NIST NATIONAL INSTITUTE OF STANDARDS AND TECHNOLOGY
U.S. DEPARTMENT OF COMMERCE

NIST Technical Note
NIST TN 2267

Fire Resilience of a Steel-Concrete Composite Floor System: Full-Scale Experimental Evaluation for Influence of Slab Reinforcement and Unprotected Secondary Beam (Test #3)

Selvarajah Ramesh, Lisa Choe, Matthew Hoehler, Matthew Bundy, Rodney Bryant, Giovanni Torres, Brian Story, Anthony Chakalis, Artur Chernovsky, Phillip Deardorf, Michael Selepak
Fire Research Division
Engineering Laboratory

This publication is available free of charge from:
https://doi.org/10.6028/NIST.TN.2267

October 2023

U.S. Department of Commerce
Gina M. Raimondo, Secretary

National Institute of Standards and Technology
Laurie E. Locascio, NIST Director and Under Secretary of Commerce for Standards and Technology

NIST TN 2267
October 2023

Certain commercial equipment, instruments, software, or materials, commercial or non-commercial, are identified in this paper in order to specify the experimental procedure adequately. Such identification does not imply recommendation or endorsement of any product or service by NIST, nor does it imply that the materials or equipment identified are necessarily the best available for the purpose.

The policy of the National Institute of Standards and Technology is to use metric units in all its published materials. Because this report is intended for the U.S. building construction industry, in some cases U.S. customary units are used.

The policy of the National Institute of Standards and Technology is to include statements of uncertainty with all NIST measurements. In this document, some measurements made by authors outside of NIST are presented, for which uncertainties are not reported and are unknown.

Publication History
Approved by the NIST Editorial Review Board on 2023-09-15

How to Cite this NIST Technical Series Publication
Selvarajah Ramesh, Lisa Choe, Matthew Hoehler, Matthew Bundy, Rodney Bryant, Giovanni Torres, Brian Story, Anthony Chakalis, Artur Chernovsky, Phillip Deardorf, Michael Selepak (2023) Fire Resilience of a Steel-Concrete Composite Floor System: Full-Scale Experimental Evaluation for Influence of Slab Reinforcement and Unprotected Secondary Beam (Test #3). (National Institute of Standards and Technology, Gaithersburg, MD), NIST Technical Note (TN) NIST TN 2267. https://doi.org/10.6028/NIST.TN.2267

NIST Author ORCID iDs
Selvarajah Ramesh: 0000-0002-9525-6767
Lisa Choe: 0000-0003-1951-2746
Matthew Hoehler: 0000-0002-6049-7560
Matthew Bundy: 0000-0002-1138-0307
Rodney Bryant: 0000-0002-5344-9878
Giovanni Torres: 0000-0002-0799-3418

Abstract

The National Fire Research Laboratory at the National Institute of Standards and Technology conducted a series of large compartment fire tests to investigate the behavior and fire-induced failure mechanisms of full-scale composite floor assemblies with a two-story steel gravity frame, two bays by three bays in plan. A total of three 9.1 m × 6.1 m composite floor specimens with varying slab reinforcement and fire protection schemes for the secondary beam were tested under combined mechanical loads and compartment fire exposure. This report presents the experimental design and results from the third composite floor fire experiment (Test #3). The first experiment (Test #1) was designed to achieve a 2-hour fire resistance rating per current U.S. practice and create baseline data for the behavior of the building. Test #1 specimen had the minimum specified reinforcement permitted in the U.S. for the composite slabs with profiled steel decks. Test #2 was conducted to study the effect of enhanced slab reinforcement with larger area and ductility on the fire resilience of the composite floor systems.

Test #3 was conducted to study the effect of enhanced slab reinforcement as well as unprotected secondary beams on the fire resilience of the composite floor systems. Similar to Test #2, the floor slab in the test bay was reinforced with 9.5 mm diameter deformed bars with a center-to-center spacing of 30 cm (230 mm^2/m). Unlike in Test #1 and Test #2, the secondary beam and its end connections in the test bay were left unprotected in Test #3. The test floor was mechanically loaded to 2.7 kPa to mimic the code-prescribed gravity loads for fire conditions. The compartment test fire created upper-layer gas temperatures like those in standard fire resistance tests. A total of four natural gas burners distributed over the compartment floor created a peak gas temperature exceeding 1100 °C below the test floor. A wide transverse crack with flame leak above the floor developed at 132 min in the mid-panel region. The mid-panel vertical displacement reached 535 mm (equivalent to the ratio of L/17 where the span length L = 9.1 m) It reached a peak value of 655 mm (L/14) at 140 min, when the actuator loading was removed. The Test #3 showed that the use of deformed steel bars (230 mm^2/m) for the slab reinforcement maintained the structural integrity of the tested slab longer than the specified rating period with an unprotected secondary beam. The experimental results presented in this report can be used for validation of predictive models to perform parametric studies incorporating the variability in the steel reinforcement scheme (area, spacing, and material) for safer and cost-effective composite floor construction for fire safety.

Keywords

Compartment fire experiments; Composite floors; Fire resistance; Slab reinforcement; Unprotected secondary beam.

Table of Contents

List of Tables

List of Figures

List of Acronyms and Abbreviations

AISC	American Institute of Steel Construction
ASTM	American Society for Testing and Materials
ASCE	American Society of Civil Engineers
ANSI	American National Standards Institute
EC	Eurocode
IBC	International Building Code
ICC	International Code Council
UL	Underwriters Laboratories Inc.
ISO	International Organization for Standardization
NFPA	National Fire Protection Association
NFRL	National Fire Research Laboratory
NIST	National Institute of Standards and Technology
WTC	World Trade Center
SCI	Steel Construction Institute, United Kingdom
SFRM	Sprayed Fire Resistive Material
SPM	Slab Panel Method
WWR	Welded Wire Reinforcement

Preface

This work was conducted as part of the *Measurement of Structural Performance in Fire* project under the NIST Engineering Laboratory's *Fire Risk Reduction in Building Program*. The authors thank William Baker (Skidmore, Owings, and Merrill), Craig Beyler (Jensen Hughes), Luke Bisby (University of Edinburgh), Ian Burgess (University of Sheffield), Charles Carter (AISC), Charles Clifton (University of Auckland), Michael Engelhardt (University of Texas), Graeme Flint (Arup), Nestor Iwankiw (Jensen Hughes), Kevin LaMalva (Holmes Fire), Roberto Leon (Virginia Tech.), Kristi Sattler (AISC), and Amit Varma (Purdue University) for their expert consultation. The authors also thank the current and former NIST colleagues including Laurean DeLauter, Marco Fernandez, Xu Dai, William Grosshandler, Jonathan Weigand, Joseph Main, Fahim Sadek, Chao Zhang, Ana Sauca, Mina Seif, and John Gross for their significant contributions to design, construction, and execution of this test program.

Dedication

This report is dedicated to the memory of Brian R Story (1977 - 2022). Brian was tirelessly devoted to the success of this project and will be dearly missed by his colleagues at NIST. Brian brought a rare combination of technical expertise and practical hands-on experience to his work and his presence is irreplaceable.

1. Introduction

A multi-year experimental research project was conducted at the NIST National Fire Research Laboratory to study the behavior of full-scale composite floor systems exposed to large enclosure fires. The test program was aimed to generate technical information and data essential for the development and validation of predictive tools that can be used for performance-based design and assessment for steel-framed buildings in structurally significant fires.

1.1. Background

Steel-concrete composite floors are widely used in modern steel buildings because of their cost effectiveness for spanning large open spaces. However, the fire safety design of composite floors in the United States, regardless of their size and geometry, is mainly based on prescriptive fire-resistance rating of small-scale assemblies tested following the century-old standard fire testing method. This testing method usually requires a test assembly that is representative of the structural details used in construction, however, the size and support conditions of a test assembly are limited by available furnaces in testing facilities.

Over the last few decades, significant research efforts have been made to better understand the integrity of full-scale composite floor systems under realistic fire loading. The Cardington test program [1, 2] in Europe, which was performed in an eight-story steel-framed building, demonstrated that the fire resilience of composite floor systems was superior to that observed in standard fire tests on isolated composite beams. Membrane action of the composite slabs was observed as secondary load-carrying mechanism after the support beams lost their flexural capacity at extremely high temperature. These findings led to the possibility of eliminating fire protection of the secondary (filler) beams and the development of simplified design methods [3–5] accounting for the load-displacement relationship of composite floor assemblies in tensile membrane action at elevated temperatures. Both the FRACOF [6] and COSSFIRE projects [7] further examined the benefit from membrane action by conducting standard fire tests on full-scale composite floor assemblies with the bare steel secondary beams. These tests indicated that the increased amount of steel reinforcement in composite slabs can significantly enhance their fire resistance beyond a specified rating period.

A significant variation exists in steel reinforcement requirements for composite slabs with steel decking in current construction practice. Table 1 shows a summary of the minimum steel reinforcement prescribed in building design standards as well as that used in previous large-scale fire experiments which demonstrated superior fire resilience of composite floors exposed to structurally significant fires. In the United States (US), the Steel Deck Institute standard (ANSI/SDI C-2017) [8] specifies a minimum required crack-control reinforcement ratio of 0.075 % for a composite floor slab with steel decking. The Underwriters Laboratories testing standard (UL 263) [9], essentially identical to the ASTM E119 standard [10], allows using a similar reinforcement area for standard furnace testing to determine a fire rating of small-scale composite floor or beam assemblies. The British standard, SCI-P56 [11], permitted a minimum slab reinforcement of 142 mm^2/m for the fire resistance design of composite floors with steel decking. The same amount of steel reinforcement was used in the Cardington test program. The post-Cardington large-scale experiments (e.g., FRACOF and COSSFIRE projects) used the reinforcement ratio designed using Bailey's method [3–5], ranging from 0.26 % to 0.33 %. The

steel reinforcement ratio of composite slabs permitted in the US practice is considerably lower than that used in prescriptive design of composite floors (incorporating tensile membrane action) used elsewhere. The floor integrity provision in the US fire testing standard tends to focus on the heat transfer aspect only (i.e., delaying the unexposed surface temperature by passive fire protection measures), not specifically accounting for the concrete damage associated with structural responses (i.e., excessive vertical displacements) of composite floors to fire. It is noteworthy that the fire resistance design in the US does not consider the slab reinforcement as a factor to determine fire resistance and is not always based on the displacement limit specified in the furnace testing standard.

Table 1. Steel reinforcement in concrete slabs specified in design standards and used in research.

Standard or Test Name	Reinforcement area	Reinforcement ratio*	Reinforcement details
ANSI/SDI C-2017 [8]		0.075 %	
SCI-P56 [11]	142 mm^2/m		6 mm mesh reinforcement at 200 mm spacing
Cardington Tests 3, 4, 7 [1, 2]	142 mm^2/m	0.20 %	6 mm mesh reinforcement at 200 mm spacing
FRACOF [6]	256 mm^2/m	0.26 %	7 mm mesh reinforcement at 150 mm spacing
COSSFIRE [7]	256 mm^2/m	0.33 %	7 mm mesh reinforcement at 150 mm spacing

*Computed as the ratio between the cross-sectional area of a steel wire to the cross-sectional area of the topping concrete above the fluted steel deck per unit slab width.

As alternatives to a prescriptive approach, the US building design standards (e.g., AISC 360 Appendix 4 [12], ASCE 7 Appendix E [13], and ASCE Manual of Practice 138 [14]) offer a variety of resources that allow engineers to adopt performance-based design of buildings in fire. However, numerical analyses used in performance-based design require validation against test data and experimental evidence of the extent of fire-induced structural damage during and after fire exposure. Previous studies mentioned above have provided useful insights into the capability of composite floors to activate membrane action in fire; however, the data and findings from those studies are more relevant to the European standard practice. There is a lack of experimental data quantifying the fire performance of full-scale composite steel frames designed in accordance with U.S. building codes and specifications.

The National Institute of Standards and Technology (NIST) conducted large-scale fire experiments using a two-story steel gravity frame designed and constructed following the U.S. practice. The fire experiments were designed to evaluate the system-level fire resistance, structural performance, and failure modes of the full-scale composite floor assemblies with the most realistic restraints from the surrounding structural assemblies. This test program included a total of three experiments. The fire test floor, 9.1 m × 6.1 m in plan, was situated on the first floor level in the middle edge bay of the two-story test building and was tested under combined mechanical loads and compartment fire exposure. In these experiments, the influence of a variety of factors, including the steel reinforcement used in the slabs and passive fire protection scheme of the steel framing, on the fire resilience of full-scale composite floor systems was investigated.

The first experiment (Test #1) was conducted on November 14th, 2019, to generate the baseline data for current US prescriptive approach applied to a full-scale building floor system and to compare with the second and third experiments. Literature review, experimental design, measurement systems, and results of Test #1 are reported in Choe et al. [15, 16]. An overview of Test #1 and key findings from this study are summarized in Sect. 1.2. The second experiment (Test #2) was conducted on March 10th, 2021 to study fire resilience of the composite floor system with the enhanced slab reinforcement detailed to allow tensile membrane action to develop [17]. Literature review, experimental design, measurement systems, and results of Test #2 are reported in Choe et al. [18] and Ramesh et al. [19]. An overview of Test #2 and key findings from this study are summarized in Sect. 1.3. The third experiment (Test #3), the focus of this report, was conducted on February 3rd, 2022 to study the effect of enhanced slab reinforcement as well as unprotected secondary beams on the fire resilience of the composite floor systems. In these tests, all other conditions remained similar, including the specimen geometry, beam-end connections, test fire curves, and imposed gravity loads.

1.2. Composite Floor Test #1

The first experiment, Test #1, investigated the structural performance and failures of the 9.1 m × 6.1 m composite floor system designed following the current US practice, incorporating prescriptive fireproofing insulation details to achieve the 2-hour fire-resistance rating and the minimum steel reinforcement (with a cross-sectional area per unit width, 60 mm^2/m) prescribed for shrinkage and temperature crack control of a concrete slab with fluted steel decking.

The full-scale two-story steel frame two bays by three bays in plan was used to mimic the realistic boundary conditions of composite floors when exposed to fire (Fig. 1). The fire test compartment (10 m × 6.9 m × 3.8 m) with the main opening (5.8 m × 1.5 m) on the exterior wall was situated in the south middle bay of the two-story test building. There was a 5.8 m × 0.3 m slit on the north wall designed for air intake only. Four natural gas burners (1 m × 1.5 m each in size and rated 16 MW total) distributed on the floor of the test compartment created standard fire exposure to the soffit of the composite floor in the test bay (Fig. 1). During fire exposure, the composite floor in the test bay was hydraulically loaded to 2.7 kPa which resulted in a total gravity load of 5.2 kPa according to the ASCE 7 [13] load combination for fire conditions (1.2 × dead load + 0.5 × live load). The composite floors in the adjacent bays, which remained cool during fire loading, were loaded to 1.2 kPa (equivalent to 0.5 times live load) using water-filled drums. Over 300 data channels were used to characterize the fire testing conditions as well as thermal and structural responses of the two-story building to the test fire at a variety of locations.

The natural gas fueled compartment fire produced the upper layer gas temperature (below the composite floor) closely following the temperature-time relationship used in standard fire testing. The peak gas temperature of 1060 °C was recorded when both the test fire and hydraulic loading was removed at 107 min. Temperatures of the protected steel beams in the test bay reached a peak value of 800 °C. The peak heat release rate and total heat energy was measured 10.8 MW and 63.5 GJ, respectively.

(a) (b)

Fig. 1. Test #1 (a) compartment fire test in the south middle bay of the two-story building under 20 MW exhaust hood; (b) top of the composite floor developing slab breach at 106 min after burner ignition.

During fire, the heated composite floor (with imposed mechanical loads on top) continuously sagged, reaching the peak vertical displacement of 60 cm at 107 min. The 9.1 m long floor beams (W16×31) buckled at their ends due to large compressive forces induced by the restraint to thermal elongation. The exterior columns (W12×106) bent outward due to thermal expansion of the heated floor assembly, resulting in partial shear ruptures in some bolts connected to those columns.

Whereas temperatures of the protected steel beams were acceptable compared to the ASTM E119 [10] limiting temperatures, significant integrity failure (concrete cracks) occurred in the heated composite floor before attaining the specified fire rating period. Large concrete cracks appeared around the hogging moment region (next to the test-bay column gridline) less than 30 min into heating, and the mid-panel concrete cracks began to occur at 70 min, exposing the hot glowing steel deck beneath along the longitudinal centerline (Fig. 2).

The limited ductility of the heated composite slab was the primary cause of the integrity failure which might eventually lead to local collapse mechanisms during longer (uncontrolled) fires and initiate fire spread above the compartment of fire origin. The steel wire reinforcement (60 mm^2/m) embedded in the test floor slab ruptured in tension at critical locations as the thermally degraded composite floor sagged but before reaching the ASTM E119 displacement limit. The minimum steel reinforcement (60 mm^2/m) prescribed for concrete crack control in normal conditions and permitted in standard furnace testing may not be sufficient to maintain the integrity of a full-scale composite floor undergoing the 2-hour standard fire exposure.

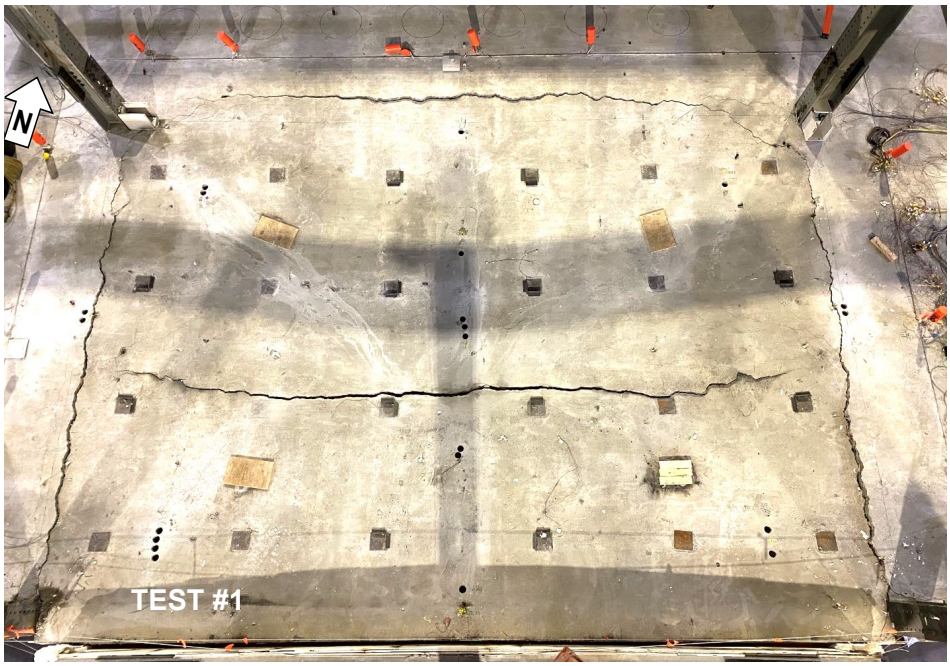

Fig. 2. Test #1 composite floor after cool down.

1.3. Composite Floor Test #2

The second experiment, Test #2, investigated the influence of enhanced slab reinforcement with larger cross-sectional area and ductility on the fire resilience of the full-scale composite floor subjected to combined mechanical and fire loading. In Test #2, the slab reinforcement scheme of the test floor assembly consisted of No. 3 (9.5 mm diameter) deformed bars (ASTM A-615 Grade 60) with the spacing of 30.5 cm in both orthogonal directions, resulting in the equivalent area of 230 mm^2/m slab width. All other conditions remained comparable to those used in the first experiment (Test #1) of this test program, including the specimen geometry, beam-end connections, test fire curves, imposed gravity loads, and passive fire protection of the exposed steel frame.

While sustaining a mechanical load of 125 kN which resulted in a total gravity load of (1.2 × dead load + 0.5 × live load), 290 kN, the test floor assembly was heated by the natural gas fueled compartment fire with the peak heat release rate approximately equal to 12 MW. The natural gas burners were switched off at 131 min due to a damage of the fire compartment which resulted in fire leak above the slab, whereas mechanical loading was continued over a 2-hr cooling period.

The average upper layer gas temperature within the test bay was approximately 10 % higher than that specified in ASTM E119 [10] standard and approximately 5 % higher than the temperature measured in Test #1. The peak average temperature was recorded at 1130 °C. The SFRM protected 9.1 long secondary beams (W16×31) were heated to 850 °C on average at the bottom flanges until the test fire was extinguished. The average top surface temperature of the heated floor slab reached nearly 150 °C during heating and further increased to 190 °C during the cooling phase of the test fire.

The mid-panel vertical displacement reached 455 mm at 131 min in fire. The peak displacement of 475 mm was measured about 15 min after the test fire was extinguished. The vertical and

horizontal displacements of the test assembly increased more slowly with increasing temperature compared to those observed in Test #1. This result might be attributed to the maintenance of slab continuity (through No. 3 bars) in the hogging moment region during the heating phase. Most of concrete cracks including those in the hogging moment region were less than 5 mm wide after cooldown (Fig. 3). From the post-test inspections, only one longitudinal bar next to the southwest column was found to be ruptured.

In Test #2, all fire-exposed beams exhibited some degree of permanent global deflection and local buckling; however, all shear-tab connections appeared to be intact and robust after cooling. No steel ruptures in connection elements (plates, bolts and welds) were identified. However, the bottom bolts connected at the south ends of the girders exhibited some degree of bending. All four extended shear tabs connecting the girders significantly bent due to thermal expansion of the floor specimen.

After cooldown, the test floor assembly was loaded again using the same hydraulic actuators used in the fire testing to examine its post-fire flexural behavior at ambient temperature. The floor specimen reinforced with No. 3 bars retained a large flexural strength after cooled down from fire exposure. No additional structural damage was reported until the floor specimen was loaded to 90 % of the calculated nominal capacity at ambient temperature. This second test suggests that the fire resilience of the composite floor can be significantly improved by using a higher reinforcement ratio achieved with No. 3 reinforcing bars (with a reinforcement area of 230 mm^2/m width of the slab). It showed that the use of enhanced slab reinforcement maintained the structural integrity of the tested slab for longer fire exposure.

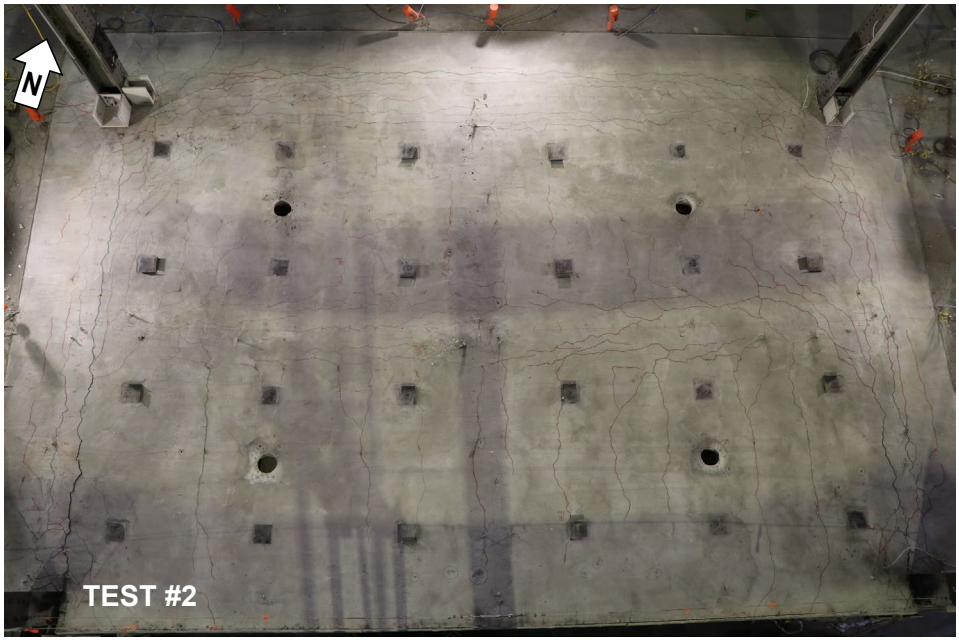

Fig. 3. Test #2 composite floor after cool down.

1.4. Scope and Objectives

This report presents the third experiment (Test #3) conducted on February 3, 2022. This study was aimed to investigate the influence of the slab reinforcement and the secondary beam's fire protection on the structural performance of the full-scale composite test floor assembly subjected to combined mechanical and fire loading. The effect of the test variables on the fire resilience and failure characteristics of the composite floor system is discussed in this report.

The experimental measurements include:

- fire characteristics including heat release rates, gas temperatures, velocity flow of the openings, and heat fluxes from the natural gas fueled compartment fire,
- thermal (temperatures) and structural responses (displacements, forces, and strains) of the test building, and
- any noteworthy observations during the fire test and post-test inspections critical to understand the overall fire performance and failure modes of the test floor assembly.

This report offers the unique experimental results that provide insight into the effects of standard fire exposure in a real building structure and potential failure mechanisms of full-scale steel-concrete composite floor systems including steel frame connections and slab continuity. This technical information can be used to guide the development and validation of physics-based computational models of composite floor assemblies in fully developed fires as well as after the fire is extinguished. This research effort also provides important steps toward the improvement of the current fire testing methods and performance-based design provisions for steel-framed buildings in fire.

2. Experimental Design & Construction

2.1. Fire Test Setup

Details of the two-story steel-framed building and the fire test setup are presented in Choe et al. [15] and summarized herein. The fire test was conducted on the two-story steel gravity frame two by three bays in plan constructed below the 15 m × 14 m exhaust hood at the NFRL, as shown in Fig. 4. The test frame has the footprint of 1036 cm × 1768 cm (34 ft. × 58 ft.) with an average 366 cm (12 ft.) story height. Composite floors were constructed on the first-floor level, whereas the second-floor steel framing provided braces to the steel columns of W12×106 shapes. Each W12×106 column had a 91 cm × 91 cm × 5 cm steel plate (ASTM A572 Grade 50 with a minimum specified yield strength of 50 ksi) welded to the base of the column and these base plates were anchored to the strong floor using four 3.5 cm diameter high strength steel bars (Grade 150 with a minimum specified tensile strength of 150 ksi) post-tensioned to 445 kN (100 kip) each. Refer to Appendix A13 for details of boundary conditions at the column base.

The fire test bay (687 cm × 1008 cm × 377 cm) was situated in the south middle bay of the test building on the ground floor, with the footprint slightly greater than the column grid size (610 cm × 914 cm). Enclosing walls (along the red lines in Fig. 4b) were constructed as non-load bearing walls made of sheet steel with Type-C gypsum board lining at the exposed surface. Columns were not directly exposed to fire except for the upper region where the floor beams or girders of the test bay were joined. Four natural gas burners (1 m × 1.5 m each and rated 16 MW total) on the ground floor were used to create realistic fire exposure to the soffit of the composite floor in the test bay. Purpose-built slab splices (along the blue lines in Fig. 4b) were designed to reuse the same surrounding floors throughout the test program, and therefore only the fire-exposed floor assembly was reconstructed new for each test.

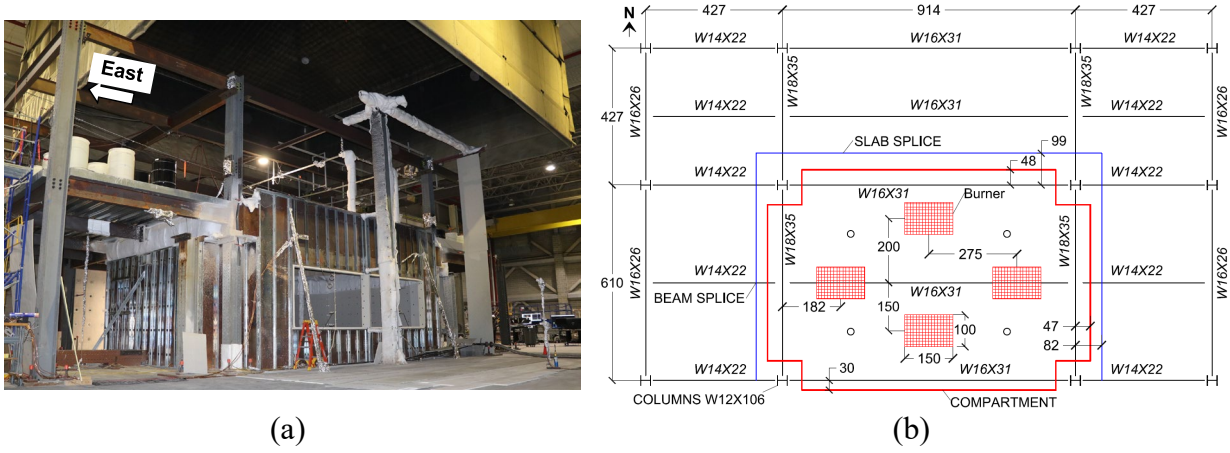

Fig. 4. (a) Photograph of the two-story test frame and (b) scale drawing of floor plan. Units are in cm.

The main ventilation opening was on the south exterior wall, approximately 150 cm tall × 582 cm wide as shown in Fig. 5a. There was a 30 cm tall × 582 cm wide slit on the north wall for air intake only. The height of the windowsill (i.e. the bottom of the opening) on both north and south sides was 100 cm from the strong floor. The design basis of a test fire condition is presented in Zhang et al. [20].

Figure 5b shows the mechanical loading arrangement. The test-bay floor was loaded using four hydraulic actuators providing a total imposed load of 2.7 kPa (load applied by the actuators + self-weight of the loading system) distributed to 24 loading points over the test floor as shown in Fig. 5b. The total gravity load (including the floor self-weight of 2.5 kPa) was 5.2 kPa, which conforms to the gravity load demand determined from the ASCE 7 [13] load combination for extraordinary events (1.2 times dead load plus 0.5 times live load). The surrounding floors were loaded by water-filled drums, providing an imposed gravity load of 1.2 kPa, equivalent to 50 % of an office live load as specified in the ASCE 7 standard.

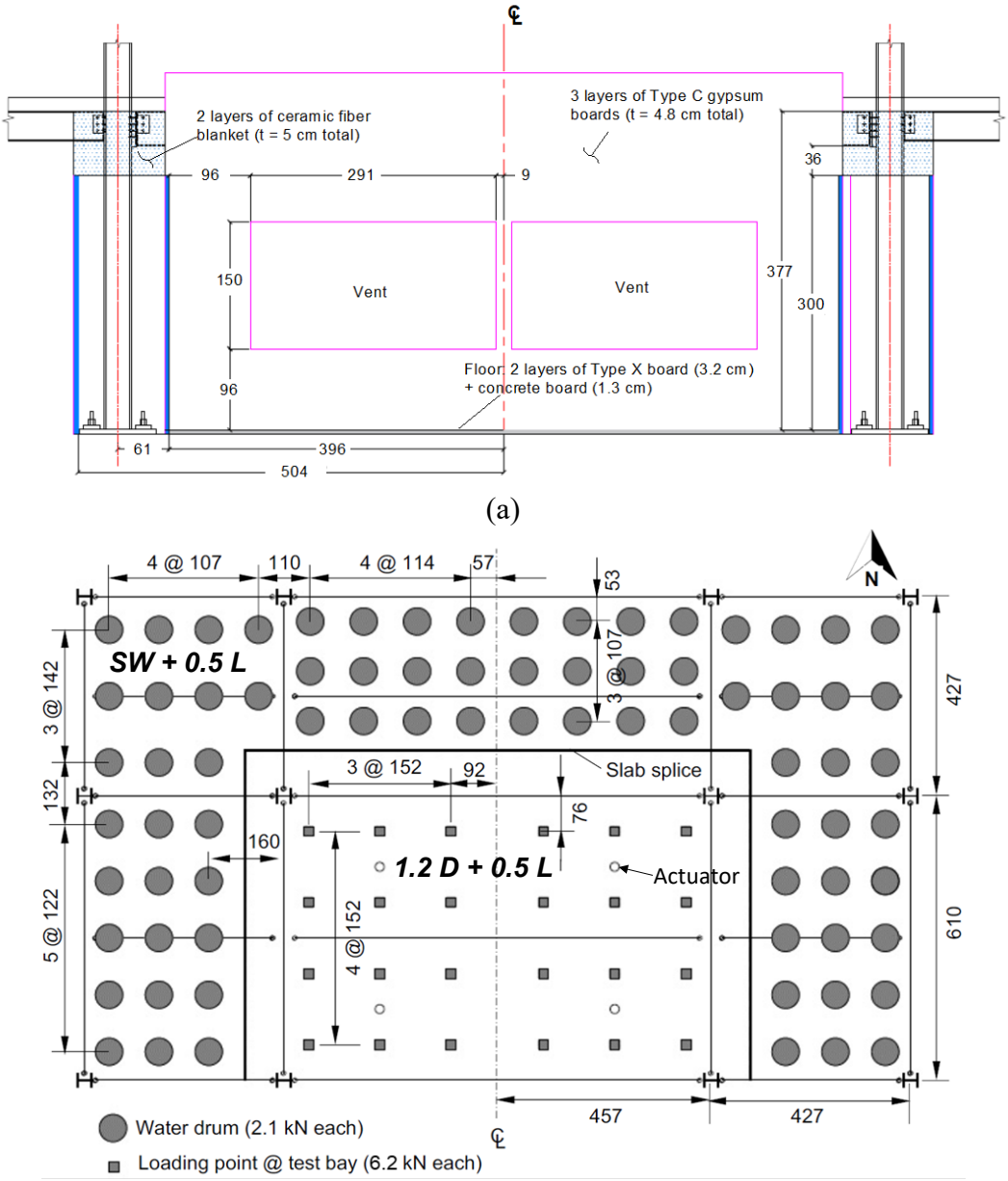

Fig. 5. Scale drawings of (a) south wall with main ventilation opening; (b) mechanical loading arrangement. Units are in cm.

2.2. Design Basis of Composite Floor Test #3

The primary difference between Test #1 and Test #2 was the steel reinforcement scheme used in the composite slab in the test bay. Test #1 demonstrated that the welded wire reinforcement (WWR) of 6×6 W1.4×W1.4 mesh mat (with a cross-sectional area of 60 mm^2/m slab width), shown in Fig. 6a, was not sufficient to maintain slab integrity up to the specified rating period (2 h), with a potential risk of fire spread beyond the compartment of fire origin. Hence, for Test #2, it was decided to study the influence of the steel reinforcement on the fire resilience of the composite floor while other conditions remained mostly unchanged. With several iterations performed for the selection of slab reinforcement using the Slab Panel Method (SPM) [21] which has been used in the New Zealand (NZ) practice, a slab reinforcement with No. 3 deformed reinforcing bars with the spacing of 30.5 cm in both orthogonal directions (9.5 mm diameter hot rolled deformed bars which provided a reinforcement area of 230 mm^2/m slab width and a reinforcement ratio of 0.28 %) was used in Test #2. Within the test bay in Test #2, the No. 3 reinforcing bars were spliced as the length of the bars which were available to be acquired was limited to 6.1 m (20 ft). Mechanical couplers were used to splice the bars to rule out the effect of splice failure on the structural behavior of the composite floor. The same slab reinforcement used in Test #2 (No. 3 deformed reinforcing bars with the spacing of 30.5 cm in both orthogonal directions) was used in Test #3 as well. However, ACI-318 [22] specified contact splices were used in Test #3, instead of the mechanical couplers, to replicate the construction practice. The No. 3 bars were spliced by overlapping the bars for a length of 63.5 cm (25 in.).

Similar to Test #1 specimen, all the fire exposed steel members in Test #2, including the secondary beam and its end connections, were sprayed with fire resistive material required for a 2-hr restrained assembly fire rating (Fig. 7a). In the Test #3 specimen, the secondary beam and its end connections were left unprotected, as shown in Fig. 7b, to evaluate the effect of fire protection of the secondary beam on the fire resistance of the composite floor when combined with the enhanced slab reinforcement provided by the No. 3 deformed reinforcing bars.

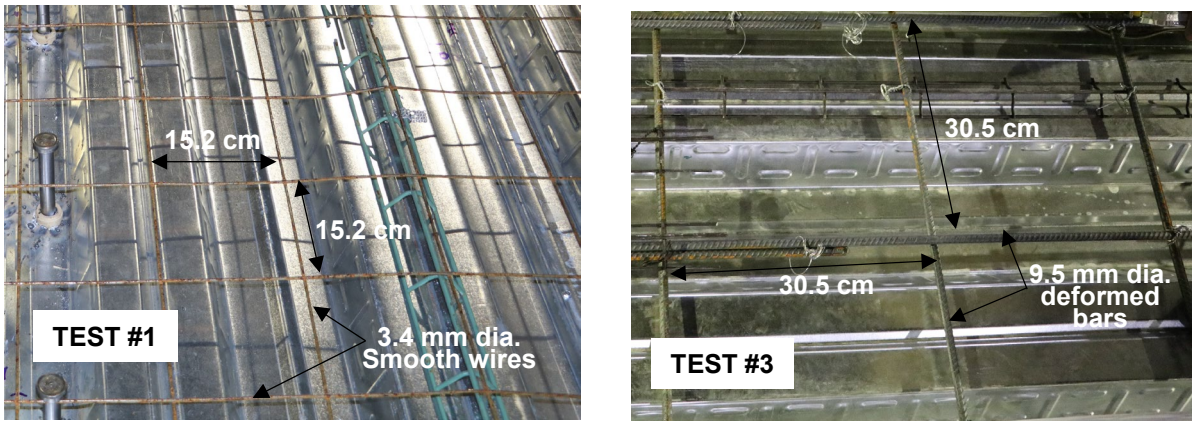

(a) (b)

Fig. 6. Slab reinforcement (a) Test #1; (b) Test #3.

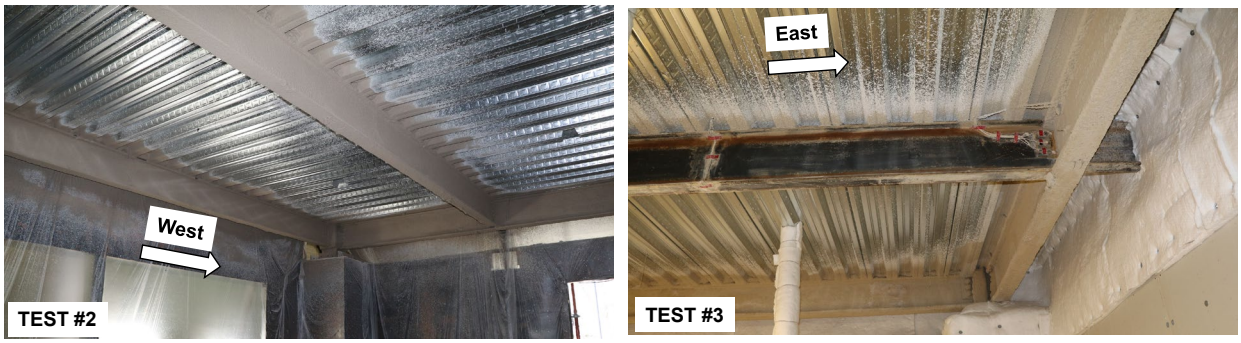

(a) (b)

Fig. 7. Fire protection scheme (a) Test #2; (b) Test #3.

2.3. Composite Floor Design and Construction

The steel frames within the fire test bay consisted of three 914 cm (30 ft.) long W16×31 shapes and two 610 cm (20 ft.) long W18×35 shapes as shown in Fig. 4b. Refer to AISC Steel Construction Manual [23] for the dimensions of the steel shapes. The ends of the W16×31 beams were connected via standard shear tabs (8½×6×3/8 in.) with three 1.9 cm (0.75 in.) diameter structural bolts whereas the W18×35 girders were connected to the webs of W12×106 columns using extended shear tabs (9-7/8×14½ ×3/8 in.) with five 1.9 cm diameter structural bolts. The weld size used in the shear tab connections was 6.3 mm (0.25 in.). Short-slotted holes, 2.1 cm (13/16 in.) wide and 2.5 cm (1 in.) long, were drilled on the connecting elements, whereas the standard holes with the diameter of 2.1 cm were drilled on the webs of beams and girders. Details of the beam-end connections are shown in Fig. 8.

The composite floor was constructed with lightweight aggregate concrete and 7.6 cm (3 in.) deep profiled steel decking as shown in Fig. 9. The deck flute was oriented perpendicular to the 914 cm long beams. The topping concrete (above top ribs) was 8.3 cm (3.25 in.) thick as required to achieve the 2-hr fire resistance rating. Steel headed stud anchors with 19 mm shaft diameter were welded to the top flange of the W16×31 shapes with one stud at every 30 cm (12 in.). They were welded to the top flange of the W18×35 shapes with two studs at every 36 cm (14 in.). The corresponding composite action was estimated to be about 65 % of the yield strength of steel shapes at ambient temperature. Photographs of the floor specimen soffit, beam framing, and connections are shown in Fig. 10.

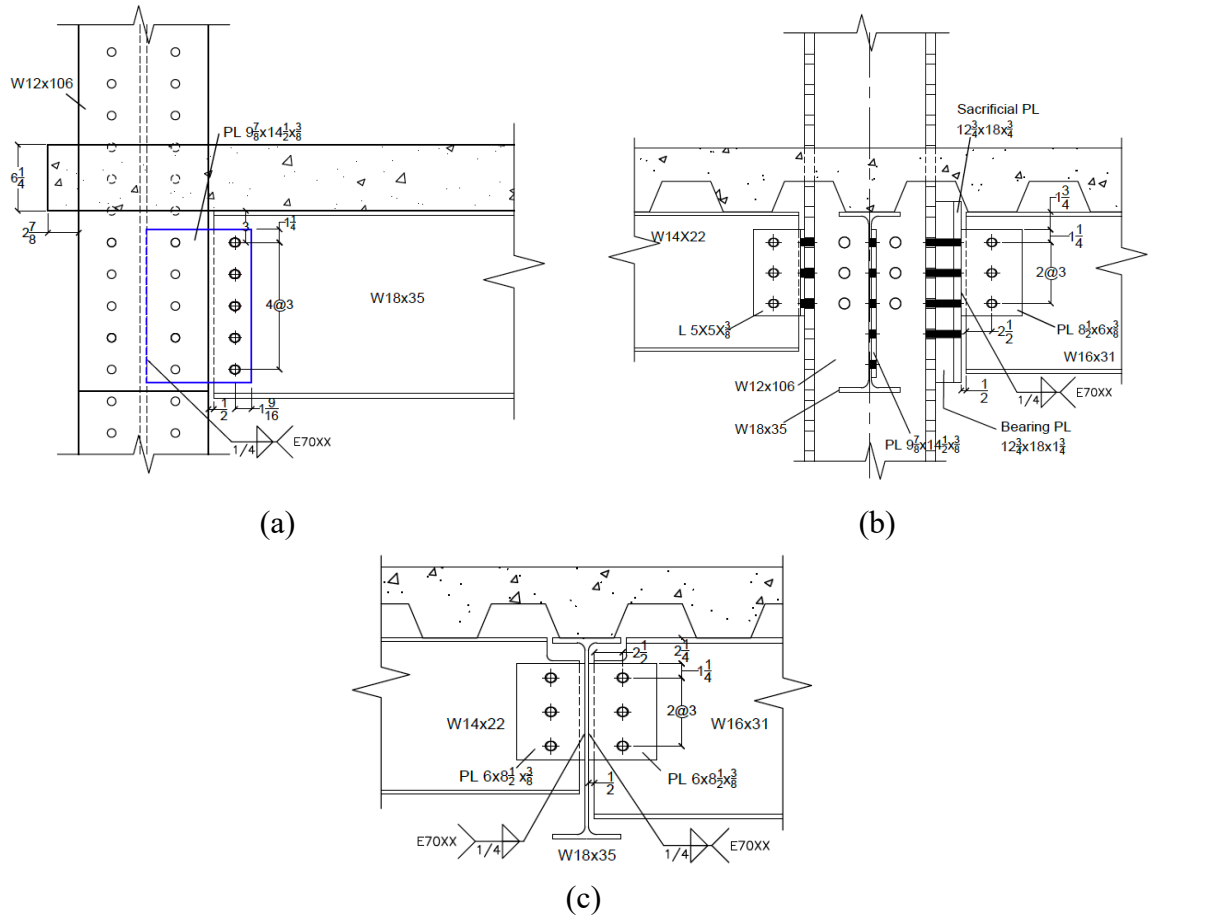

Fig. 8. Scale drawings of connection details in the test bay (a) girder to column connection; (b) beam to column and girder to column connections; (c) secondary beams to girder connections. Units are in inches.

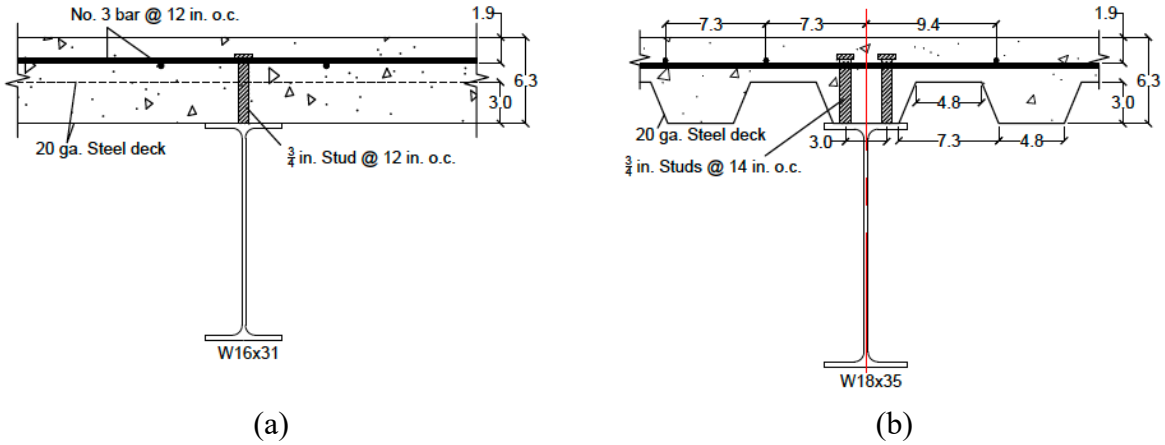

Fig. 9. Scale drawings of (a) composite floor beams and (b) girders in the test bay. Dimensions are in inches and rounded to the nearest tenth.

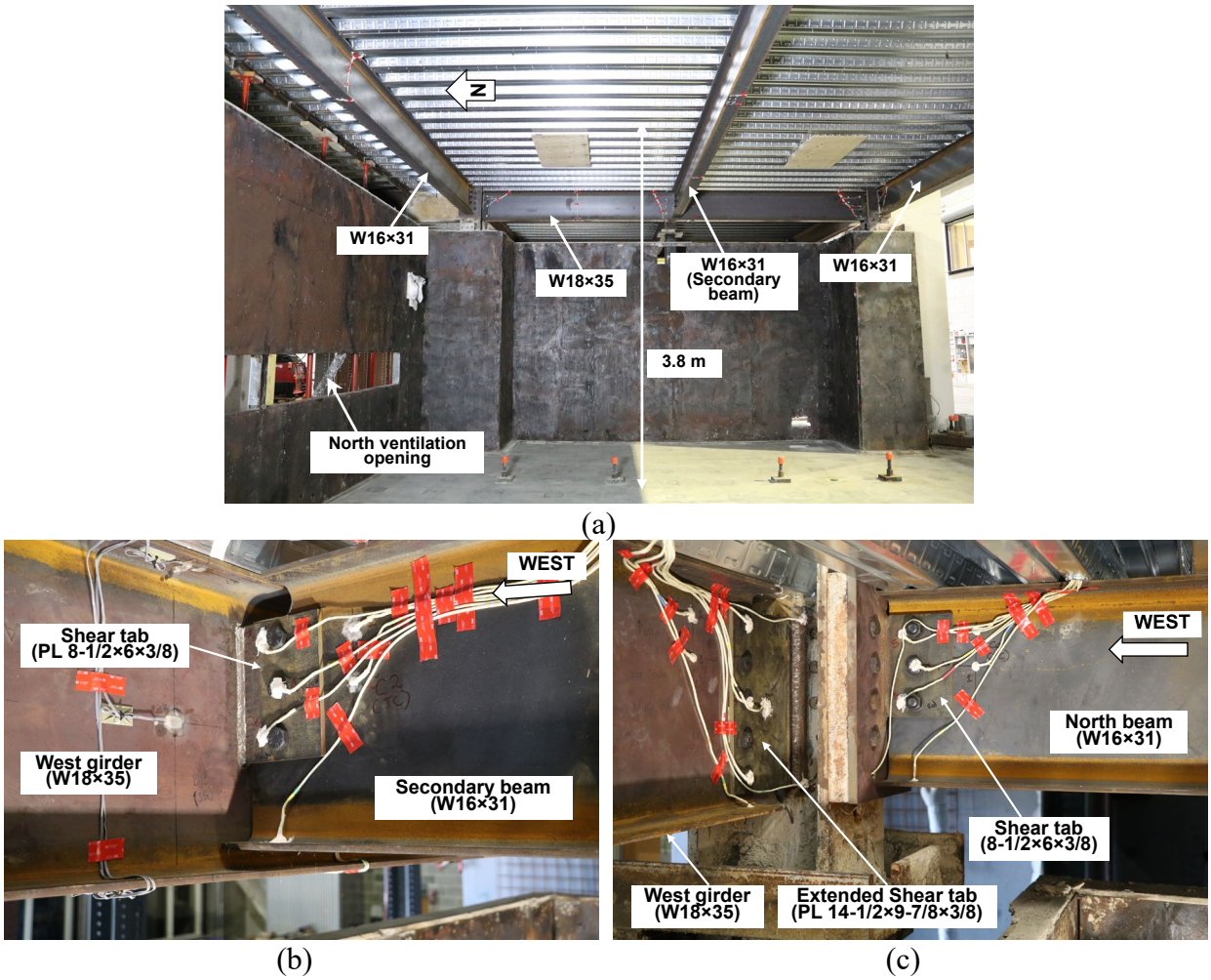

Fig. 10. Photographs of Test #3 floor specimen: (a) steel work; (b) beam-to-girder connections; (c) beam-to-column connections prior to fireproofing insulation.

The floor slab was reinforced with two layers of No. 3 deformed bars at 30.5 cm (12 in.) spacing as shown in Fig. 11. The spacing of some transverse bars adjacent to the east and west column lines of the test bay ranged from approximately 19 cm (7.5 in.) to 42 cm (16.5 in.) due to the bar clear distance from support columns. The longitudinal bars had a clear cover of 4.8 cm (1.9 in.) from the top surface of the concrete, and the transverse bars had a clear cover of 3.8 cm (1.5 in.) from the top surface of the slab. The south ends of transverse bars had the 180-degree standard hooks to minimize separation of the concrete slab from the south edge beam during the fire test. The reinforcing bars were spliced by overlapping the bars for a length of 63.5 cm (ACI-318 [22] specified contact splice) within the test bay. In the north-south direction, the distance to the center of the 63.5 cm long contact splice in the transverse bars was 99 cm (39 in.) from the centerline of the north edge beam. In the east-west direction, the distances to the center of splices in the longitudinal bars were 184.5 cm (72.5 in.) from the centerlines of the east and west girders. These bars were also lapped with the 63.5 cm (25 in.) long No. 4 deformed bars extended from the slab splice line. Photographs of the test floor prior to concrete placement is provided in Fig. 12. Refer to Choe et al. [15] for the details of slab reinforcement in the surrounding floors.

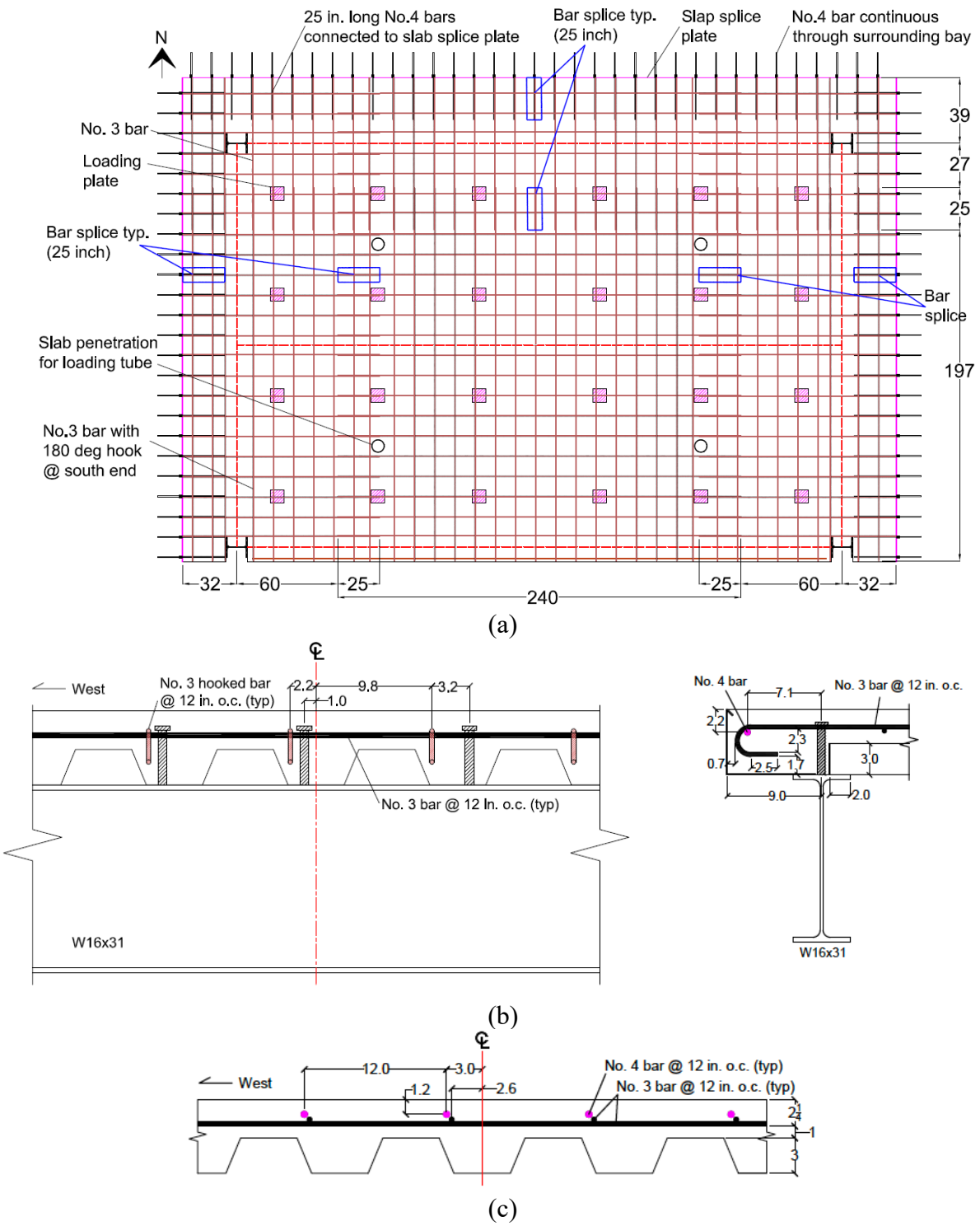

Fig. 11. (a) Scale drawing of slab reinforcement; (b) front and side views at south end; (c) front view at north side. Dimensions are in inches.

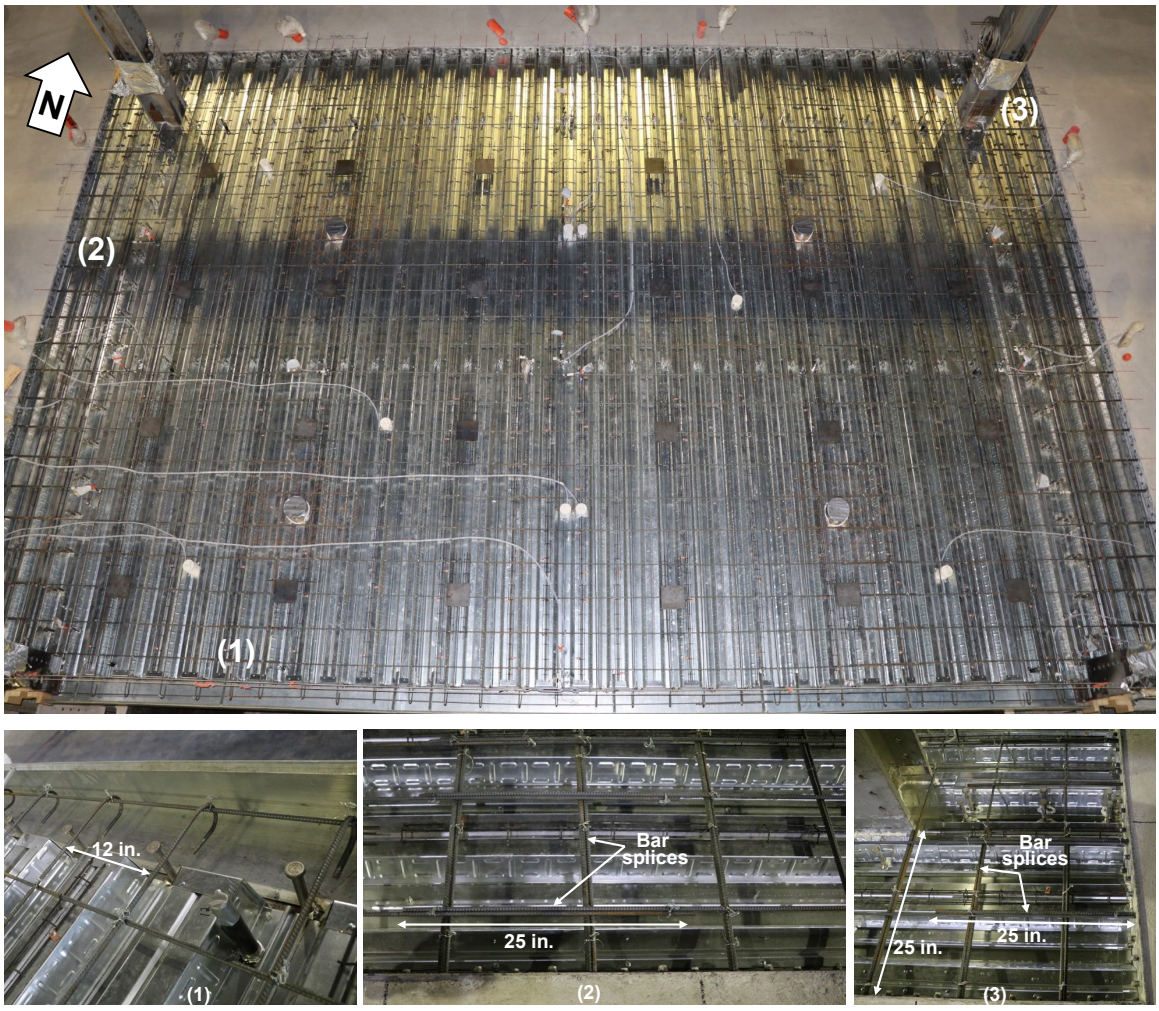

Fig. 12. Top of test floor assembly prior to concrete placement.

2.3.1. Mechanical Properties of Steel Components

The room-temperature mechanical properties of steel components constituting the test floor assembly were measured at a commercial testing facility. The fabrication of specimens (coupons) and testing procedures conformed to the ASTM E8/E8M [24] standard. Table 2 summarizes the average values of the 0.2 % offset yield strength (S_y), the ultimate tensile strength (S_u), and percent elongation at fracture (δ_u). The values after ± symbols indicate one standard deviation estimated using a uniform distribution of the two measured values. Refer to Appendix A12 for the stress-strain curves of the steel components.

Table 2. Measured mechanical properties of steel components.

Steel components	ASTM Designation	S_y (MPa)	S_u (MPa)	δ_u (%)
W16×31	A992	350 ± 10	480 ± 4	34 ± 1
W18×35	A992	370 ± 2	510 ± 2	33 ± 1
Shear tab plate	A36	290 ± 1	440 ± 30	37 ± 1
Headed stud anchor	A29	410 ± 2	510 ± 3	-
Structural bolt	A325 (F3125)	890 ± 10	970 ± 8	19 ± 1
Steel deck	A653	400 ± 4	470 ± 2	26 ± 1
No. 3 deformed bar	A615	480 ± 6	770 ± 8	21 ± 1

2.3.2. Fireproofing Insulation

The primary beams and girders as well as their end connections were protected with a commercially available sprayed fire resistive material (SFRM), which was a cementitious gypsum-based material with a density ranging from 240 kg/m^3 to 350 kg/m^3. The secondary beam and its end connections were left unprotected. The thickness of the SFRM applied to the protected steel substrate met the 2-hr fire-resistance rating requirement for Type IB construction in accordance with the IBC [25]. Table 3 shows the design and measured average values of the SFRM thickness. The values after ± are the coefficient of variation in the measurements.

Table 3. Design and measured thickness of SFRM.

Steel Component	UL Design No.	Design Thickness	Average Measured Thickness*
W16×31 (north primary beam)	N791	18 mm (11/16 in.)	19 mm ± 7 %
W16×31 (south primary beam)	N791	18 mm (11/16 in.)	19 mm ± 8 %
W16×31 (secondary beam)	D949	11 mm (7/16 in.)	-
W18×35 (east girder)	N791	18 mm (11/16 in.)	19 mm ± 7 %
W18×35 (west girder)	N791	18 mm (11/16 in.)	19 mm ± 6 %
Standard shear tab (beam-end connections)	-	25 mm (1 in.)	27 mm ± 6 %
Extended shear tab (girder-end connections)	-	25 mm (1 in.)	27 mm ± 6 %

*The values after ± symbol are the coefficient of variation. The SFRM thickness measurement was performed at 81 discrete points on each beam and 9 discrete points on each end connection region.

2.4. Concrete Placement and Curing

2.4.1. Mixture Design

The concrete mixture was designed to provide a lightweight aggregate concrete with hardened mechanical properties typical of those used in current construction practice, but with a low propensity for fire-induced spalling. To reduce the likelihood of spalling, 2.37 kg/m^3 (4 lb/yd^3) of monofilament polypropylene microfibers were used in the mix as proposed in Maluk et al. [26]. To further reduce the chance of fire-induced spalling, expanded slate lightweight aggregate with low water-retention characteristics and high desorption was selected as suggested in Pour-Ghaz et al. [27], to expedite the reduction of moisture in the concrete during curing. The concrete design mixture proportion are provided in Table 4.

Table 4. Concrete design mixture proportions.

		water/cement: 0.41	Slump: 14.0±2.5 cm (5.5±1.0 in.)
	Material	Surface Saturated Dry, kg (lb)	Volume, m^3 (ft^3)
Cement:	ASTM C-150: Type I/II Lehigh	254 (560)	0.081 (2.85)
Fly Ash:	ASTM C-618: Separation Technologies Class F	64 (140)	0.025 (0.89)
Aggregate:	ASTM C-33: Carolina Stalite LTWT	404 (890)	0.269 (9.51)
Sand:	ASTM C-33: Chaney Sand	622 (1372)	0.240 (8.46)
Air:	2.5%	-	0.019 (0.67)
Water:	ASTM C-1602; ASTM C-1603	129 (284)	0.129 (4.55)
Admixture:	See details below	5 (10)	0.002 (0.07)
	Total	1477 (3256)	0.765 (27.00)
	Unit Weight kg/m^3 (pcf)	1932 (120.6)	
	Calculated Equilibrium Dry Density kg/m^3 (pcf)	1853 (115.7)	

Admixtures

FRC MONO-150 - 2.37 kg/m^3 (4 lb/yd^3)

Sika Visocrete 2100 - 1.75 ± 1.75 ml/kg (3 ± 3 oz/cwt)

Sika Plastocrete 161 - 2.91 ± 1.16 ml/kg (5 ± 2 oz/cwt)

SikaTard 440 - 1.16 ± 1.16 ml/kg (2 ± 2 oz/cwt)

Sika ViscoFlow 2020 - 2.33 ± 1.16 ml/kg (4 ± 2 oz/cwt)

2.4.2. Concrete Placement

The concrete was batched at a local ready-mix concrete plant and trucked to NIST for casting (on 9/14/2021). A total of two trucks were used to cast the test floor slab. Although the design mixture proportions were the same for both batches (trucks), small adjustments were made by adding superplasticizer and trim water prior to the concrete placement. Immediately after casting, the concrete was covered with wet burlap to maintain a wet surface condition. The burlap was re-wet, as necessary, for the first 7 days of curing, after which the burlap was removed. The

concrete in the surrounding bays had been cast on 6/4/2019, when the Test #1 test floor was cast, and remained in place.

2.4.3. Curing Conditions

The relative humidity and temperature in the concrete during curing were measured using probes placed into perforated sleeves embedded in the concrete during casting. The manufacturer specified accuracy of the temperature and relative humidity in the applied temperature range are ± 0.2 °C and less than ± 2.5 %, respectively. The temperatures measured in the concrete are shown in Fig. 13 and the relative humidity measurements in Fig. 14. Measurement locations in the test specimen were in the southwest and northeast quadrants of the specimen to provide an indication of variation across the specimen. The measurement location for the surrounding bays was in the middle of the center north bay. No measurements were made in the surrounding bays until the time of testing. Therefore, the relative humidity in the concrete in the surrounding bays is significantly lower than in the test specimen. The moisture content of the specimens, which is related to the relative humidity, was measured separately on concrete cylinders cured under the same conditions as the slabs.

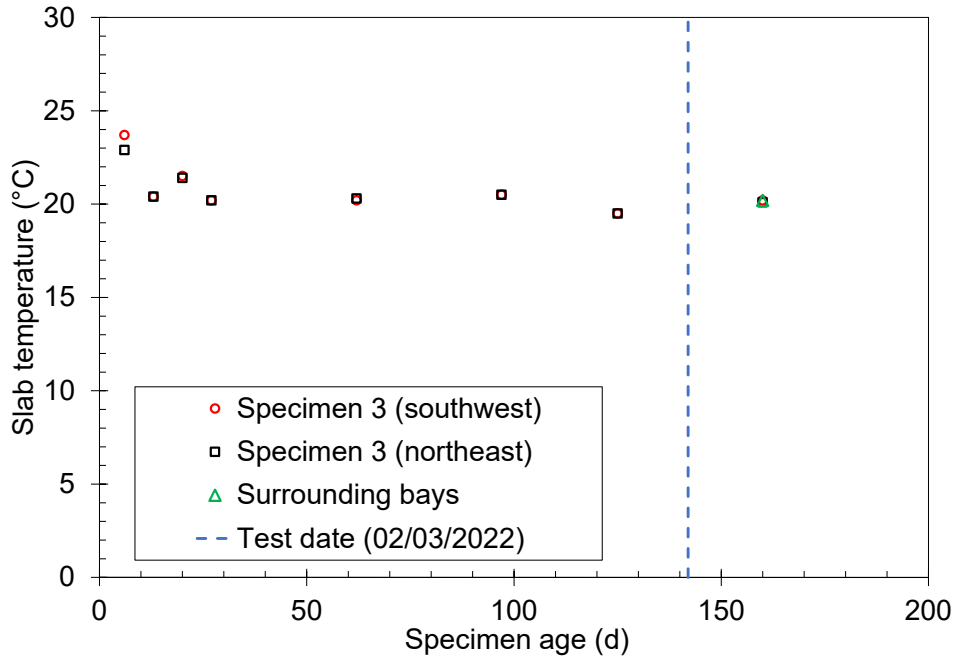

Fig. 13. Temperature in the test specimen and surrounding bays.

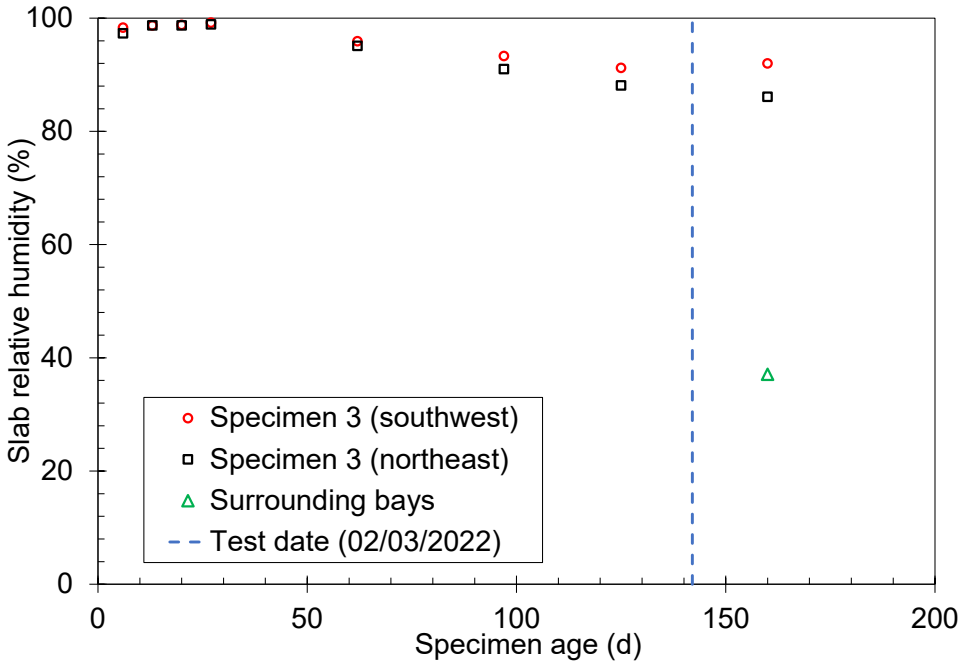

Fig. 14. Relative humidity in the test specimen and surrounding bays.

2.4.4. Hardened Concrete Properties

Table 5 summarizes the measured concrete properties. Where applicable, the relevant ASTM test standard used is provided in the table. The reader is directed to the current edition of these standards for details on those test methods. Details about the tests used to determine properties of the surrounding bay concrete are provided in Choe et al. [15]. The hardened concrete properties of the test floor concrete were measured within one week after the fire test of the composite floor. Those measurements were made from 102 mm × 204 mm concrete cylinders prepared according to ASTM C192 [28] and cured alongside the concrete slab in the test hall. They were measured at ambient laboratory temperatures; nominally 23 °C. No measurements of the concrete properties at elevated temperatures were made.

The slump and plastic unit weight of the concrete are reported in Table 6. No replicate measurements of the fresh concrete were made so standard deviation is not reported. Table 7 summarizes the measured properties (mean and one standard deviation) of the hardened concrete for each individual delivery truck (batch). Each value is from two or more replicates. Average values for the concrete in the test specimen and surrounding bays are provided in Table 8.

Table 5. Matrix of measured concrete properties.

Property	Number of cylinders			
	Casting 9/14/2021	28-day 10/12/2021	Day of Test	Total
Slump (ASTM C143)	✔	-	-	-
Plastic unit weight (ASTM C138) [b]	✔	-	-	-
Compressive strength (ASTM C39)	-	6	6	12
Density (ASTM C642)	-	-	[a]	-
Moisture content (ASTM C642)	-	-	6	6
[a] Use moisture content cylinders.			Total	18

Table 6. Fresh concrete properties.

Property	Truck number	
	T1	T2
Water-to-binder (cement + fly ash), -	0.41	0.41
Slump, cm	19.1	17.1
Tare ==> Empty measure, kg	6.42	6.42
Mass ==> Measure + Concrete, kg	34.32	34.82
Unit weight kg/m^3	1971	2006

Table 7. Hardened concrete properties for each truck.

Category	Description	Truck T1	Truck T2
Structural	Compressive strength, MPa	65.6 ±0.5	70.2 ±0.5
Thermal	Bulk density, kg/m^3	1928 ±5.8	1942 ±0.8
	Moisture content, % mass	8.4 ±0.1	7.6 ±0.1

Table 8. Average hardened concrete properties.

Category	Description	Specimen 3 (T1+T2)	Surrounding bays*
Structural	Compressive strength, MPa	67.9 ±2.3	63.0 ±1.1
	Splitting tensile strength, MPa	not available	5.7 ±0.4
	Static modulus, GPa	not available	24.9 ±0.2
Thermal	Bulk density, kg/m^3	1935 ±8	1911 ±10
	Moisture content, % mass	8.0 ±0.4	7.7 ±0.2
	Thermal conductivity, W/m·K	not available	2.18 ±0.14
	Specific heat, J/kg·K	not available	887 ±47

* The splitting tensile strength of the surrounding bay concrete was determined in June 2021; the remaining concrete properties of the surrounding bay were determined in November 2019.

2.5. Instrumentation & Measurement Uncertainty

Measurements were performed to quantify the applied mechanical and fire loading as well as the thermal and structural responses of the test structure during and after fire exposure. Details of the measurement system, data acquisition and recording systems are presented in Choe et al. [15] and briefly summarized herein. Appendix A provides the physical locations and channel names of the sensors.

The mechanical load applied on the floor specimen was controlled and measured using four servo-hydraulic actuators (Model: MTS 201.35TS). The heat release rate of the test fire was quantified using both the fuel consumption and oxygen consumption calorimetry [29]. The gas temperature produced in the fire test bay and temperatures of the floor specimen at various locations (including composite slabs, floor beams, and connections) were measured using K-type thermocouples (with 20-gauge or 22-gauge wires). Gardon gauges were used to measure instantaneous heat fluxes on the exposed surface of the compartment enclosure. Gas velocity through the ventilation opening of the test compartment was measured using bi-directional probes with high-precision capacitance manometers. Resistive displacement transducers were installed outside of the test compartment at a variety of locations to measure the vertical and horizontal displacement of the test structure. Linear strain gauges were mounted on the steel reinforcement in the test floor slab and at the base of the support columns and steel frames in the surrounding bays to measure the thermally induced forces during and after fire exposure.

The strain, voltage, and temperature measurements were digitized and recorded using National Instruments (NI) CompactDAQ and PXI systems with signal conditioned I/O Modules. The heat release rate measured by the NFRL's calorimeters were digitized and recorded using a separate data acquisition system described by Bryant and Bundy [29]. An in-house software developed in LabVIEW™ called MIDAS (Modular In-situ Data Acquisition System) was used to allocate channels and control the data acquisition.

High-definition cameras were deployed to record and live-stream a variety of video scenes of the test building and the fire test compartment during the heating and cooling phases of the fire. Thermal imaging of the unexposed (top) surface of the test assembly was performed using a high-speed infrared camera (Model: FLIR SC8303).

The measurement uncertainty is summarized in Table 9. The estimated total expanded uncertainty values are rounded to the nearest integer, except for the construction dimensions and heat release rate of burners which are rounded to the nearest tenth. The users of this report are advised that the experimental results presented in Chapter 3 are either raw data or the statistics of raw data. The authors recommend incorporating the measurement uncertainty reported herein into validation of predictive models or verification of new metrology techniques.

The standard uncertainty in measurements is estimated based on four categories in accordance with Taylor and Kuyatt [30] as follows:

- Type A uncertainty estimated using statistical analysis of the measured data, e.g., in-house calibration or random error caused by the test environment
- Type B uncertainty estimated by other means, such as manufacturer's data sheets (e.g., sensor resolution or factory calibration) or operator's experience (e.g., assumed misalignment or temperature effects)

- Combined standard uncertainty estimated using 'root-sum-of-squares' method to combine all the Type A and Type B uncertainty components
- Total expanded uncertainty computed by multiplying the combined standard uncertainty by a coverage factor (k) of 2 for a 95 % confidence level

The components considered in the component standard uncertainty include resolution, calibration, installation, and random errors. The resolution is the minimum change in the data measurement the instrument can exhibit. Calibration error includes uncertainties from calibration of the sensor. The resolution and calibration uncertainties were derived from instrument specifications (Type B). Uncertainty due to installation method was estimated based on engineering judgement (Type B) considering misalignment, quality of the mounting method of the sensors, and previous data. Random error which resulted from random unpredictable variations in the environment and measurement process was estimated as Type A using statistical analysis of the measured data. It was estimated as Type-B, using engineering judgement, in the absence of data for statistical analysis (for example, in the calculation of random error for the constructions dimensions).

Table 9. Estimated relative measurement uncertainty. FSO_E = maximum measured values; N = number of samples used for estimating random errors

Measurement / Component	Uncertainty Type	Standard Uncertainty	Combined Standard Uncertainty	Total Expanded Uncertainty (k=2)
Actuator Load (FSO_E = 125 kN)				
Resolution	Type B	± 0.1 %	± 0.6 %	± 1 %
Calibration	Type B	± 0.5 %		
Random (N=8400)	Type A	± 0.4 %		
Vertical Displacement (FSO_E = 655 mm)				
Resolution	Type B	± 0.1 %	± 1.2 %	± 2 %
Calibration	Type B	± 0.2 %		
Random (N=12000)	Type A	± 1.2 %		
Horizontal Displacement (FSO_E = 28 mm)				
Resolution	Type B	± 0.1 %	± 2.9 %	± 6 %
Calibration	Type B	± 1.1 %		
Temperature compensation	Type B	± 2.0 %		
Random (N=12000)	Type A	± 1.8 %		
Strain (FSO_E = 1875 με)				
Resolution	Type B	± 0.1 %	± 0.5 %	± 1 %
Calibration	Type B	± 0.5 %		
Random (N=12000)	Type A	± 0.1 %		
Steel Temperature (FSO_E = 1100 ºC)				
Resolution	Type B	± 0.1 %	± 3.2 %	± 6 %
Calibration	Type B	± 0.4 %		
Installation	Type B	± 2.0 %		
Random (N=12000)	Type A	± 2.4 %		
Concrete Temperature (FSO_E = 1040 ºC)				
Resolution	Type B	± 0.1 %	± 4.1 %	± 8 %
Calibration	Type B	± 0.4 %		
Random (N=12000)	Type A	± 2.8 %		

Measurement / Component	Uncertainty Type	Standard Uncertainty	Combined Standard Uncertainty	Total Expanded Uncertainty (k=2)
Gas Temperature (FSO_E = 1200 ºC)				
Resolution	Type B	± 0.1 %		
Bias	Type B	± 0.4 %	± 4.1 %	± 8 %
Radiative cooling or heating	Type B	± 4.0 %		
Random (N=12000)	Type A	± 0.4 %		
Construction Dimensions (FSO_E = 9.1 m)				
Resolution	Type B	± 0.1 %	± 0.2 %	± 0.5 %
Misalignment	Type B	± 0.2 %		
Random*	Type B	± 0.1 %		
Weight (FSO_E = 2.1 kN)				
Resolution	Type B	± 0.1 %	± 1.2 %	± 2 %
Bias	Type B	± 0.1 %		
Random (N=2)	Type A	± 1.2 %		
Fuel Consumption Calorimetry (FSO_E = 10 MW)	Type B			± 1.4 %
Oxygen Consumption Calorimetry (FSO_E = 10 MW)	Type B			± 8 %

***** Uncertainty was calculated as Type B, using engineering judgement, considering an error of 1 cm in the measurement of 9.1 m.

3. Test Results

This chapter describes the third compartment fire experiment (Test #3) conducted on the 9.1 m by 6.1 m composite floor assembly, data (including average values and standard deviation where applicable) and observations from the heating and cooling phases of the test fire. The error bars shown in the figures of this manuscript are the maximum standard deviations of the measurements used to calculate the averaged values. The estimated relative uncertainty of the individual measurements are provided in Section 2.5. The raw data are presented in Appendix A.

3.1. Test Protocol

The following test protocol was used in this experiment:

1. Increase a total mechanical load to 125 kN at ambient temperature using four servo-hydraulic actuators.
2. Ignite pilot flames of the burners and increase natural gas flow to ignite the burners. The heat release rate of the burners (HRRburner) was initially set to 1000 kW for approximately 2 min to verify the uniformity of natural gas flow to all four burners.
3. Increase the value of HRRburner following the pre-determined HRRburner versus time relationship, which was designed to increase an upper layer temperature following the furnace temperature-time relationship prescribed in the ASTM E119 standard [10].
4. Remove the fire and hydraulic loading when any of the following criteria was met: (i) detachment of the beam-to-column connection(s), (ii) breach of the fire test compartment (a test floor assembly, enclosing walls, or both), (iii) actuator piston stroke reaching its maximum of 690 mm, (iv) loss of exhaust hood flow, or (v) failure of the data acquisition system network connection for a period exceeding 5 min.

Table 10 provides key events during the fire test experiment, where the reported times are rounded to the nearest minute. As shown, unloading of actuator loads was started at 140 min and the burners were switched off at 142 min.

Table 10. Timeline of Test #3 on February 3rd, 2022.

Clock Time	Fire Exposure Time	Description
10:23 AM		Hydraulic loads of actuators began to ramp up
10:46 AM		Target actuator load was reached
12:02 AM	0 min	The burner ignition was confirmed
2:22 PM	140 min	Unloading of actuators was started
2:23 PM	141 min	Unloading of actuators was completed
2:24 PM	142 min	The burners were switched off; See Fig. 15

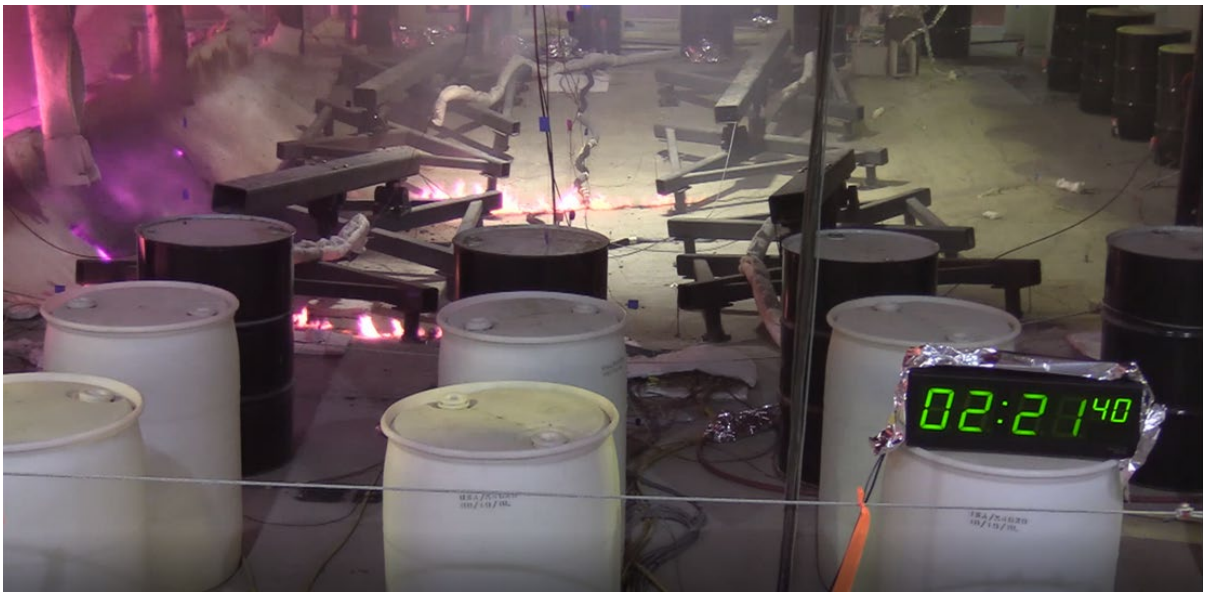

Fig. 15. Snapshot from the test video showing top of the test floor specimen at 142 min (2 hr:22 min) after the burner ignition. The pink color at the left side of this image is a camera artifact.

3.2. Fire Test Condition

This section describes the mechanical loading and fire conditions created during Test #3.

3.2.1. Mechanical Loading

A total of four hydraulic actuators (name: NE, NW, SE, and SW) were used to apply mechanical loads distributed at 24 points across the test bay. Locations of the hydraulic actuators and the raw data including loads and displacements applied using individual actuators are provided in Appendix A.1. The average value of applied loads and stroke displacements from four actuators are shown in Fig. 16. Four actuators increased a mechanical load simultaneously to a target value of 31 kN each at ambient temperature. This load level was then maintained throughout the heating phase of the test fire. The maximum variation in the load values from four actuators was 2.4 kN at ambient temperature. During the heating phase of the test fire, the load values varied by 0.5 kN. The total load applied using four actuators was maintained at (122.9 ± 0.2) kN, where the value after ± indicates the standard deviation.

As shown in Fig. 16b, the north half of the test floor slab loaded by the NE and NW actuators exhibited smaller displacements than the south half of the floor loaded by SE and SW actuators throughout the test period due to slab continuity to the north surrounding bay. During heating, the boundary (support) conditions of the test floor assembly was maintained symmetrical about its north-south (transverse) centerline. The maximum variation in actuator displacement values before the unloading of actuators during the heating phase was estimated 29 mm between the NE and NW actuators and 4 mm between the SE and SW actuators.

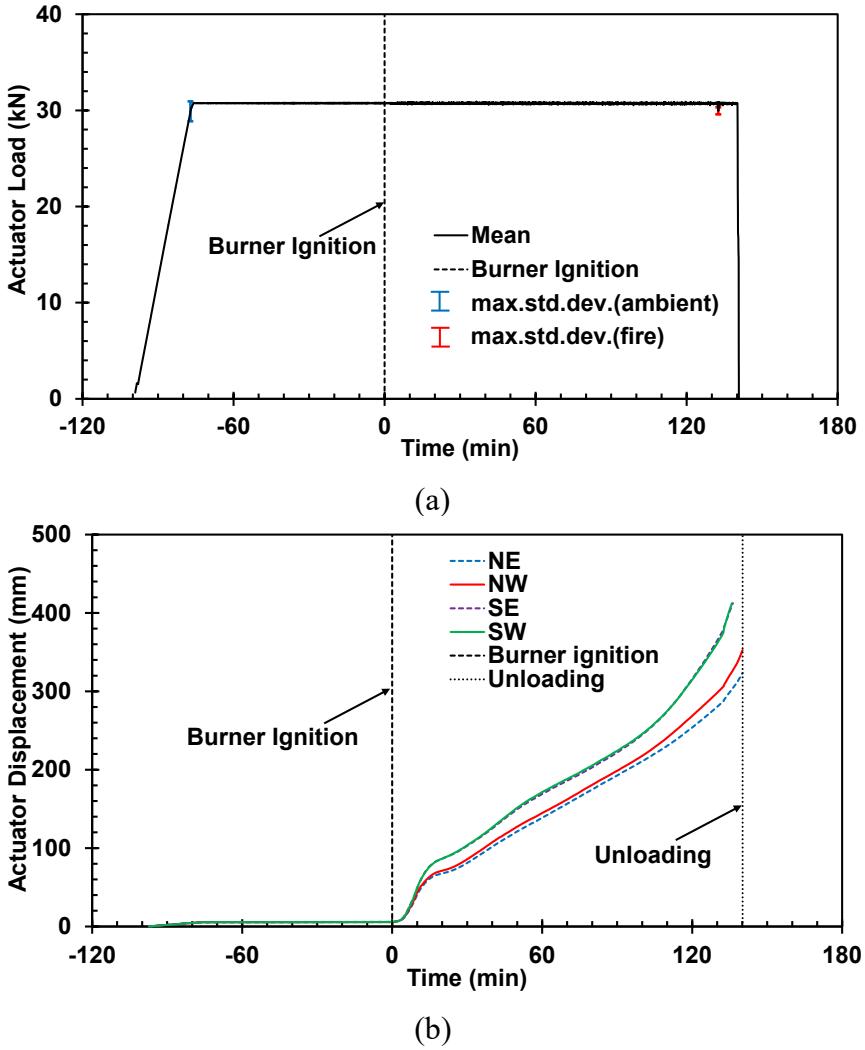

Fig. 16. (a) Average load applied by a single actuator and (b) stroke displacement of the actuators.

3.2.2. Test Fire

The test fire environment was created using four natural gas burners (1 m × 1.5 m each) distributed on the floor of the test compartment. The heat release rates and compartment temperatures recorded during the heating and cooling phases of the test fire is presented in the following subsections.

3.2.2.1. Heat Release Rate

The heat release from the test fire was measured using two methods: (a) the natural gas fuel consumption based on mass flow to the burners (channel: HRRburner) and (b) the oxygen calorimetry at the 20 MW exhaust hood (channel: HRR) as described in Bryant and Bundy [29]. The HRRburner and HRR data are provided in Fig. 17. The natural gas fire was controlled using the pre-programed fuel flow function to create the HRRburner versus time relationship. As

shown in Fig. 17, the HRR values were approximately 450 kW greater than the HRRburner values after the HRR ramping period of approximately 11 min.

Table 11 shows a summary of the measured peak heat release rate, total heat energy, and fuel load density that was estimated as the total heat energy divided by the floor area of the test compartment. The difference of the peak heat release rate between the natural gas fuel delivery system and oxygen calorimetry was approximately 10 % at 12 MW. A photograph of the test building captured during fire loading is shown in Fig. 18.

Table 11. Measured total heat release and fuel load density.

Method	Peak heat release rate (kW)	Total heat energy (MJ)	Fuel load density (MJ/m^2)
Oxygen calorimetry	12660	92310	1420
Fuel consumption	11460	87860	1350

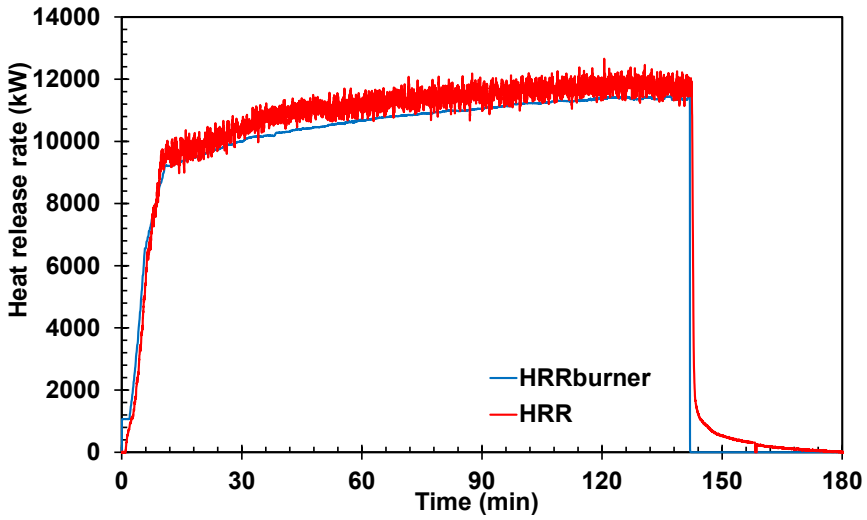

Fig. 17. Measured heat release rate (HRRburner and HRR).

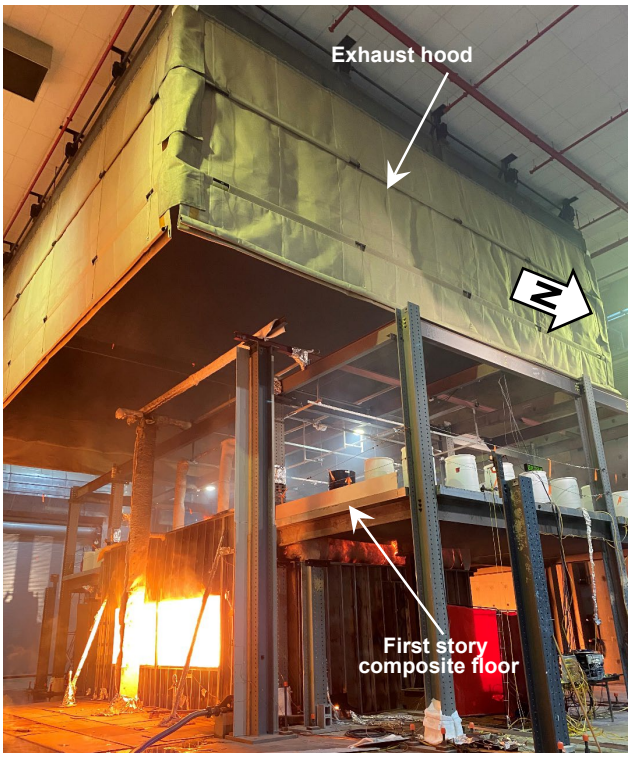

Fig. 18. A photograph of the test structure during the test.

3.2.2.2. Gas Temperature

Gas temperatures inside the test compartment were measured 30 cm below the floor specimen soffit (i.e., 346 cm above the compartment floor) using twelve thermocouples as well as two thermocouple trees mounted on the compartment floor. Locations of individual thermocouple probes and raw data are reported in Appendix A.2.

The natural gas fire created practically uniform upper layer gas temperatures to heat the floor specimen soffit, as shown in Fig. 19a. The standard deviation in the temperature measurements across the test bay was less than 50 °C during heating. The average upper layer gas temperature (AvgULG) variation with the fire exposure time measured in this test was close to that measured in Test #2. It was approximately 10 % higher than that specified in ASTM E119 [10] standard and approximately 5 % higher than the temperature measured in Test #1. This difference was caused by the house natural gas supply pressure during fire loading. The incoming natural gas pressure was measured 160 kPa (23 psig) in Test #1 but 170 kPa (25 psig) in Test #2 as well as in Test #3. Although the control valve position settings of the natural gas fuel delivery system were almost identical between the tests (within 1% difference), the elevated supply gas pressure in Test #2 and Test #3 increased the actual fuel mass flow by 6 % and subsequently increased the HRRburner value by 0.5 MW. The average upper layer gas temperature reached a peak value of 1120 °C at 142 min, when the burners were switched off.

A comparison of the gas temperature measured at three different heights within the test compartment, i.e., 100 cm, 200 cm, and 300 cm above the ground floor, as well as the upper layer temperature measured at 350 cm is shown in Fig. 19b. As shown in the figure, the gas

temperatures measured at and above 200 cm were close with a temperature difference of approximately 30 °C on average after 1 hr of fire exposure. The temperatures measured at 100 cm were approximately 65 °C lower on average after 1 hr of fire exposure.

Air flow through the windows of the test compartment was measured using a set of bi-directional probes with pressure transducers during fire loading. Refer to Appendix A.9 for locations of the sensors as well as velocity and gas-phase temperatures measured across the south and north windows of the test compartment.

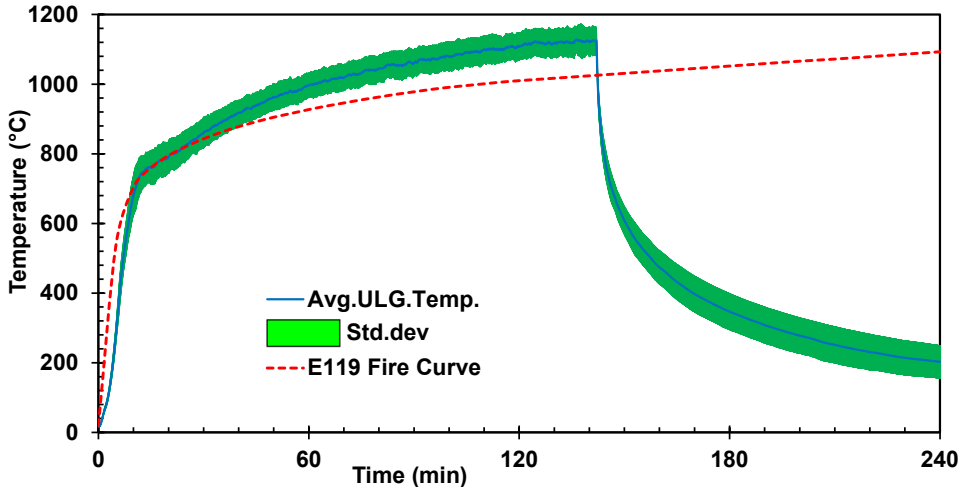

(a)

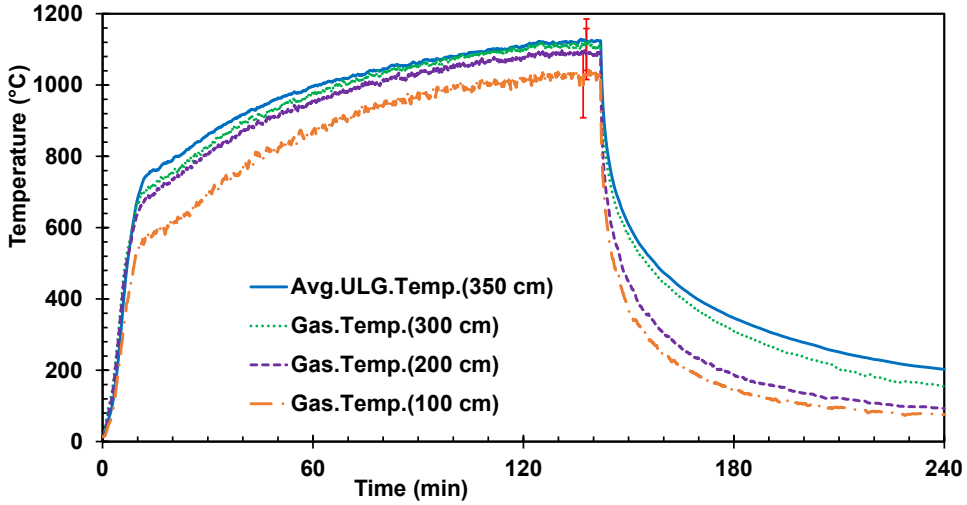

(b)

Fig. 19. (a) Average upper layer temperature (b) gas temperature measured at different elevations inside compartment.

3.3. Thermal Response

This section describes temperatures of the test floor assembly measured at a variety of locations during the heating and cooling phases of the test fire. Most of the data presented herein are the average values of temperatures measured by multiple thermocouples. All thermocouple locations and raw temperature data are reported in Appendix A.3 through A.6.

3.3.1. Concrete Slab and Steel Reinforcing Bars

The averaged values of concrete temperatures measured within the floor slab with profiled steel decking are illustrated in Fig. 20. Refer to Appendix A.3 for locations of individual thermocouples, a list of temperature channels used to compute the average values of measured concrete temperatures reported in this section, and the corresponding standard deviation of the averages.

As shown in Fig. 20, the change in concrete temperatures varied with the measurement locations (1 through 7) within the test floor slab. The concrete temperature near the exposed deck (locations 4 and 7) reached 750 °C on average during the fire exposure. Temperatures closer to top of the slab increased more slowly but increased continuously during the early cooling phase. Temperatures measured at locations 1 and 2 were significantly influenced by evaporation of the moisture driven out toward the top of the slab during heating, as indicated by a 100 °C plateau. The magnitude of error bars indicates that the larger variation in temperatures was observed at locations 4, 6, and 7. These temperature measurements appeared to be affected by several factors, such as the separation of concrete from the steel decking, concrete cracks, or combined effects. Temperatures measured at the mid-depth of the topping concrete in the test bay varied due to the concrete mass below. For instance, the temperature measured at location 1 and 6 was 270 °C and 590 °C at 132 min, when the transverse crack started to develop in the mid-panel region, respectively.

A total of twelve thermocouple probes were mounted 3 mm below the top surface of the concrete slab. The average values of temperatures measured at the top of the deep (using four thermocouples) and shallow (using four thermocouples) concrete slab sections are plotted in Fig. 21a. The average top surface temperature of the deep concrete section reached 110 °C at 142 min, when the burners were switched off. The average top surface temperature of the shallow concrete section reached 180 °C at 142 min. The average top surface temperature, calculated using four thermocouple probes at deep section and four thermocouple probes at shallow section, reached 147 °C at 142 min, i.e., 129 °C above the ambient temperature (18 °C) measured prior to the ignition of the test fire. This temperature is less than the ASTM E119 limit of 139 °C above the ambient temperature. The average top surface temperature reached a peak value of 170 °C at 200 min, 58 mins into cooling.

The average temperatures of No. 3 deformed bars placed within the deep and shallow sections of the test floor slab are shown in Fig. 21b. The peak temperature of the bars in the deep section reached about 320 °C on average about 10 min after the test fire was extinguished, whereas the bars embedded in the shallow section were heated to 600 °C at 3 min after the test fire was extinguished. The large error bars in Fig. 21b was the result of large differences between the bar temperatures measured in the mid-slab region and the bar temperatures measured away from the mid-slab region, attributed to cracking in the bottom part of the concrete slab in the mid-slab

region when the specimen deflected downward. Refer to the raw data used to estimate the average temperatures of No. 3 deformed bars and the location of thermocouples used to measure the raw data presented in Appendix A.4 for more details.

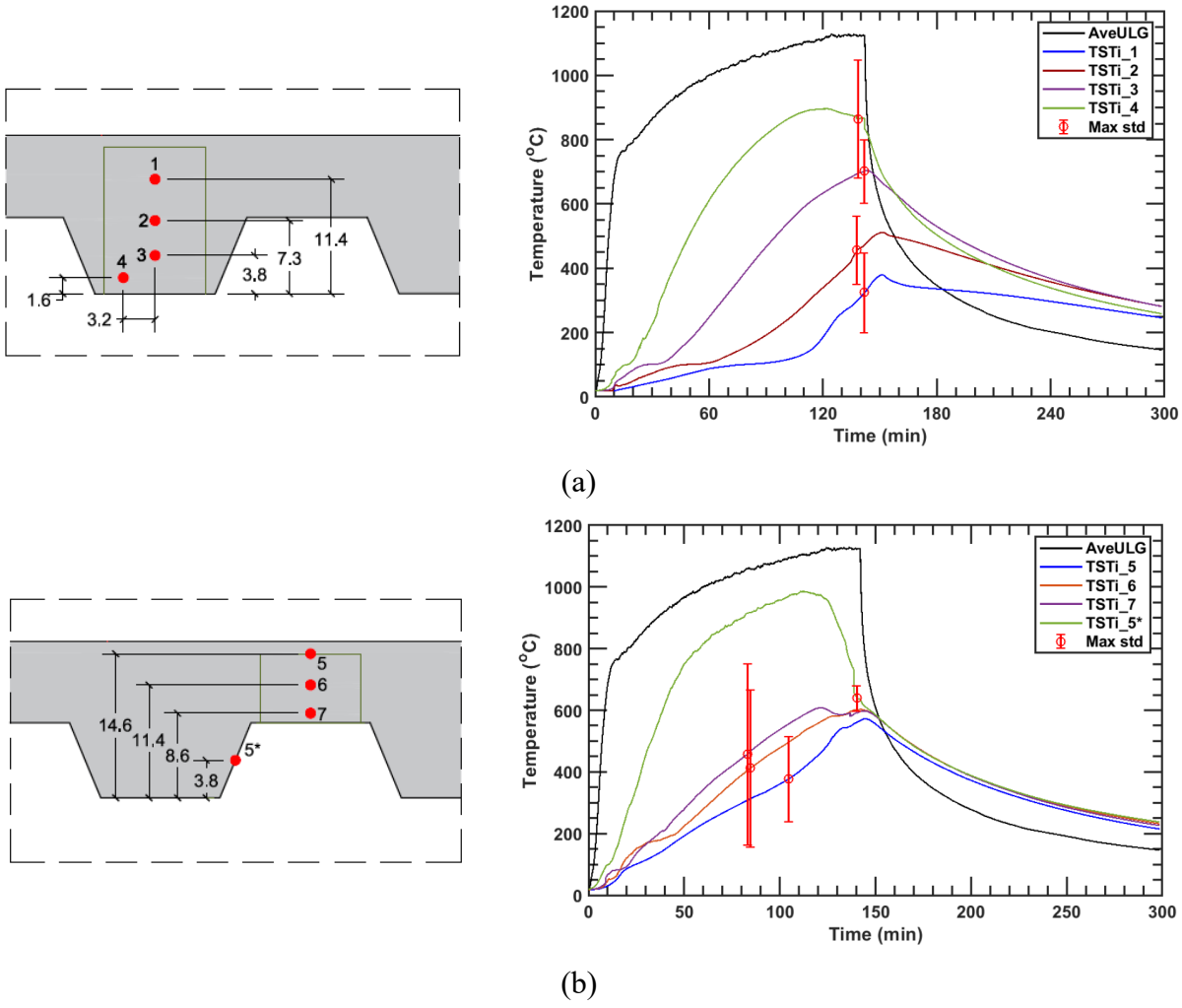

Fig. 20. Average temperatures of concrete slab (a) 15.9 cm deep sections and (b) 8.3 cm deep sections of the test floor slab. Error bars indicate the maximum standard deviation of temperatures recorded from multiple thermocouples installed at the same distance from the steel deck. Dimensions are in cm.

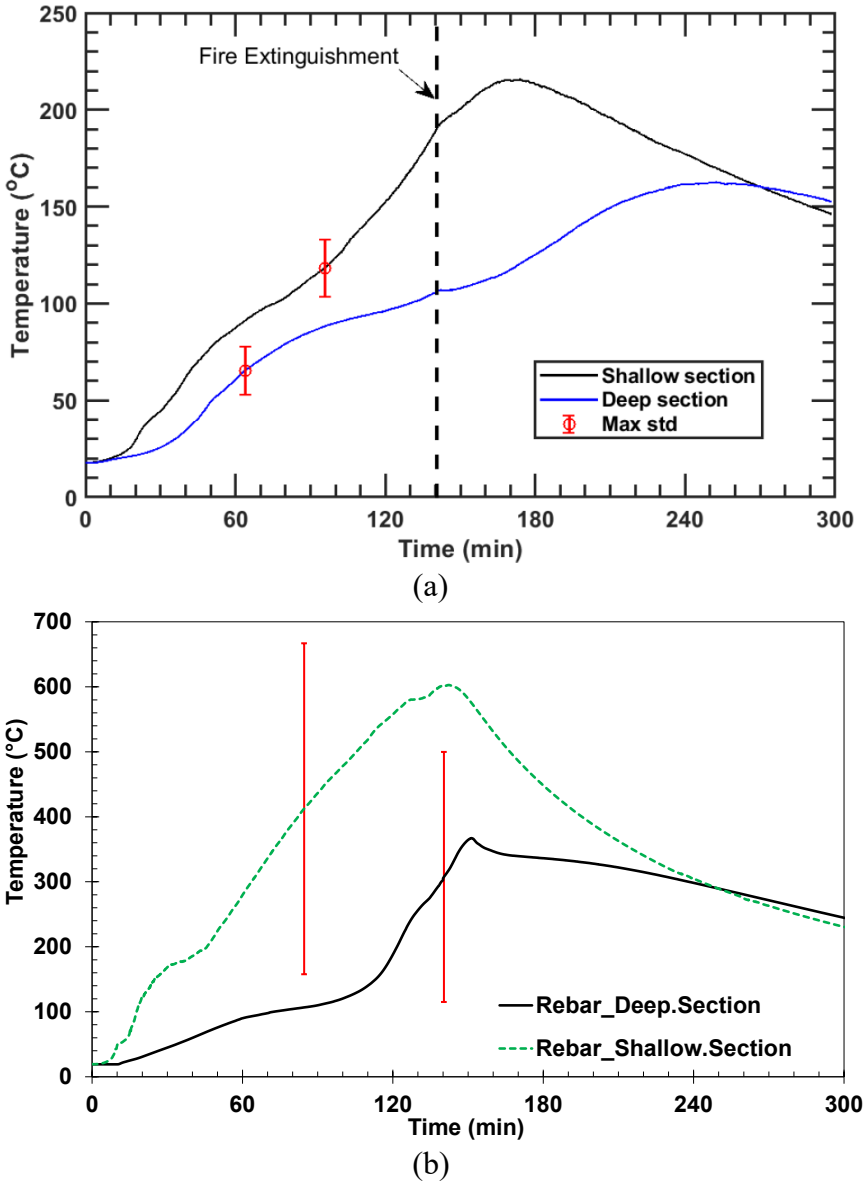

Fig. 21. Average temperature measured 3 mm below the top (unexposed) surface of composite slab; (b) average temperatures of No. 3 deformed bars within the test floor slab

3.3.2. Composite Beam and Girder

Temperatures of the 9.1 m span composite beams (W16×31) and 6.1 m span composite girders (W18×35) within the fire test bay were measured across the midspan cross section, as shown in Fig. 22. Temperatures of all five steel beam shapes and the topping slab are reported in Appendix A.4 and A.5.

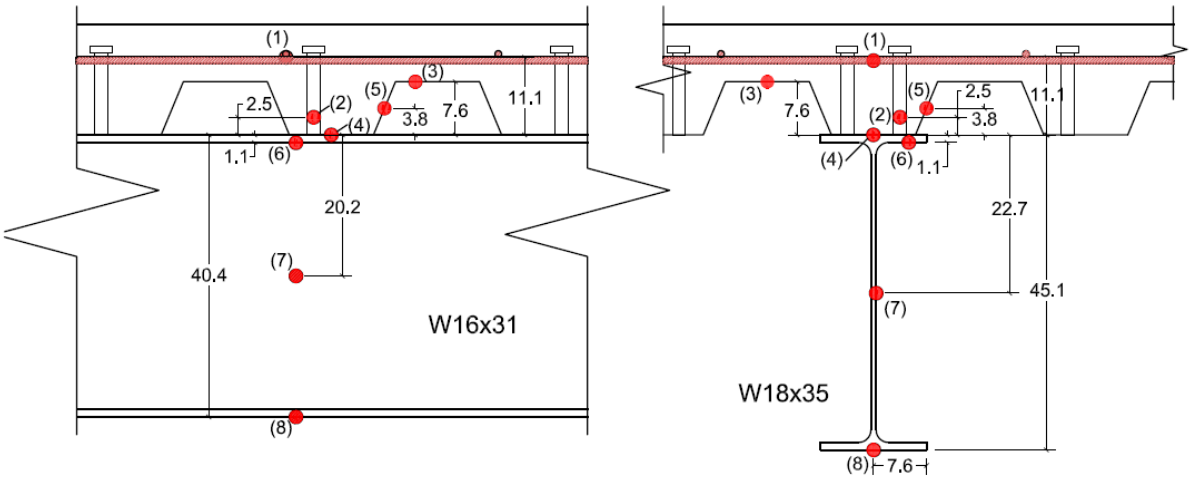

Fig. 22. Locations of thermocouple probes within the 9.1 m composite beam (W16×31) and the 6.1 m composite girder (W18×35) at midspan. Dimensions are in cm.

The typical temperature change across the composite beam sections is presented in Fig. 23. The 9.1 m unprotected secondary beam temperatures (Fig. 23a) are the average values of temperature readings of three sections along the beam. The error bars indicate the maximum value of the standard deviations of the temperature readings used to calculate the averages. The 9.1 m SFRM protected composite beam temperatures (Fig. 23b) are the average values of temperature readings of the north and south beams at midspan. Similarly, the composite girder temperatures in Fig. 23c are the average temperature values of the east and west girders at midspan. As shown, during the fire exposure, the average temperatures of the unprotected secondary beam were close to the upper layer gas temperature and reached a peak value of 1100 °C at 142 min when the burners were shut off. The average temperatures of the stud anchors and No. 3 reinforcing bars above the secondary beam reached 720 °C and 460 °C at 142 min, respectively. At the same time, the temperatures of the 9.1 m long SFRM-applied W16×31 shapes reached a peak value of 940 °C at the bottom flanges and 590 °C at the top flanges on average. The temperatures of the 6.1 m long SFRM-applied W18×35 shapes reached 1030 °C at both the bottom flanges and reached 800 °C at the top flanges on average at 142 min.

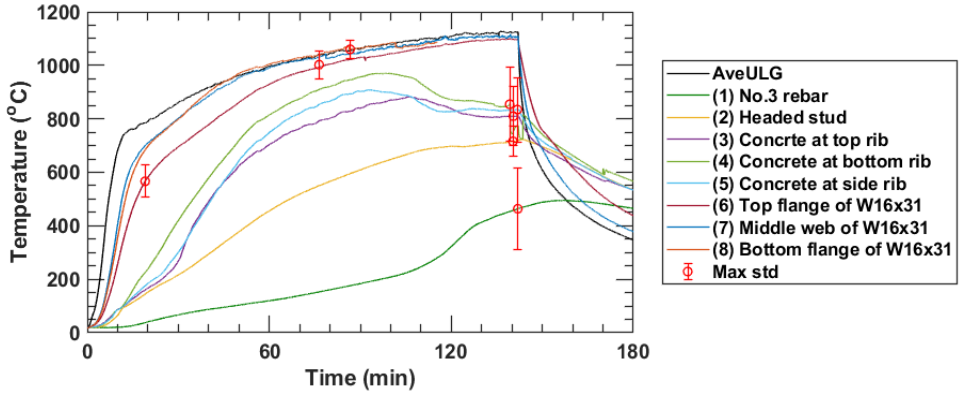

(a)

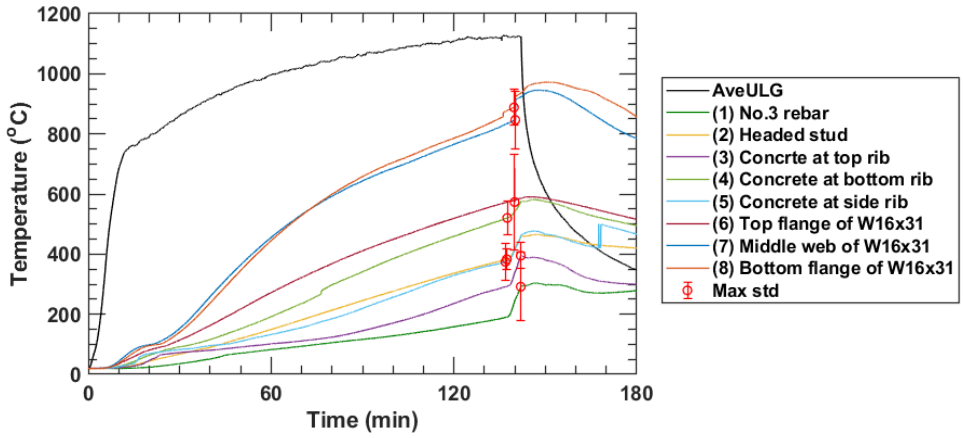

(b)

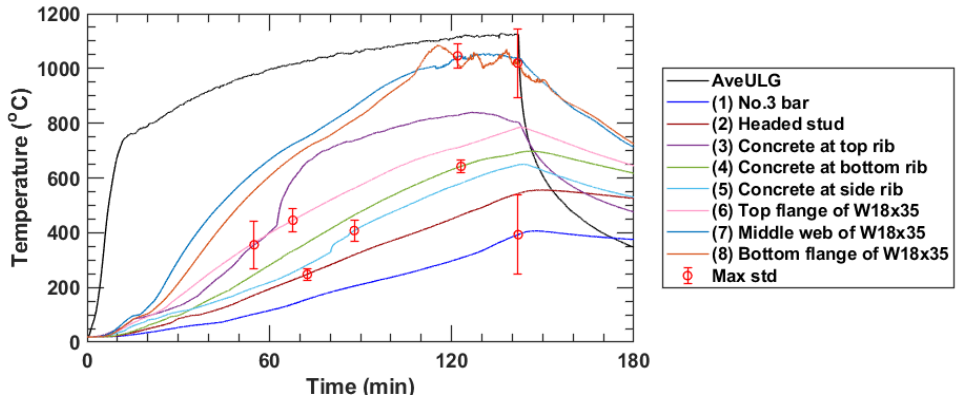

(c)

Fig. 23. Average temperatures of (a) 9.1 m unprotected secondary beam; (b) 9.1 m SFRM protected composite beams; (c) 6.1 m SFRM protected composite girders at midspan.

3.3.3. Beam-End Connection

The shear connections at the end of north and south primary beams as well as at the end of east and west girders of the fire test bay were protected with the same SFRM used for the connected beams and girders. The connections at the end of secondary beam were left unprotected. Refer to

Sect. 2.3.2 for the thickness of applied SFRM. Typical locations of the thermocouples mounted on the shear-tab connections of the floor beams are shown in Fig. 24. The average temperatures of the beam-end and girder-end connection regions are provided in Fig. 25 and Fig. 26, respectively. Temperatures of all ten connections exposed to fire are reported in Appendix A.6.

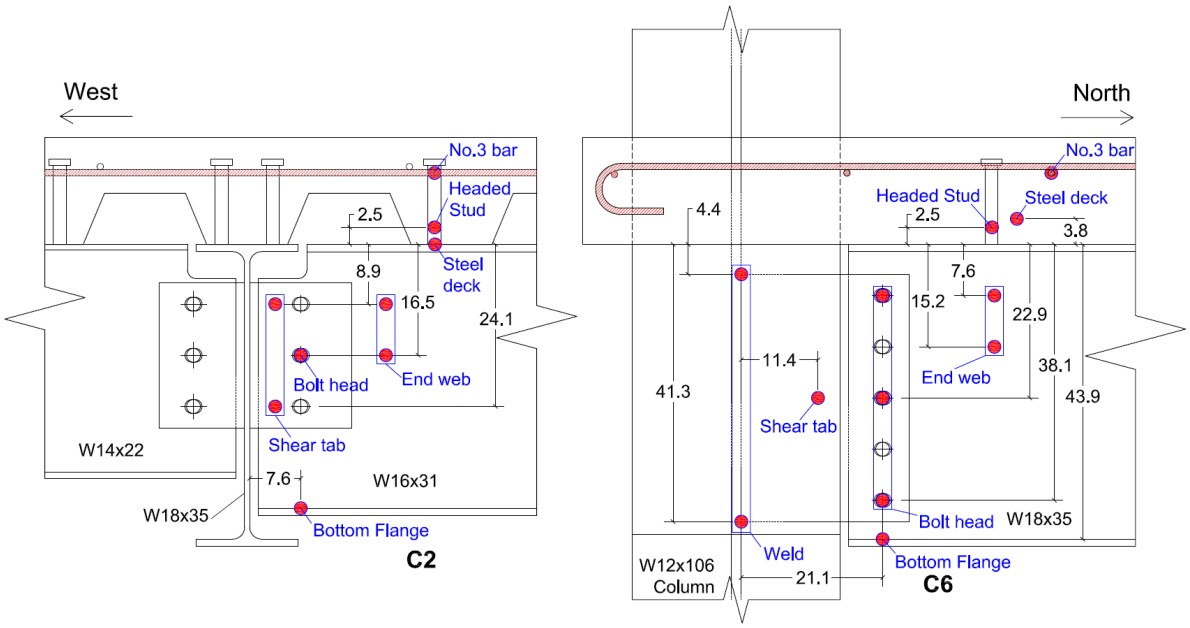

Fig. 24. Typical locations of temperature measurements in the beam-end (left) and girder-end (right) connection regions.

As shown in Fig. 25, the connection at the end of secondary beam was heated more rapidly than other connections as it was left unprotected and due to its proximity to the burners. The temperature of the end web region, shear tab plate, and bolt heads reached 1100 °C at 142 mins on average. Temperatures of the same connection at the north and south beam ends remained below 800 °C and 710 °C, respectively. The No. 3 reinforcing bar over the secondary beam connections sharply increased after 114 mins, indicating concrete cracks. It reached 410 °C at 142 mins, when the burners were switched off.

Figure 26 shows the temperatures measured at the girder end-connection regions. Beam end web, bolt head, and shear tab plate reached 820 °C, 655 °C, 530 °C on average at 142 mins. The temperatures of the welded joints remained below 400 °C, because thermocouples in those regions were shaded by the column flanges.

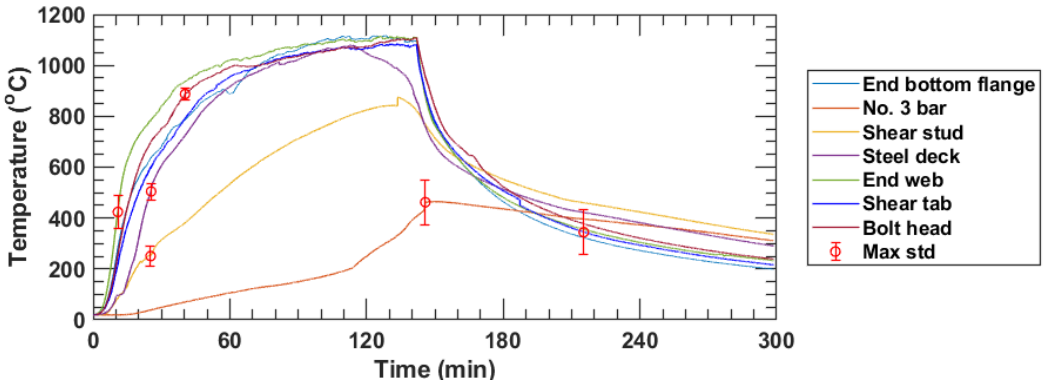

(a)

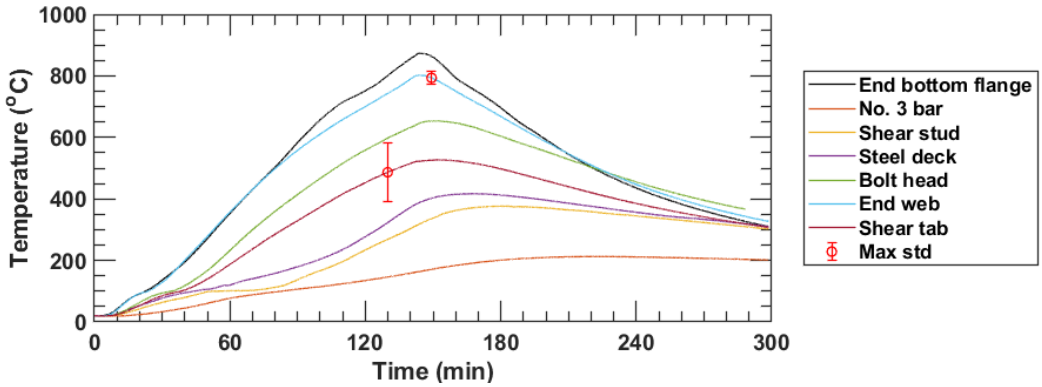

(b)

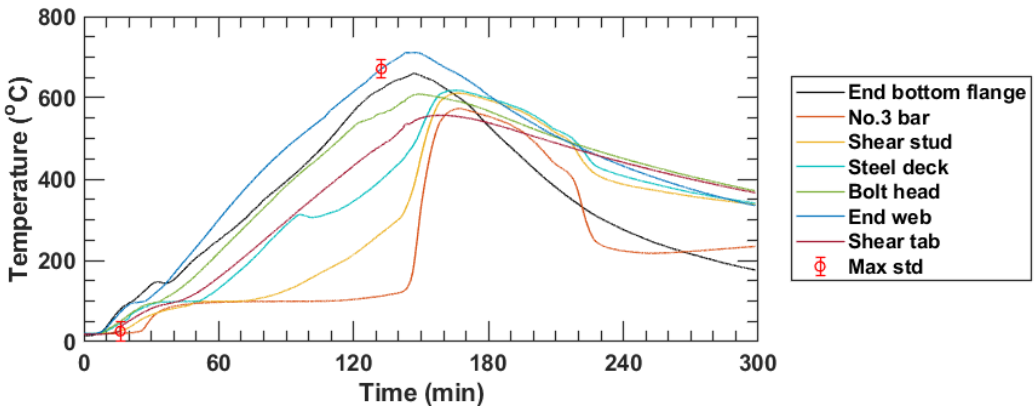

(C)

Fig. 25. Average temperatures of the beam-end connections of (a) secondary beam; (b) north edge beam; (c) south edge beam with W16x31 shapes. Error bars indicate a maximum value of standard deviation of temperatures measured at multiple locations.

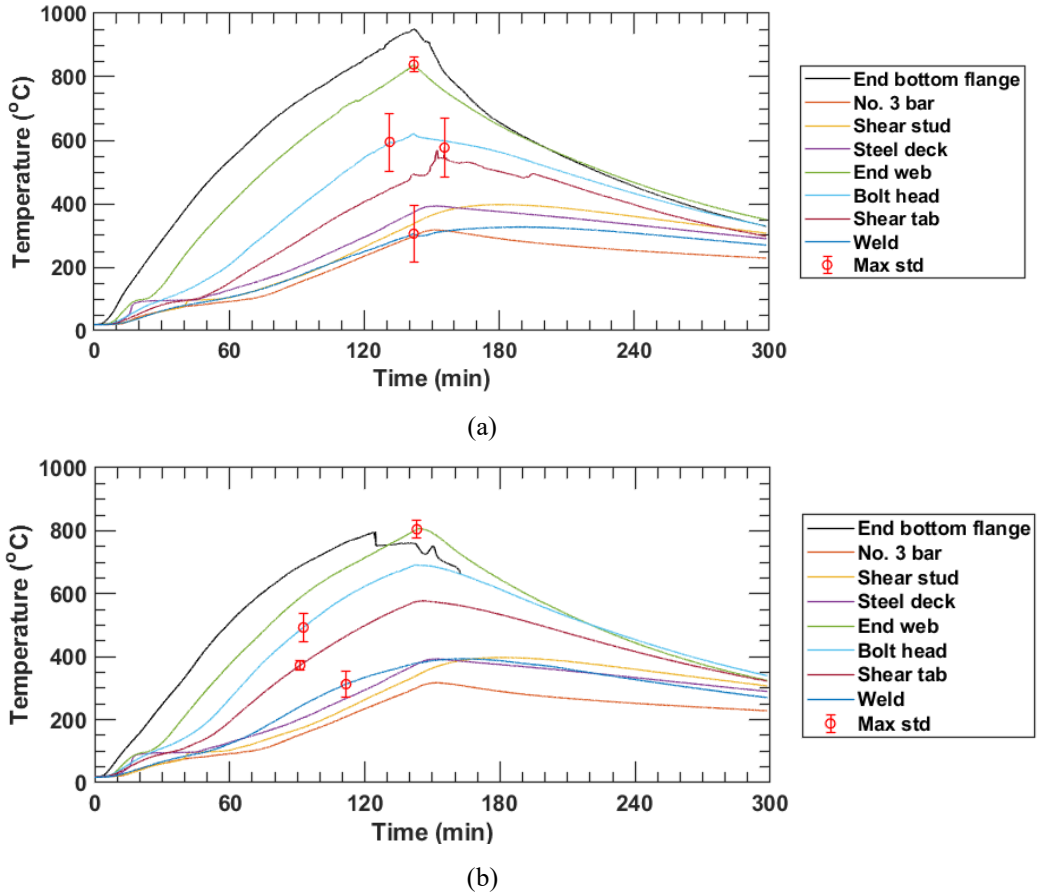

Fig. 26. Average temperature of (a) east girder end connection and (b) west girder end connection attached to W18x35 shapes. Error bars indicate a maximum value of standard deviation in temperatures measured at multiple locations.

3.4. Structural Response

This section presents the vertical and horizontal displacements of the hydraulically loaded composite floor assembly during the heating and cooling phases of the test fire. The displacement data not reported in this section and strain measurements of the support columns and surrounding beams of the two-story test building are included in Appendix A.7 and A.8, respectively.

3.4.1. Vertical Displacement

A total of thirteen displacement transducers (named VD1 through VD11, VD13, and VD14) were deployed to measure the vertical deflection of the test-bay and surrounding floors as shown in Fig. 27. Some vertical displacements are plotted with fire exposure time and the average bottom flange temperatures of the floor beams, as illustrated in Fig. 28. Other displacements not presented in this figure are reported in Appendix A.7. The positive values of displacements indicate the downward vertical displacements as the test floor assembly sagged under fire exposure. The actuator loading was removed at 140 min of the fire exposure, whereas the test fire was extinguished at 142 min.

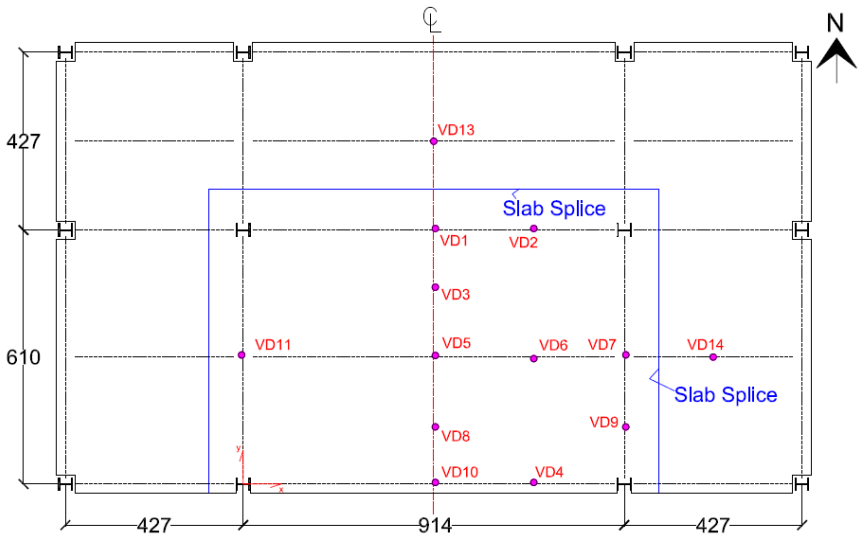

Name/ID	X East+	Y North+
VD1	461	613
VD2	697	309
VD3	461	472
VD4	697	4
VD5	461	309
VD6	697	301
VD7	918	310
VD8	461	137
VD9	918	137
VD10	461	4
VD11	4	310
VD13	461	823
VD14	1128	305

Fig. 27. Location of the vertical displacement (VD) measurements. Dimensions and coordinates are in cm.

As shown in Fig. 28a, the vertical displacement of the secondary beam at midspan (VD5) exhibited three distinct displacement rates over the heating phase of the test: (a) 13.4 mm/min between 4 min and 14 min of fire exposure, (b) 3.1 mm/min between 14 min and 132 min, and (c) 13.9 mm/min between 132 min and 140 min. The first displacement rate between 4 min and 14 min indicates thermal bowing as well as significant loss of flexural strength of the unprotected secondary beam heated to approximately 530 °C. The displacement rate change at 132 min indicates the development of transverse crack in the mid-panel region. VD5 reached a peak value of 655 mm (equivalent to the ratio of L/14 where L = 9.1 m) at 140 min, the time at which unloading of actuators was started. The floor specimen reached the ASTM E119 limiting displacement (518 mm) at 129 min but did not reach the ASTM E119 limiting displacement rate of 23.0 mm/min.

As shown in Fig. 28a, the center of the south half panel of the test bay (VD8) showed a displacement-time response similar to VD5, reaching 640 mm at 140 min and a maximum of 645 mm at 150 min. The maximum displacements of the north beam (VD1), the east girder (VD7), and the west girder (VD11) were 225 mm, 95 mm, and 100 mm, respectively. The vertical displacements of the south edge beam at midspan (VD10) became invalid after 132 min due to the damage of string used for displacement sensor caused by fire.

Figure 28b shows the vertical displacements measured at the midspan of the test bay beams plotted with the bottom flange temperatures of those beams. The mid-panel vertical displacement (VD5) exhibited a linear gradient of 0.23 mm/°C until a bottom flange temperature increased to 850 °C (at 34.7 min). The increase in the VD5 value became approximately 1.0 mm/°C afterward. The vertical displacement of the south (exterior) edge beam (VD10) increased more rapidly after a bottom flange temperature of 650 °C than other edge beams (VD1, VD7 and VD11) because of their connectivity to the surrounding bays.

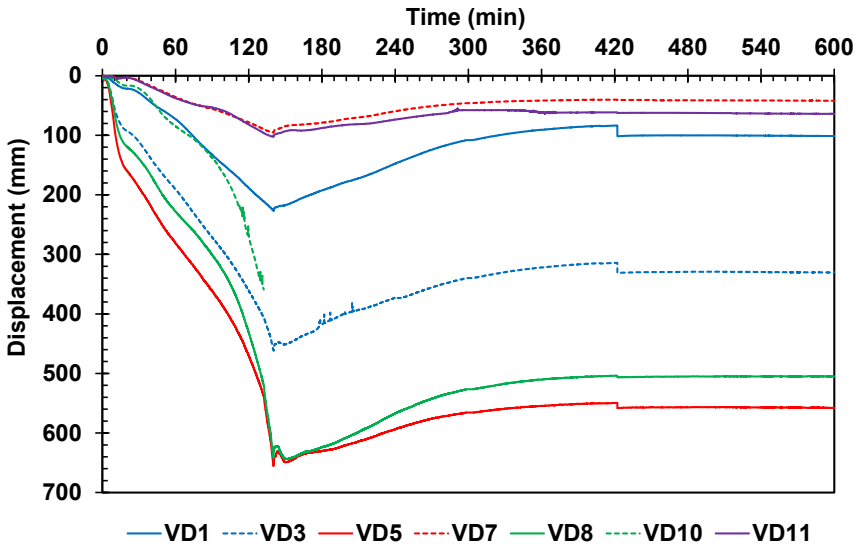

(a)

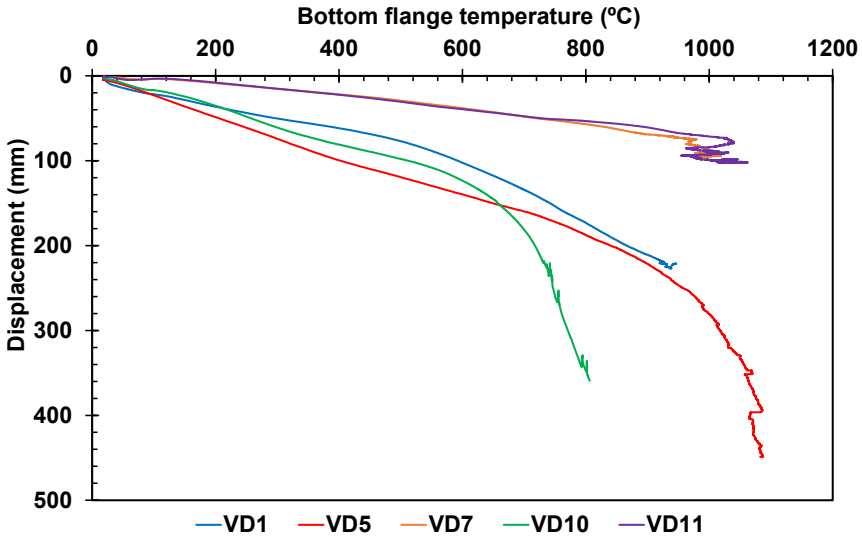

(b)

Fig. 28. Measured vertical displacements as a function of (a) fire exposure time and (b) bottom flange temperatures of the floor beams.

The temporal change in the vertical displacement measured along the longitudinal and transverse centerlines of the test bay is illustrated in Fig. 29. After 90 min of fire exposure, the south half of the floor specimen deflected more than its north half since the No. 3 deformed bars placed perpendicular to the north edge beam provided some degree of rotational restraints, maintaining a good continuity with the steel reinforcement placed in the north surrounding bay which remained cool during fire loading.

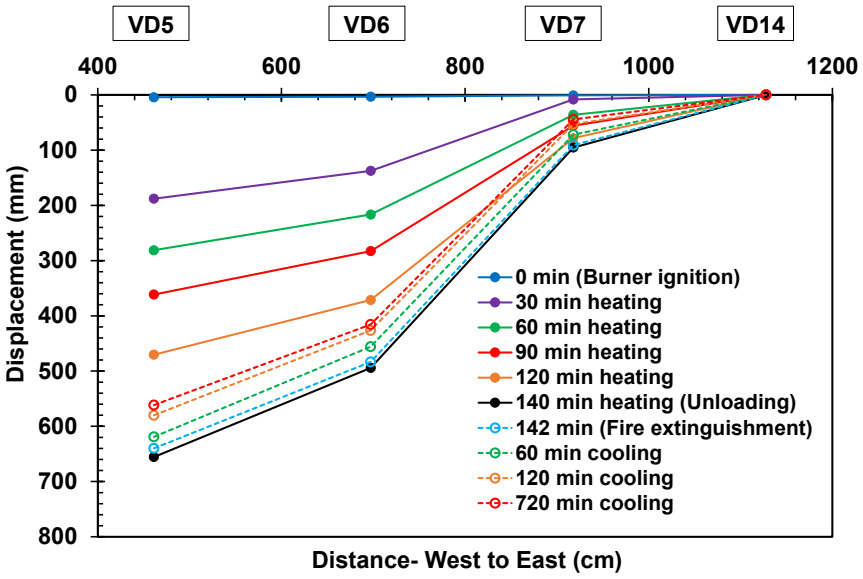

(a)

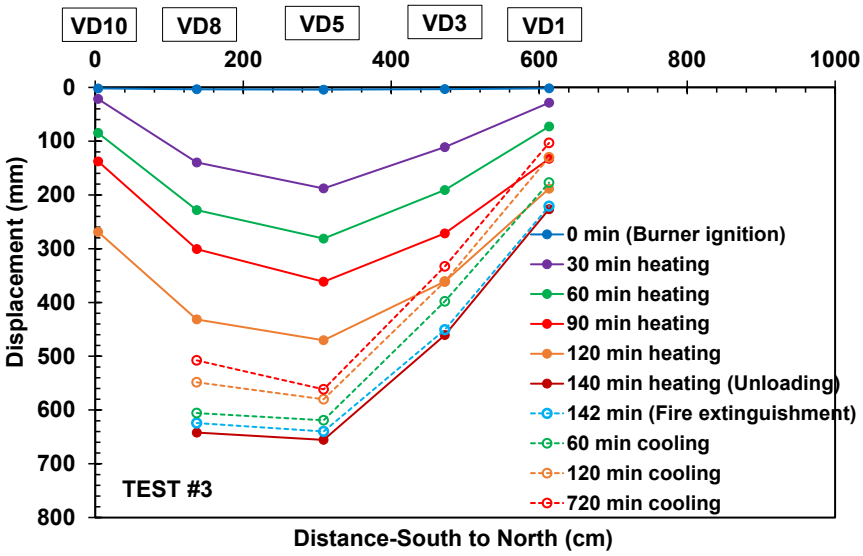

(b)

Fig. 29. Vertical displacement profile of the test floor assembly at (a) the east-west centerline; (b) the north-south centerline. The upper horizontal axes indicate the corresponding position of each vertical displacement sensors in reference to the origin at south west column of test bay.

3.4.2. Horizontal Displacement

A total of eighteen string potentiometers (HD1 through HD18) were deployed to measure the horizontal displacement of the test floor assembly and at the perimeter of the two-story prototype building; See Fig. 30. The HD4, HD6, HD18 sensors were used to measure thermal expansion of the north, east, and west edges of the fire test bay, respectively. The lateral displacements of the first-story columns (HD1 through HD3, HD5, HD8 through HD10, and HD16) as well as HD4, HD6, and HD18 were measured at 15 cm above the top surface of the test floor slab.

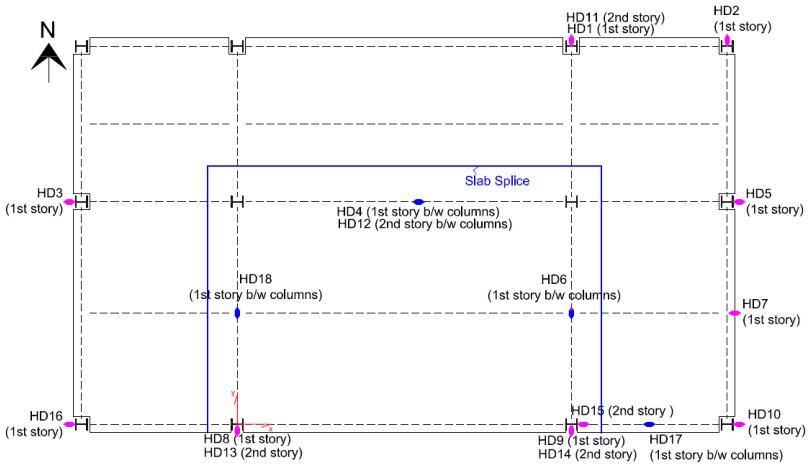

Name/ID	X East+	Y North+	Z Up+	Direction (+ value)
HD1	914	1037	412	North
HD2	1341	1037	412	North
HD3	-443	610	412	West
HD4	16	610	412	Expansion
HD5	1357	610	412	East
HD6	914	609	412	Expansion
HD7	1382	305	427	East
HD8	0	1	412	South
HD9	914	1	412	South
HD10	1357	0	412	East
HD11	914	1037	734	North
HD12	16	610	734	Expansion
HD13	0	1	729	South
HD14	914	1	729	South
HD15	931	0	734	East
HD16	-443	0	412	West
HD17	1325	0	412	East
HD18	0	594	412	Expansion

Fig. 30. Location of horizontal displacement (HD) measurements. The Z datum is defined at the laboratory strong floor. Coordinates are in cm.

Some horizontal (lateral) displacements, plotted as a function of time, of the exterior columns at the test floor level are illustrated in Fig. 31. Other displacements not presented in this figure are reported in Appendix A.7. As shown, approximately 8 min into fire loading, the displacements began to increase in the east or west direction due to thermal expansion of the test floor assembly. Simultaneously, the lateral displacement of the north column (HD11) at the second-story level increased toward south since this column was pulled together with the south columns deflecting toward the south during heating. The peak values of most of the lateral displacements occurred between 80 min and 100 min after the burner ignition suggesting local buckling at the end of the beams during this time and pulling back of the columns due to increasing downward displacement of the test bay slab.

The horizontal displacements of the floor specimen are plotted as a function of the bottom flange temperatures of the fire-exposed steel beams or girders in the test bay; See Fig. 32. HD4 as well as mean of HD3 and HD5 are plotted with the average bottom flange temperature of the north primary beam; HD7 is plotted with the average bottom flange temperature of the secondary beam; mean of HD10 and HD16 is plotted with the average bottom flange temperature of the south primary beam; HD1 is plotted with the average bottom flange temperature of the east girder; and mean of HD8 and HD9 as well as mean of HD6 and HD18 are plotted with the average bottom flange temperature of the east and west girders.

Thermal elongation along the north edge of the test floor (HD4) was approximately equal to two times the average displacement of the east and west exterior columns (HD3 and HD5), as shown in Fig. 32a. The displacement values along the north and south primary beams increased until a bottom flange temperature of approximately 600 °C was reached. The displacement values along the east and west girders increased until a bottom flange temperature of approximately 850 °C was reached.

With the presence of the north surrounding bay, the east and west edges of the test assembly thermally elongated mostly toward the south. As shown in Fig. 32b, the average thermal elongation of the east and west edges (HD6 and HD18, respectively) were very similar to the average lateral displacement of the southeast and southwest column of the test bay (HD9 and HD8, respectively). Beyond 850 °C, those displacements stopped increasing and began to slowly decrease until the test fire was removed.

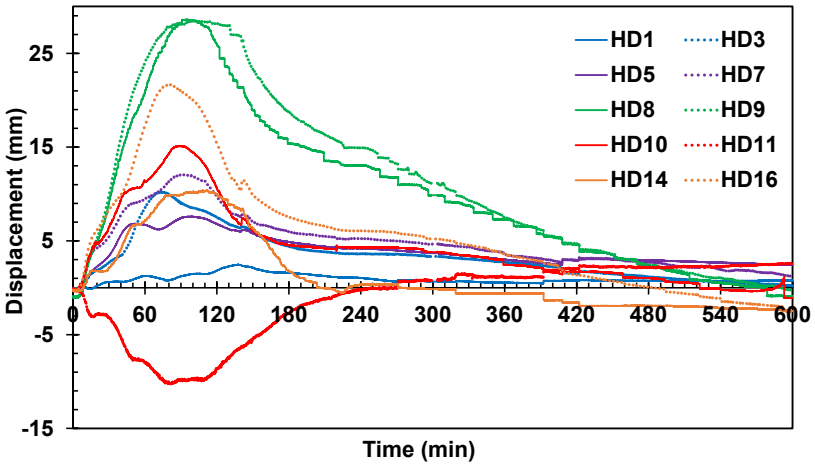

Fig. 31. Measured lateral displacements of the exterior columns.

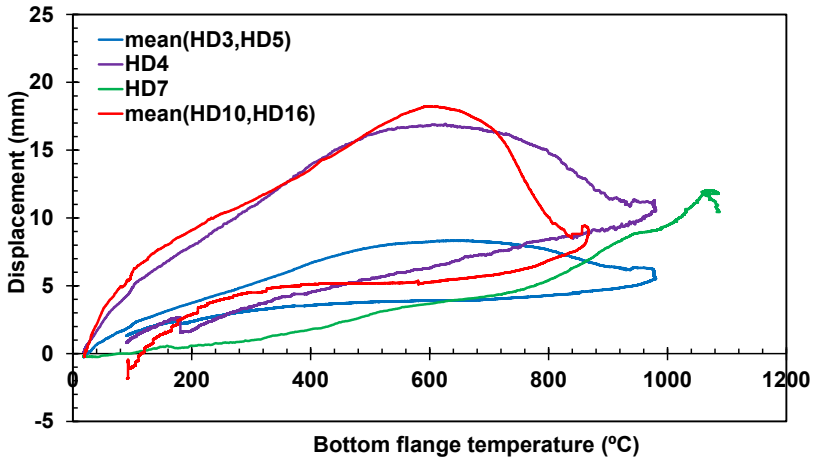

(a)

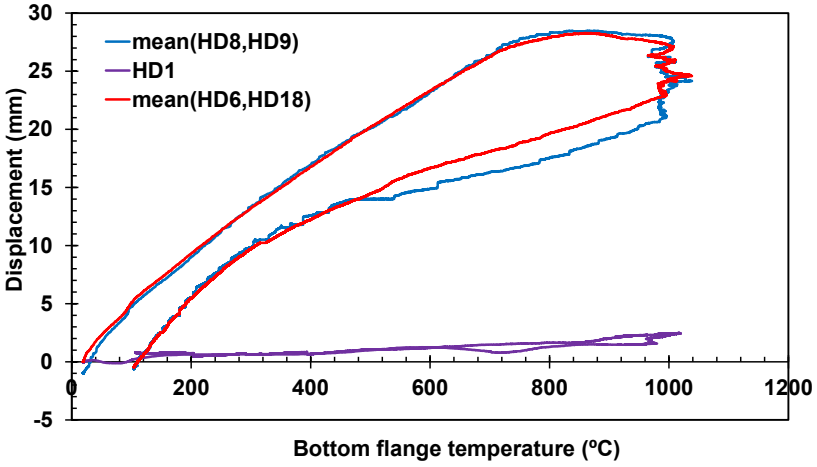

(b)

Fig. 32. Measured horizontal displacements as a function of bottom flange temperatures; (a) thermal elongation in the east-west direction and (b) thermal elongation north-south direction.

3.5. Post-Test Inspection

Several visual inspections were performed to examine structural damages of the fire-exposed floor specimen after cool-down. This section presents the final crack pattern of the concrete floor slab as well as deflections and local ruptures of the support beams, shear studs, and connections.

3.5.1. Concrete Slab

Fig. 33 and Fig. 34 show the deflected shape of the test floor after cool-down and concrete crack pattern on top of the floor specimen, respectively. As shown in Fig. 34, the concrete slab exhibited a large transverse crack opening, approximately 105 cm west of the transverse centerline of the test bay, with a maximum crack width after cooling of approximately 3.5 cm near the secondary beam. Most of the No. 3 reinforcing bars ruptured in this crack opening (Fig. 35) during the test. Flame leak above the slab through this transverse crack was observed after 132 min of fire exposure. The test floor exhibited cracks at other three locations (marked 2, 3, and 4 in Fig. 34) at 138 min of fire exposure, with flame leak above these cracks, although these cracks were smaller in size compared to the mid-panel transverse crack (marked 1). Concrete cracks at locations 2 and 3 also exhibited reinforcing bar fractures (Fig. 36). The test floor also exhibited cracks along the east, west, and north edges of the test-bay column grid (but within the footprint of the fire test compartment). The cracks along the west and east edges were larger toward the south columns but became smaller around the north columns. Along the west edge crack, the first five bars from the south end exhibited bar fracture (Fig. 37a and Fig. 37b) and the slab in that region lost continuity over the girders. The cracks along the east edge exhibited no bar fractures (Fig. 37c and Fig. 37d). Figure 38 shows the crack pattern in the north corners (locations 7 and 8) of the test floor and in the midspan of the north edge (location 9). The location of the north edge crack was about 64 cm from the north splice plate near the north-south centerline of the slab, indicating the development of that crack near the ends of the No. 4 reinforcing bars extended from the north splice plate. Those cracks did not exhibit any bar fractures. No cracks, bar slips, or bar fractures were observed in the regions of reinforcing bar splices, which were designed as ACI-318 [22] contact splices.

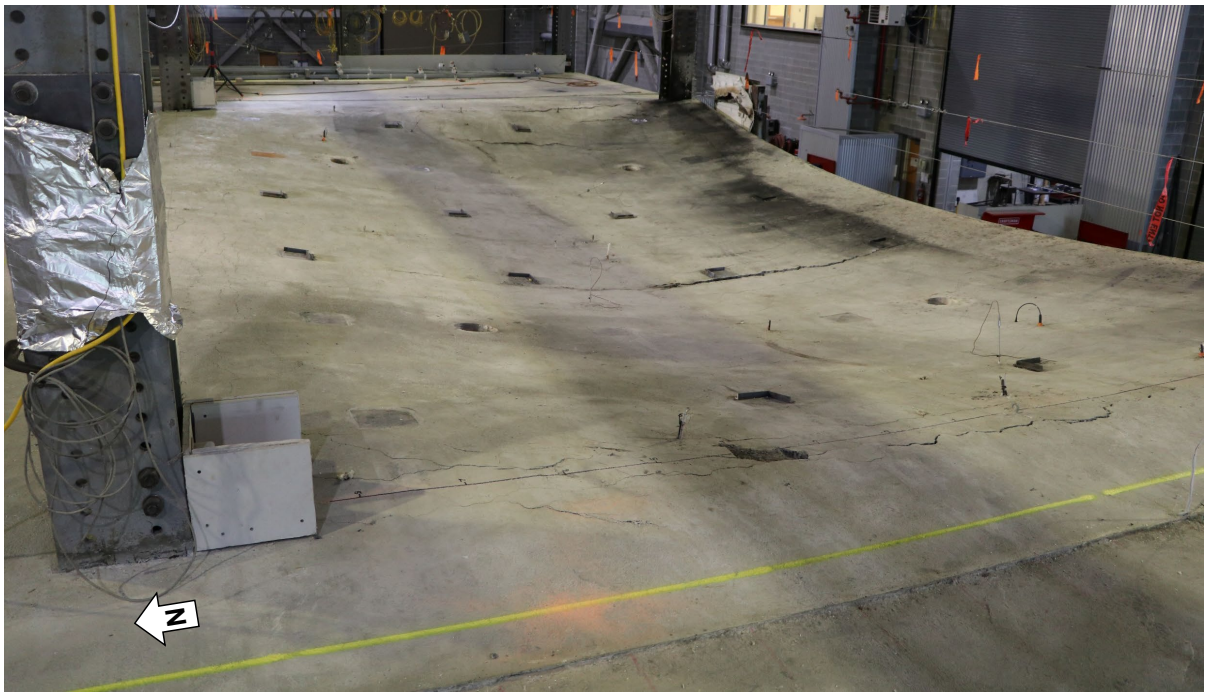

Fig. 33. Deflected shape of the test floor slab

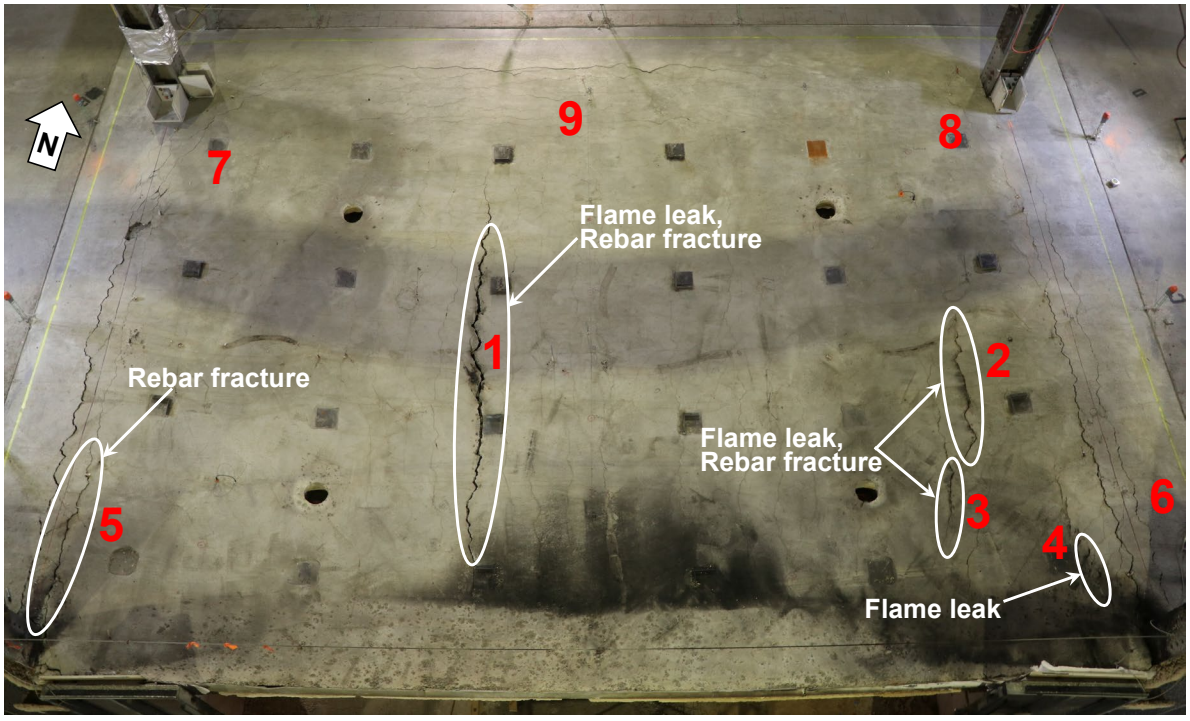

Fig. 34. Crack pattern on the test floor slab.

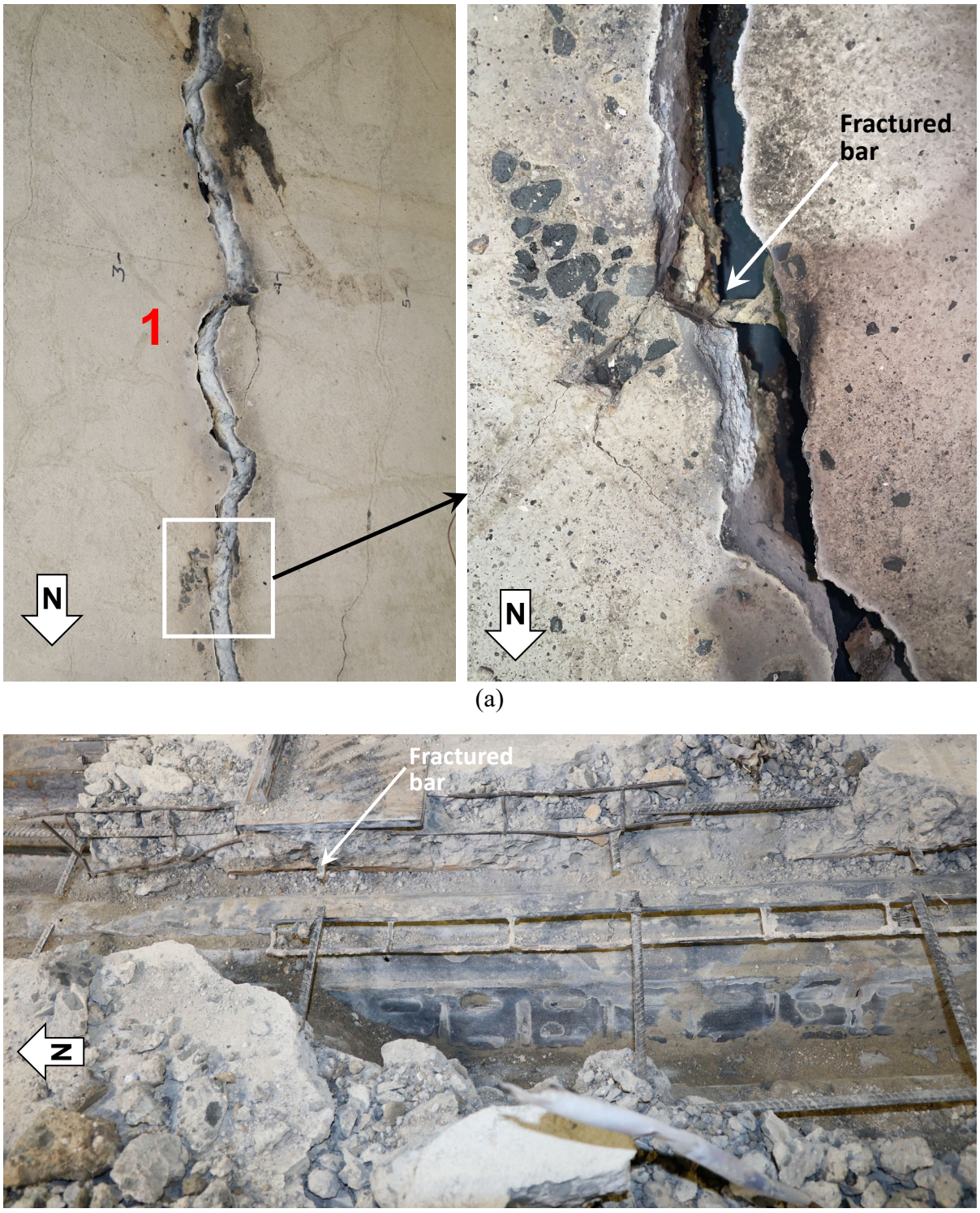

Fig. 35. (a) Transverse crack near mid centerline of the test floor slab (at Location 1 in Fig. 20); (b) rebar fractures across the transverse crack.

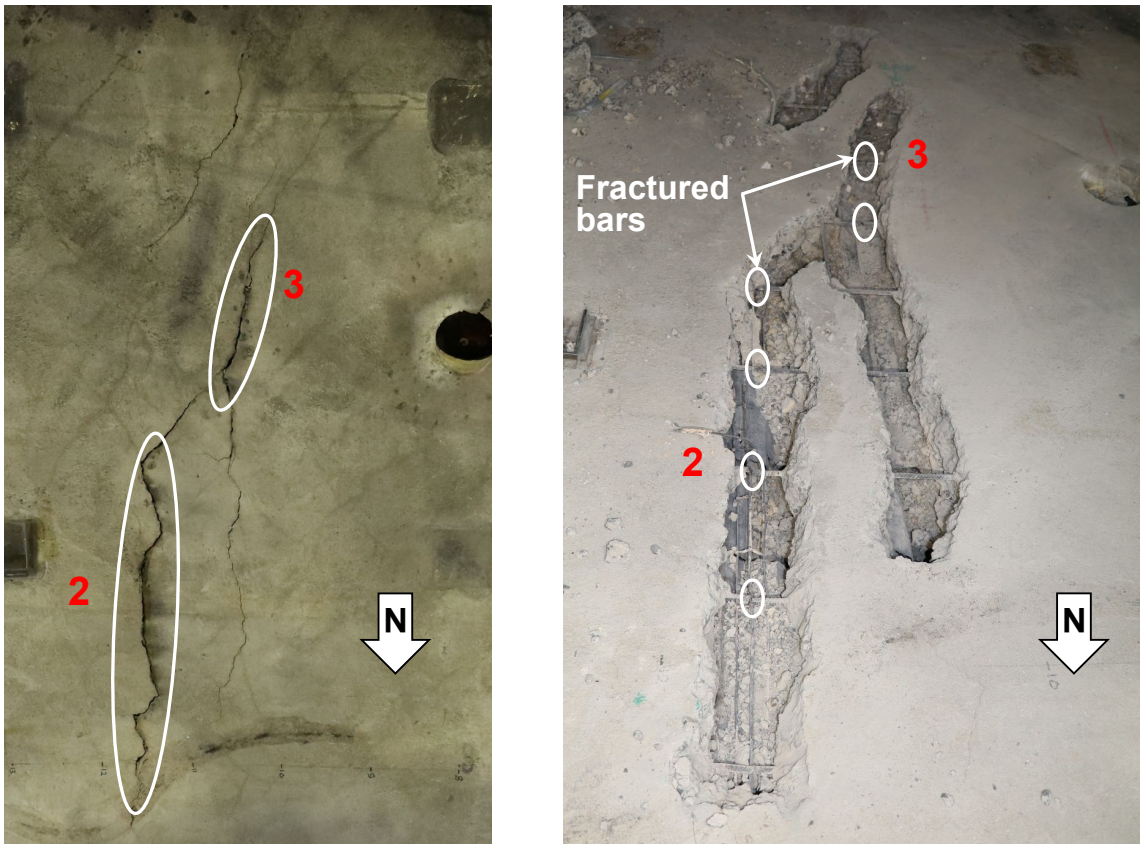

(a) (b)

Fig. 36. (a) Concrete cracks at the southeast quarter of the slab (at Locations 2 and 3 in Fig. 20); (b) rebar fractures across those cracks.

Figure 39 shows some post-test photographs of the fire damaged steel deck under the concrete slab. As shown, the test fire caused extensive damages to the steel decking across the entire test bay, including steel deck rupture at many locations throughout tested slab. In the west half of the secondary beam, the steel deck together with shear studs and concrete separated from the beam during the test as shown in Fig. 39a and Fig. 39b. Figure 40a through Figure 40e show the damaged shear studs along the secondary beam. Most of the shear studs in the west half of the secondary beam as well as in the east end of the secondary beam exhibited stud fracture or large bending, indicating the loss of composite action between the steel beam and concrete. This was because of the higher temperatures of the unprotected secondary beam and shear studs. Large bending of the shear studs indicates significant shear transfer between the concrete and steel beam as the unprotected steel beams were heated rapidly. No concrete failure around the shear studs was observed (Fig. 40a).

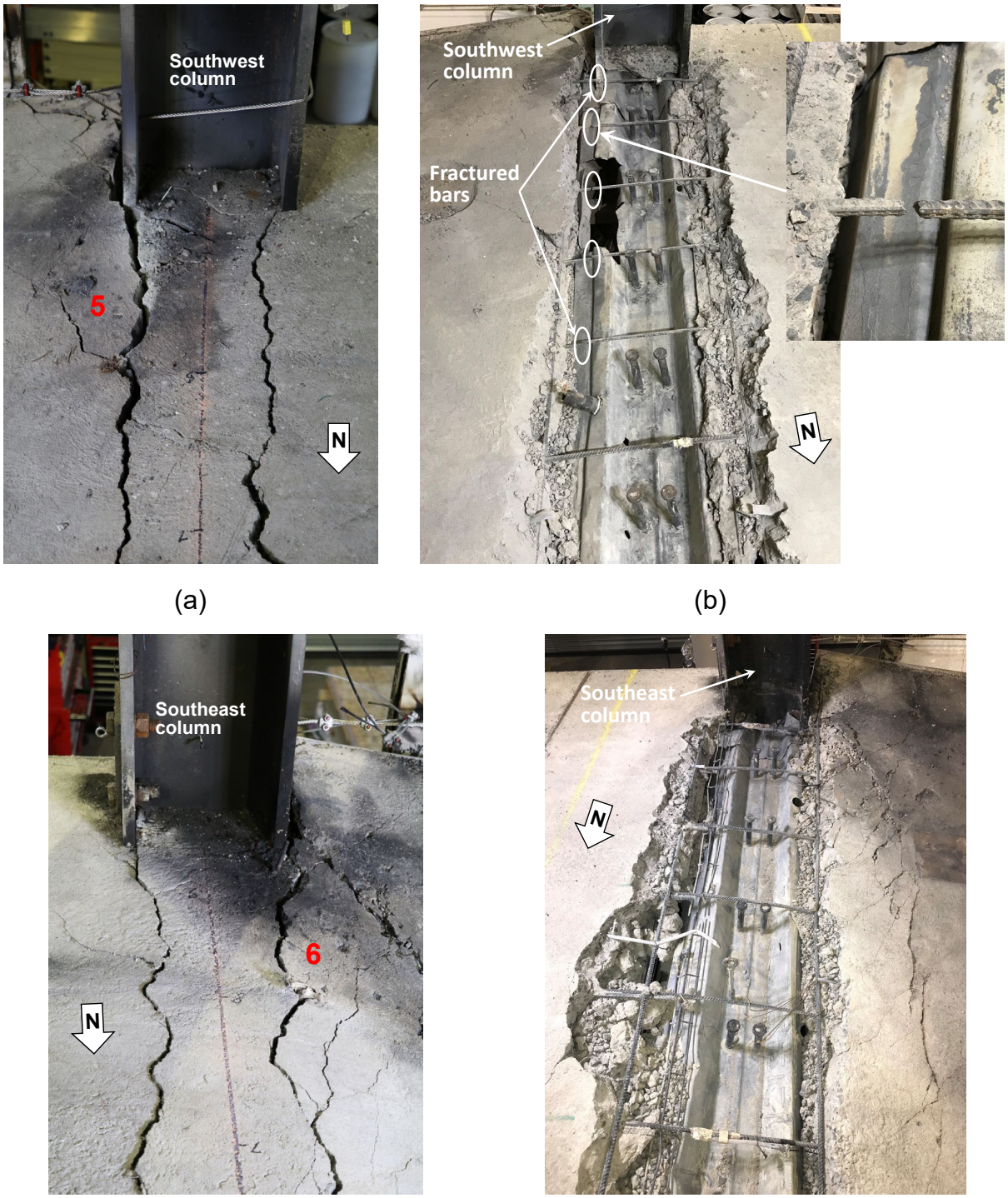

Fig. 37. (a) Concrete cracks along the west perimeter of the test bay; (b) reinforcing bar fractures along the west perimeter; (c) concrete cracks along the east perimeter of the test bay; (d) exposed reinforcing bars along the east perimeter (at Locations 5 and 6 in Fig. 20).

(a)

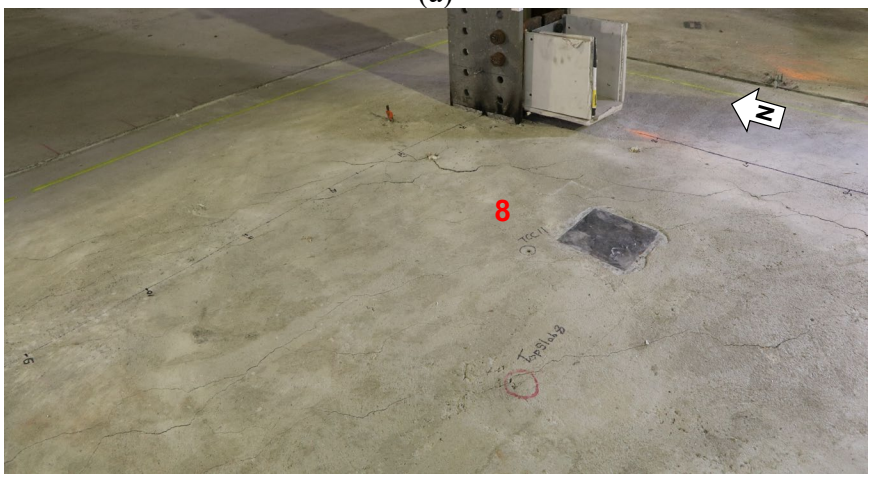

(b)

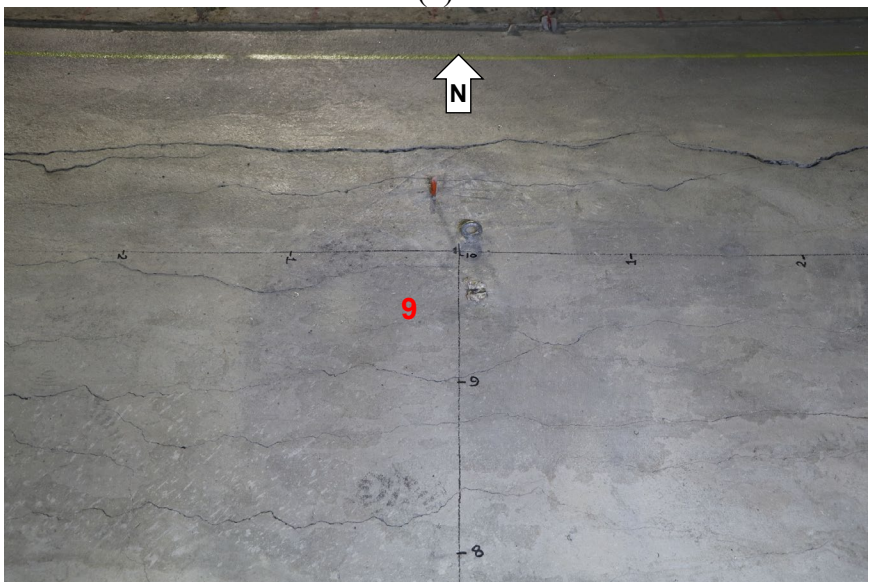

(c)

Fig. 38. Post-test photographs of the test floor slab at Locations 7, 8, and 9 in Fig. 20.

(a)

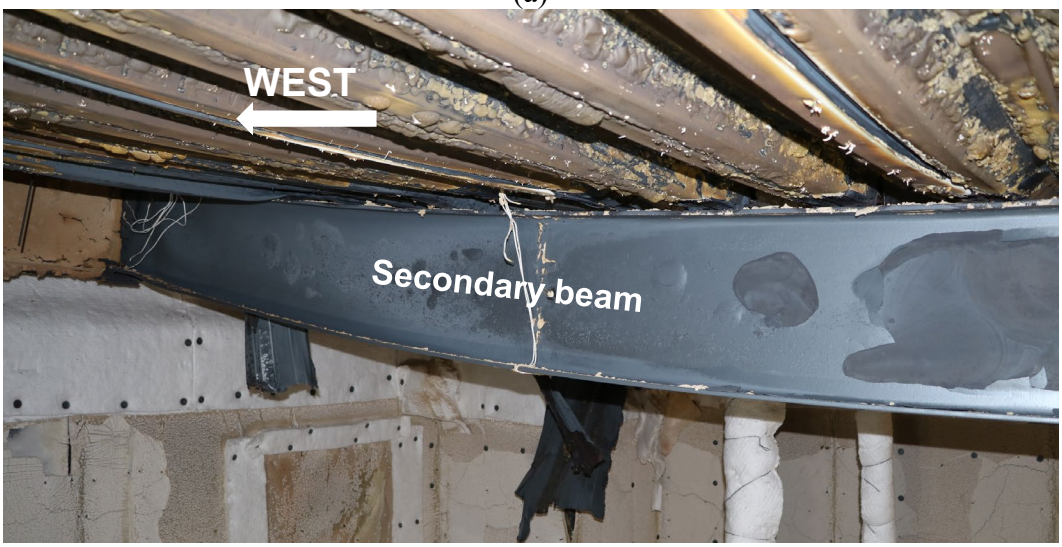

(b)

(c)

Fig. 39. (a) Steel deck rupture and separation from the beam in west half of test floor; (b) steel deck fracture in west half of test floor; (b) steel deck fracture in east half of test floor.

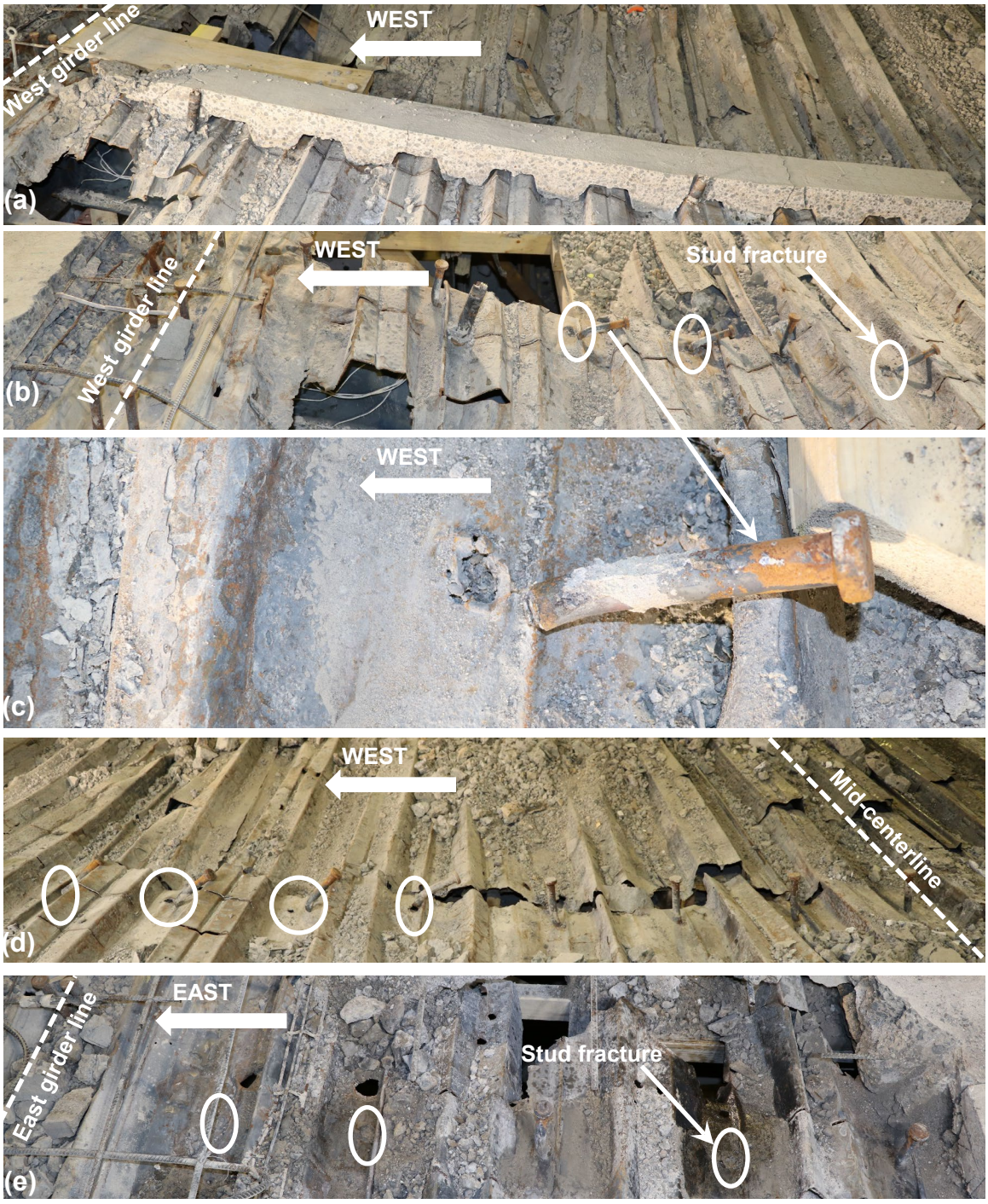

Fig. 40. Shear stud fracture along secondary beam (a) before removal of concrete around the shear studs at west end; (b) after removal of concrete at west end; (c) enlarged view of fracture of third shear stud from west end; (d) after removal of concrete at mid-span; (e) after removal of concrete at east end.

3.5.2. Beams and Connections

Figure 41 through Figure 43 show the post-test photographs of the fire damaged steel beams and connections. As shown, all floor beams, suffered from the test fire, exhibited permanent global deflection as well as both flange and web local buckling, although the severity of steel deformations varied among beams (Fig. 41). The north and south primary beams exhibited some degree of lateral deformation and twisting, whereas the secondary beam was mostly bent in its strong axis.

The local buckling at the ends of the 9.1 m long secondary beam appeared to be minor compared to the local buckling at the ends of the 9.1 m long north and south primary beams (Fig. 42 and Fig. 43). Instead, the W14×22 secondary beam framing to the east and west surrounding bay locally buckled near its connection to the girders in the test bay (Fig. 42c and Fig. 42d). It is also noteworthy that the applied SFRM coating turned black at many locations on the steel beams (Fig. 42a through and Fig. 42c). This result was possibly involved with high temperature oxidation of steel at 900 °C or higher.

As shown in Fig. 42a, all three bolts in the unprotected shear tab connection between the unprotected secondary beam and girder fractured during heating. The east end shear connection did not exhibit any structural failure (Fig. 42b). The west shear tab connection of the north primary beam exhibited bolt fracture during the cooling phase (Fig. 43d and Fig. 43e). Refer to Appendix A11 for more post-test photographs of the tested composite slab.

Fig. 41. Post-test photographs of the test bay beams after steel deck removal.

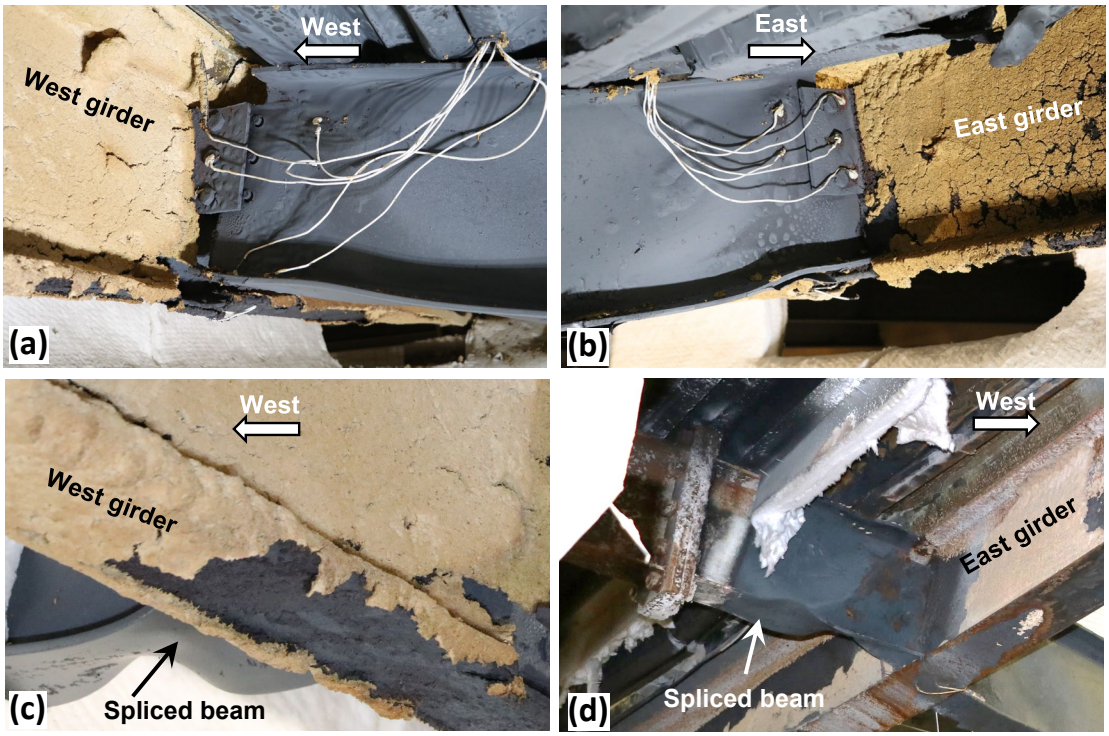

Fig. 42. Post-test photographs of the beam ends and connections (a) west end of unprotected secondary beam of test bay; (b) east end of secondary beam; (c) spliced beam in the surrounding bay west of secondary beam; (d) spliced beam in the surrounding bay east of secondary beam.

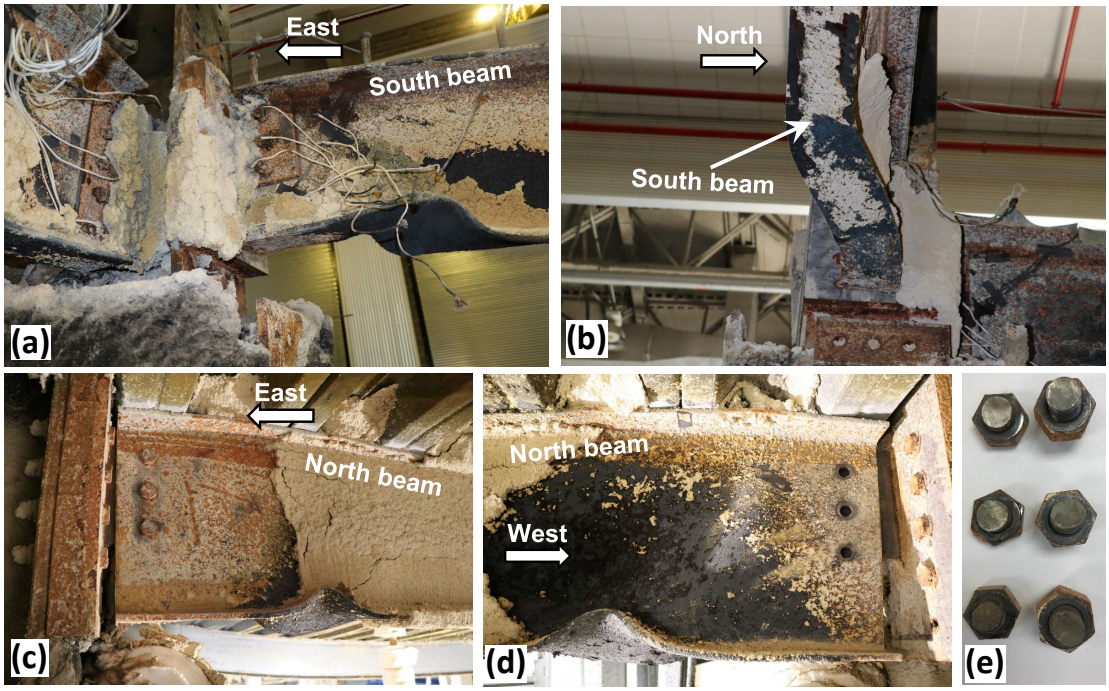

Fig. 43. Post-test photographs of the beam ends and connections (a) east end of south beam of test bay; (b west end of south beam; (c) east end of north beam; (d) west end of north beam; (e) fractured bolts at the west end of north beam.

4. Summary and Conclusions

The third fire experiment (Test #3) was conducted on the 9.1 m × 6.1 m composite floor to investigate the influence of the fire protection scheme of the secondary beam on the fire resilience of the full-scale composite floor subjected to combined mechanical and fire loading. This report has described details of the experimental design and construction, the fire test conditions, and the experimental results. In this test (Test #3), the secondary beam and its end connections were left unprotected. Furthermore, the same slab reinforcement scheme used in Test #2 was used in this test. The test floor assembly consisted of No. 3 deformed bars with the spacing of 30.5 cm, resulting in the equivalent area of 230 mm^2/m slab width. ACI-318 [22] specified contact splices were used to splice the No. 3 bars, instead of mechanical couplers used in Test #2. All other conditions remained identical or comparable to those used in the first two experiments (Test #1 and Test #2) of this test program, including the specimen geometry, beam-end connections, test fire curves, imposed gravity loads, and passive fire protection of the remaining beams and connections.

While sustaining a mechanical load of 125 kN, the test floor assembly was heated by the natural gas fueled compartment fire with the peak heat release rate approximately equal to 12 MW. The unloading of actuators started at 140 min of fire exposure and the natural gas burners were switched off at 142 min.

Some key observations and conclusions drawn from Test #3 are summarized as follows:

1) The average upper layer gas temperature within the test bay was approximately 10 % higher than that specified in ASTM E119 standard. It closely followed the temperature time curve of Test #2 and approximately 5 % higher than the temperature measured in Test #1. The peak average upper layer gas temperature was recorded at 1120 °C. The standard deviation in temperature measurements (from twelve thermocouples) was less than 50 °C, indicating practically uniform heating conditions beneath the test floor assembly.

2) The unprotected secondary beam (W16×31) was heated to 1070 °C on average at the bottom flange until the test fire was extinguished. The bottom flanges of the SFRM protected north and south beams (W16×31) were heated to 940 °C on average. The average temperature of the top surface of the concrete slab remained below the ASTM E119 limit of 157 °C, i.e., 139 °C above the ambient temperature (18 °C) measured prior to the ignition of the test fire, during heating. The average top surface temperature exceeded 157 °C at 154 min, 12 mins into cooling. A larger temperature variation existed among the embedded No. 3 reinforcing bars. The slab reinforcement at the deep and shallow sections of the slab in Test #3 reached 320 °C and 600 °C at 142 min, when the burners were shut off.

3) The mid-panel vertical displacement reached 535 mm (equivalent to the ratio of L/17 where the span length L = 9.1 m) at 132 min, when the transverse crack (integrity failure) developed in the mid-panel region. The peak displacement was 655 mm (L/14) at 140 min, when the actuator loading was removed. The floor specimen met the ASTM E119 displacement criteria for the 2 hour rating period.

4) Compared to Test #1, the No. 3 bars placed in the test floor slab in Test #3 appeared to effectively control the formation of large concrete cracks along the perimeter of the test bay. Most of the concrete cracks along the perimeter, except near the south columns, were less than 10 mm wide after cooldown. The concrete crack along the west perimeter near the south

column exhibited rebar fractures. The floor specimen exhibited a wide transverse crack at 132 min with flame leak above the floor through this crack. The test floor exhibited cracks in the south east quarter of the test panel at 138 min with rebar fractures and flame leak through these cracks.

5) The test fire in Test #3 caused extensive damage (ruptures) to the exposed steel deck compared to Test #1. All fire-exposed beams exhibited some degree of permanent global deflection and local buckling. The steel deck together with shear studs and concrete separated from the beam in the west half of the secondary beam. Most of the shear studs in the west half of the secondary beam as well as in the east end of the secondary beam exhibited stud fracture or large bending, indicating the loss of composite action between the steel beam and concrete as well as the load transfer by the tension membrane action of the slab. All three bolts in the unprotected shear tab connection at the west end of the secondary beam fractured during heating. The west end shear connection of the north primary beam exhibited fracture of all three bolts during the cooling phase.

This third test suggests that the use of No. 3 deformed steel bars (230 mm^2/m) for the slab reinforcement determined by incorporating tensile membrane action maintained the structural integrity of the tested slab during the specified 2 hour rating period without SFRM protection of the secondary beam and its beam-end connections. The structural integrity of the heated floor slab was maintained due to tensile membrane action activated after loss of flexural capacity of the secondary beam. Even though the failure of the shear connections did not lead to collapse of the composite floor, it is necessary to further investigate the structural fire behavior of various types of connections for their engineered design when subjected to fire. The experimental results presented in this paper can be used for validation of predictive models to perform parametric studies incorporating the variability in the steel reinforcement scheme (area, spacing, and material) as well as in the passive fire protection of the steel beams for safer and cost-effective composite floor construction for fire safety. They will help to explore engineered design solutions to optimize the passive fire protection and slab reinforcement used in the steel-concrete composite floor systems for different structural and fire variables, a necessary step in the performance-based design of steel framed buildings subjected to fire.

References

[1] British Steel, “The Behaviour of multi-storey steel frame buildings in fire,” Rotherham, 1999.
[2] F. Wald *et al.*, “Experimental behaviour of a steel structure under natural fire,” *Fire Saf. J.*, vol. 41, no. 7, Oct. 2006, doi: 10.1016/j.firesaf.2006.05.006.
[3] C. Bailey, “Design of steel structures with composite slabs at the fire limit state,” Garston, Unite Kingdom, 2000.
[4] C. Bailey, “Steel structures supporting composite floor slabs: design for fire,” Garston, Unite Kingdom, 2001.
[5] C. G. Bailey, “Efficient arrangement of reinforcement for membrane behaviour of composite floor slabs in fire conditions,” *J. Constr. Steel Res.*, vol. 59, no. 7, pp. 931–949, 2003, doi: 10.1016/S0143-974X(02)00116-5.
[6] B. Zhao, M. Roosefid, and O. Vassart, “Full Scale Test of a Steel and Concrete Compoiste Floor Exposed to ISO fire,” *5th Int. Conferece Struct. Fire*, no. June, 2008.
[7] B. Zhao, M. Roosefid, and A. Breunese, “Connections of Steel and Composite Structures under Natural Fire Conditions (COSSFIRE),” Luxemburg, 2011.
[8] American National Standards Institute/Steel Deck Institute, *ANSI/SDI C-2017 Standard for Composite Steel Floor Deck-Slabs*. Steel Deck Insititute (SDI), 2017.
[9] UL (Underwriters Laboratory). Fire Resistance Ratings – ANSI/UL 263. UL, Northbrook, IL, 2011.
[10] ASTM International, “E119-21 Standard Methods of Fire Test of Building Construction and Materials.” ASTM International, West Conshohocken, PA, 2021.
[11] G. M. Newman, “The Fire Resistance of Composite Floor with Steel Decking-SCI Publication P56,” Berkshire, 1990.
[12] AISC, *Specification for Structural Steel Buildings (ANSI/AISC 360-16)*. Chicago: AISC, 2016.
[13] ASCE, *Minimum Design Loads and Associated Criteria for Buildings and Other Structures*. Reston, VA: American Society of Civil Engineers, 2017.
[14] ASCE, *ASCE MOP 138 Structural Fire Engineering*, vol. 138. Reston, VA: American Society of Civil Engineers, 2018.
[15] L. Choe *et al.*, “Fire Resilience of a Steel-Concrete Composite Floor System: Full-Scale Experimental Evaluation for U.S. Prescriptive Approach with a 2-Hour Fire-Resistance Rating (Test #1),” Gaithersburg, MD, Oct. 2021. doi: 10.6028/NIST.TN.2165.
[16] L. Choe, S. Ramesh, X. Dai, M. Hoehler, M. Bundy, 2022, Experimental study on fire resistance of a full-scale composite floor assembly in a two-story steel framed building, Journal of Structural Fire Engineering, Vol. 13 No. 2, pp. 145-161. https://doi.org/10.1108/JSFE-05-2021-0030.
[17] L. Choe, S. Ramesh, C. Zhang, C. Clifton, Behavior of composite floor assemblies subject to fire: Influence of slab reinforcement. Proceeding of 2021 Eurosteel Conference, September 1-3, 2021, University of Sheffield, United Kingdom.
[18] L. Choe, S. Ramesh, M. Hoehler, M. Bundy, R. Bryant, X. Dai, et al., Fire Resilience of a Steel-Concrete Composite Floor System: Full-Scale Experimental Evaluation for Influence of Slab Reinforcement (Test #2). NIST Technical Note (NIST TN-2203), Gaithersburg, MD, 2022. DOI: 10.6028/NIST.TN.2203.

[19] S. Ramesh, L. Choe, 2022, Structural integrity of composite floors in fire: A comparison of two large-scale experiments with varying slab reinforcement, Fire Safety Journal, Vol. 134, pp. 1-13. https://doi.org/10.1016/j.firesaf.2022.103669.
[20] C. Zhang, W. Grosshandler, A. Sauca, and L. Choe, “Design of an ASTM E119 Fire Environment in a Large Compartment,” *Fire Technol.*, vol. 56, no. 3, pp. 1155–1177, 2020, doi: 10.1007/s10694-019-00924-7.
[21] G. Clifton, A. Gillies, and N. Mago, “The Slab Panel Method: Design of Composite Floor Systems for Dependable Inelastic Response to Severe Fires,” 2010.
[22] American Concrete Institute, *Building Code Requriments for Strucutral Concrete (ACI 318-19)*. Farmington Hills, MI: American Concrete Institute, 2019.
[23] AISC (American Institute of Steel Construction). Manual of Steel Construction, 15th Edition. Chicago: AISC, 2017.
[24] ASTM International, “ASTM E8/E8-21 Standard Test Methods for Tension Testing of Metallic Materials.” ASTM International, West Conshohocken, PA, 2021, [Online]. Available: https://www.astm.org/e0008_e0008m-21.html.
[25] ICC, *2018 International Building Code*. Country Club Hills, IL: ICC, 2018.
[26] C. Maluk, L. Bisby, and G. P. Terrasi, “Effects of polypropylene fibre type and dose on the propensity for heat-induced concrete spalling,” *Eng. Struct.*, vol. 141, pp. 584–595, 2017, doi: 10.1016/j.engstruct.2017.03.058.
[27] M. Pour-Ghaz, J. Castro, E. J. Kladivko, and J. Weiss, “Characterizing Lightweight Aggregate Desorption at High Relative Humidities Using a Pressure Plate Apparatus,” *J. Mater. Civ. Eng.*, vol. 24, no. 8, pp. 961–969, Aug. 2012, doi: 10.1061/(ASCE)MT.1943-5533.0000422.
[28] ASTM International, “C192/C192M-19 Standard Practice for Making and Curing Concrete Test Specimens in the Laboratory.” ASTM International, West Conshohocken, PA, 2019.
[29] R. A. Bryant and M. F. Bundy, “The NIST 20 MW calorimetry measurement system for large-fire research,” *NIST Tech. Note 2077*, 2019.
[30] B. N. Taylor and C. E. Kuyatt, “Guidelines for Evaluating and Expressing the Uncertainty of NIST Measurement Results: Appendix D1. Terminology,” *Natl. Inst. Stand. Technol. Gaithersburg, MD*, p. D.1.1.2, 2001, [Online]. Available: http://physics.nist.gov/TN1297.
[31] OMEGA Engineering, “Super OMEGACALD XL Thermocouple Probes,” 2021. https://assets.omega.com/pdf/test-and-measurement-equipment/temperature/sensors/thermocouple-probes/TJ36CAXL_NNXL.pdf.
[32] OMEGA Engineering, “Thermocouple Wire Duplex Insulated,” 2021. https://assets.omega.com/pdf/cable-and-wire/thermocouple-and-rtd-wire-and-cable/XC_K_TC_WIRE.pdf.
[33] OMEGA Engineering, “High Temperature Wire with Nextel or Silica Yarn Fiber Insulation.” .
[34] UniMeasure, “PA Series String Potentiometers.” https://unimeasure.com/products/standard-series/.
[35] Tokyo Measuring Instruments Lab, “TML Strain Gagues.” [Online]. Available: https://tml.jp/e/product/strain_gauge.
[36] MKS, “MKS Instruments.” https://www.mksinst.com/.

Appendix A: Instrumentation, Raw Data, and Photographs

A.1. Mechanical Loading

Four servo-hydraulic actuators (each named as NW, NE, SW, and SE) were used to apply mechanical loads that were uniformly distributed at twenty-four points across the test floor slab. Those actuators were mounted at the NFRL basement below the fire test bay. Each actuator provided mechanical loading on the test floor at six points spaced 152 cm apart (Fig. 44a). The strains at the midspans of the W16×31 secondary beam and W18×35 girders in the test bay were measured using strain gauges during mechanical loading at ambient temperatures only (Fig. 44a and Fig. 44b). Measured actuator loads, actuator displacements, and the beam strain values are provided in Fig. 45 and Fig. 46.

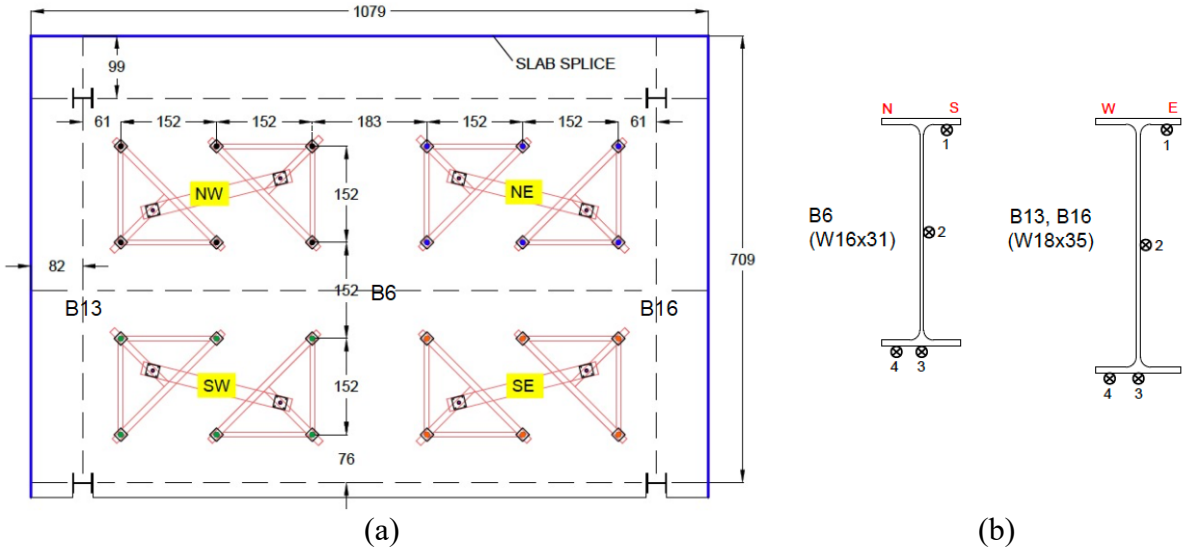

Fig. 44. Locations of (a) loading points tied to four hydraulic actuators (NE, NW, SE, SW) and (b) strain gauges installed at midspan of the test bay floor beams. Dimensions are in cm.

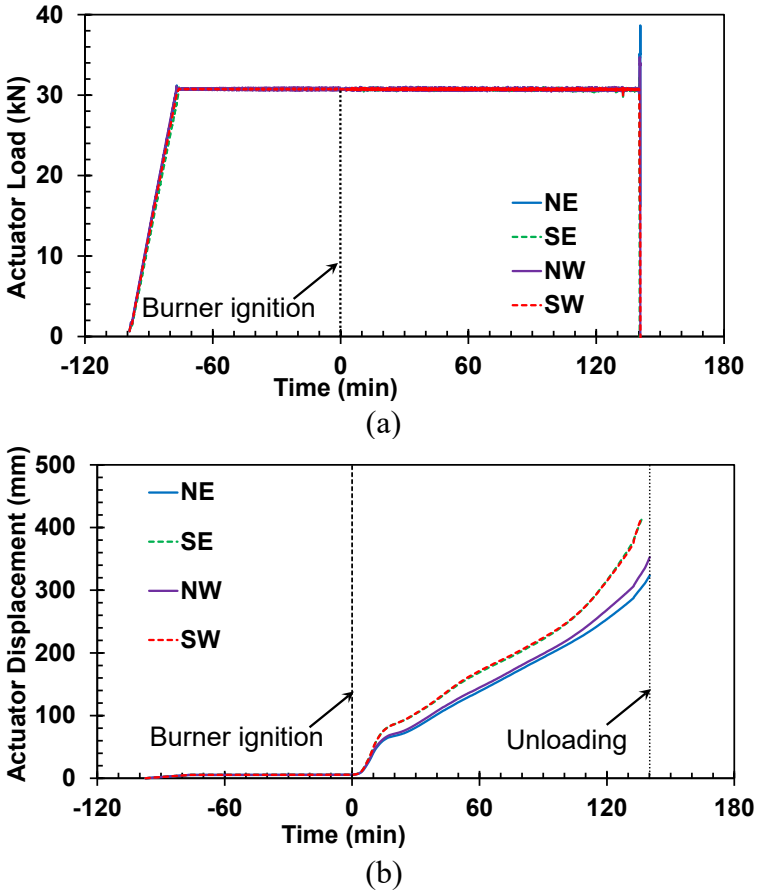

Fig. 45. Actuator data: (a) mechanical force and (b) stroke displacement of four hydraulic actuators (NE, SE, NW, and SW) used in the test.

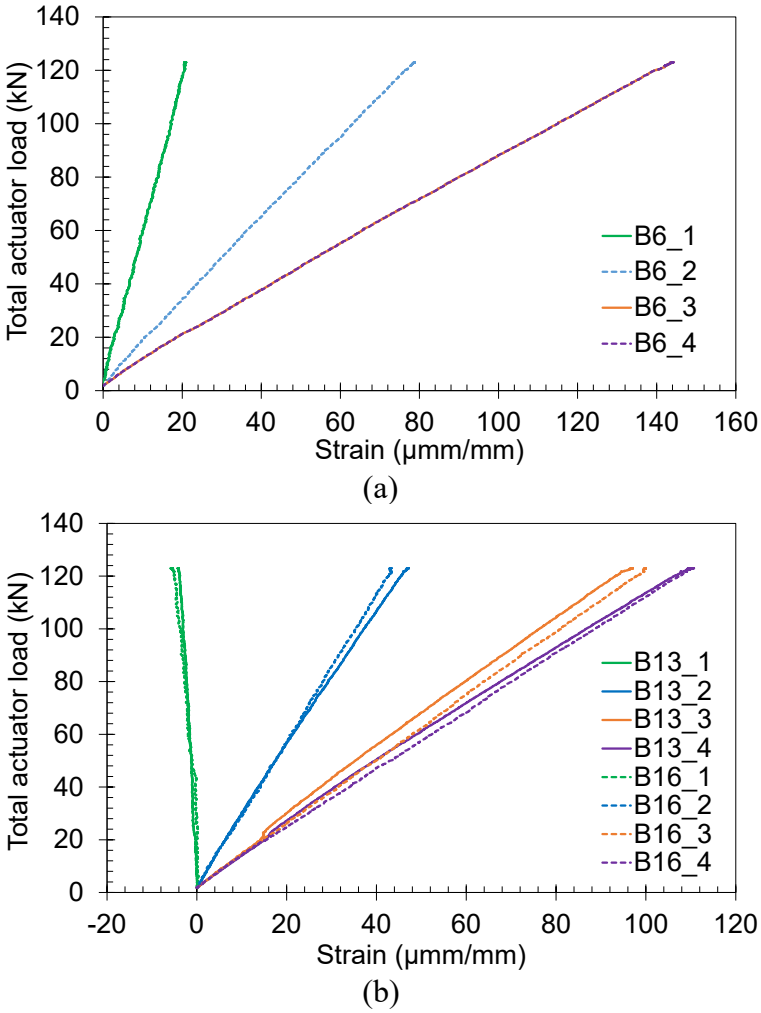

Fig. 46. Beam strains during the ambient temperature mechanical loading: (a) secondary beam and (b) girders at midspan in the test bay.

A.2. Gas Temperature

OMEGACLAD sheathed thermocouples (model: TJ36-CAXL-14U-24) [31] were used to measure the gas temperatures inside the test compartment. Twelve thermocouple probes (TCC1 through TCC12) were mounted 30.5 cm (z = 346 cm) below the floor specimen soffit (i.e., the compartment ceiling) for gas temperature measurements (Fig. 47). Two thermocouple trees were placed inside the test compartment, including the north tree 79 cm from the north wall (NorthTC) and the south tree 96 cm from the south wall (SouthTC). Thermocouple probes were located approximately 10 cm away from the exposed surface of Kaowool blanket wrapping the mounting stand. Photographs of some installed thermocouple probes are shown in Fig. 48.

The hottest spot was measured at TCC5 which was approximately 50 °C above the average upper layer gas temperature. TCC11 indicated the lowest temperature, about 50 °C below the average value. During cooling, temperatures of TCC6 decreased much quicker than TCC11.

In addition, during the first 15 min of heating, the gas temperatures measured at the north and south trees differed by a maximum of 100 °C, due to air intake through the south ventilation opening. However, this temperature variability also became smaller as the test fire continued longer than an hour.

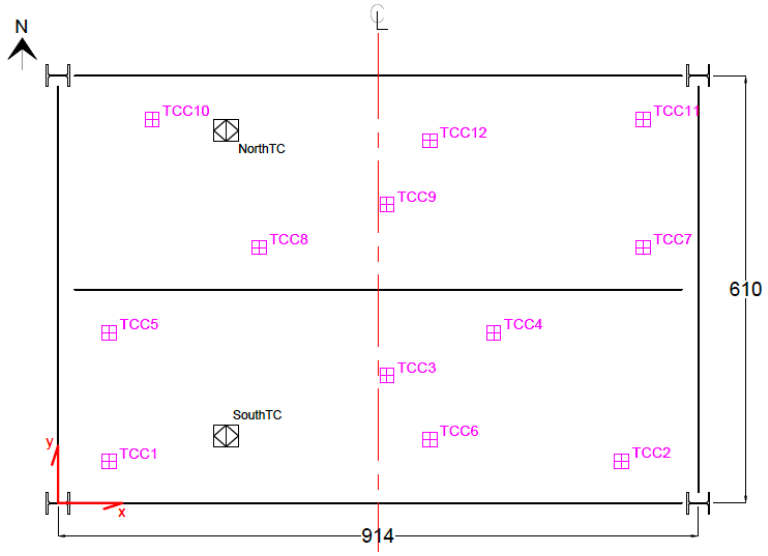

Name/ID	X East+	Y North+	Z Up+
TCC1	73	60	346
TCC2	805	60	346
TCC3	470	182	346
TCC4	622	242	346
TCC5	73	244	346
TCC6	531	90	346
TCC7	835	364	346
TCC8	287	364	346
TCC9	470	425	346
TCC10	134	547	346
TCC11	835	547	346
TCC12	531	517	346
NorthTC1	240	531	302
NorthTC2	240	531	201
NorthTC3	240	531	102
SouthTC1	240	96	302
SouthTC2	240	96	201
SouthTC3	240	96	102

Fig. 47. Locations of thermocouple probes used for gas temperature measurements within the fire test bay. The Z datum of NorthTC and SouthTC probes is at top surface of the compartment floor. Dimensions and coordinates are in cm.

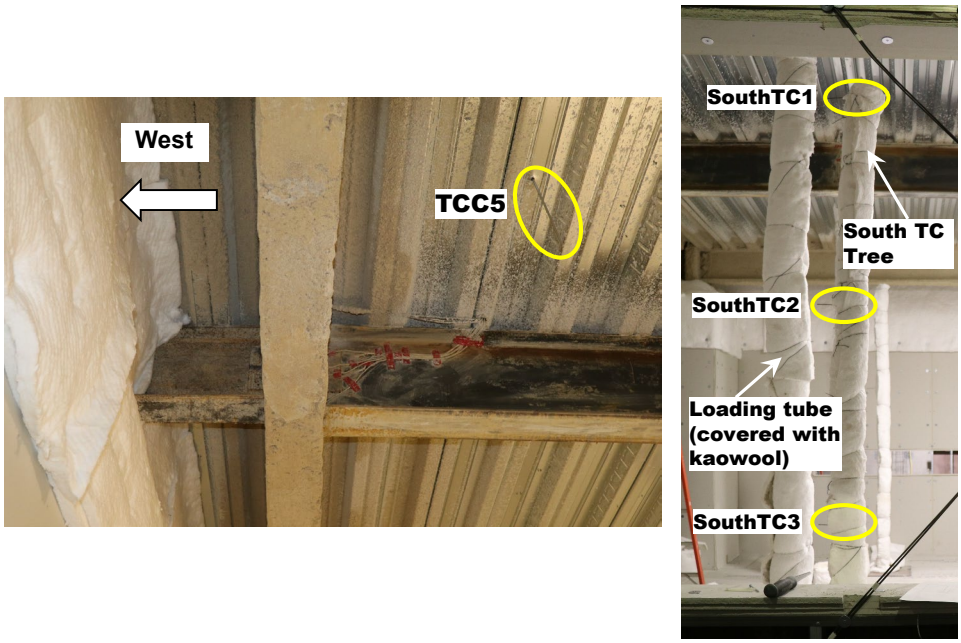

Fig. 48. Photographs of installed TCC1 and SouthTC probes.

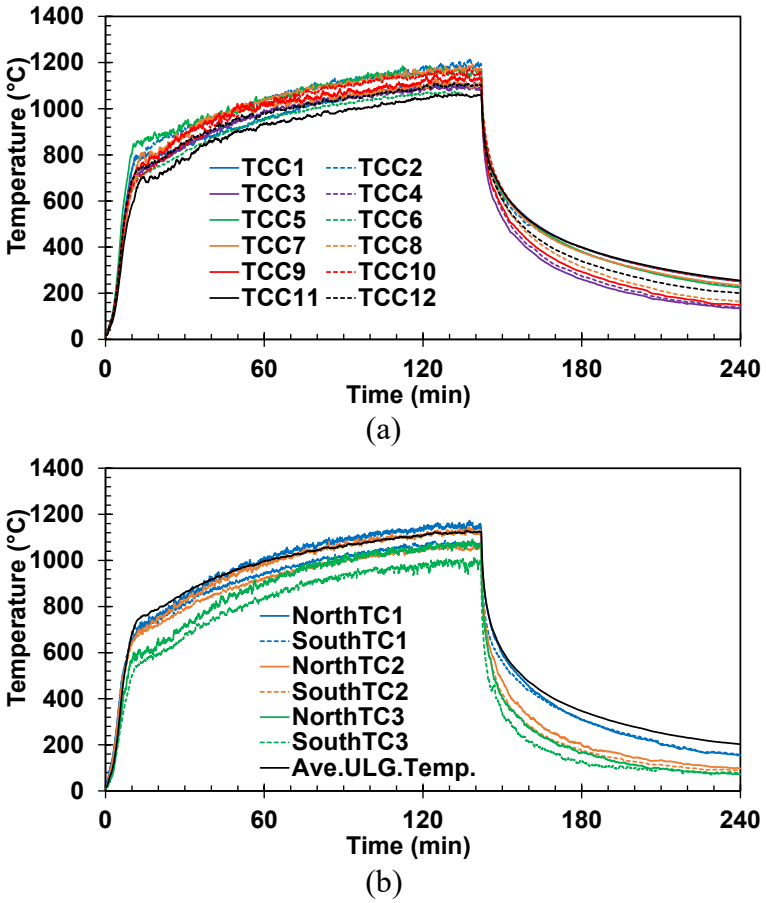

Fig. 49. Gas temperatures inside the test compartment. Fire was extinguished at 142 min.

A.3. Concrete Temperature

Glass sheathed thermocouples (model: GG-K-24) [32] were used to measure concrete temperatures. A total of ten thermocouple trees, made of the 10 cm diameter concrete cylinders, were placed in the test floor slab. Locations of these cylinders (TST1 through TST8) are shown in Fig. 50. In each cylinder, two to four thermocouples were secured through the thickness of the slab, except for TSTi_5* which was mounted 3 mm above the deck pan. Table 12 shows the list of thermocouple probes used to estimate the average temperatures at specific depths which are plotted in Fig. 20. All raw data are plotted in Fig. 51.

Table 12. List of thermocouples used to estimate the average temperatures plotted in Fig. 20.

Plot legend	Channel ID	Maximum standard deviation, °C
1	TST1_1, TST3_1, TST7_1, TST8_1, TST2_1, TST6_1	120
2	TST1_2, TST3_2, TST7_2, TST8_2, TST2_2, TST6_2	110
3	TST1_3, TST3_3, TST7_3, TST8_3, TST2_3, TST6_3	100
4	TST1_4, TST3_4, TST7_4, TST8_4, TST2_4, TST6_4	180
5	TST4_5, TST5_5	140
6	TST4_6, TST5_6, TST2_6, TST6_6	250
7	TST4_7, TST5_7, TST2_7, TST6_7	290
5*	TST2_5, TST6_5	40

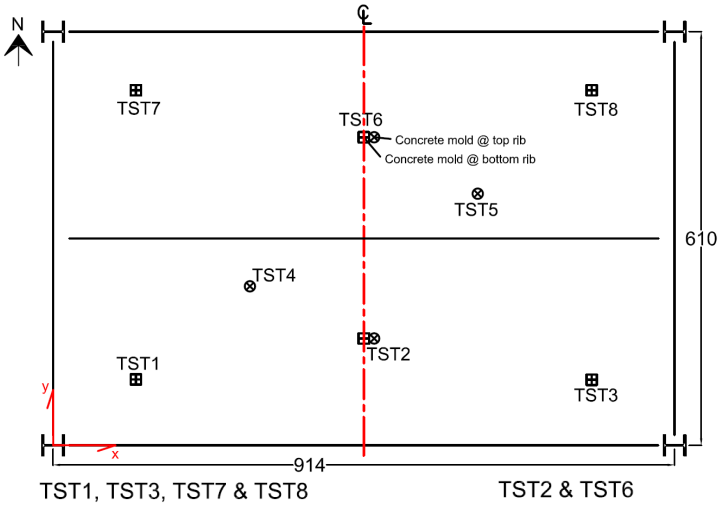

Section	Name/ID	X East+	Y North+
Bottom rib	TST1	122	97
Bottom rib	TST2	457	157
Top rib	TST2	472	157
Bottom rib	TST3	488	97
Bottom rib	TST4	290	234
Bottom rib	TST5	625	377
Bottom rib	TST6	457	454
Top rib	TST6	472	454
Bottom rib	TST7	122	523
Bottom rib	TST8	792	523

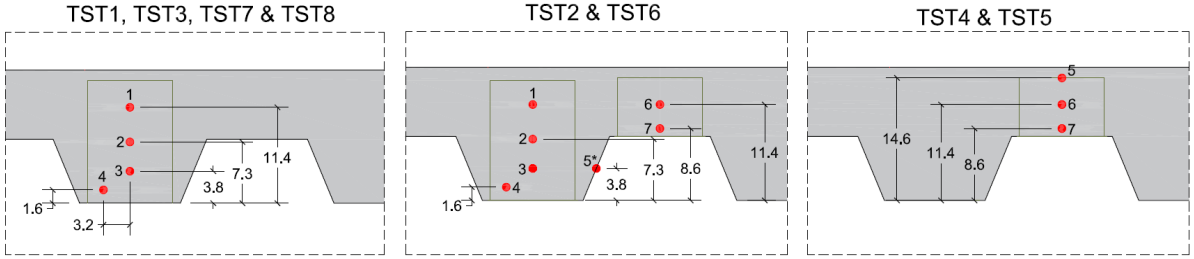

Fig. 50. Locations of thermocouples within the test floor slab. Dimensions and coordinates are in cm.

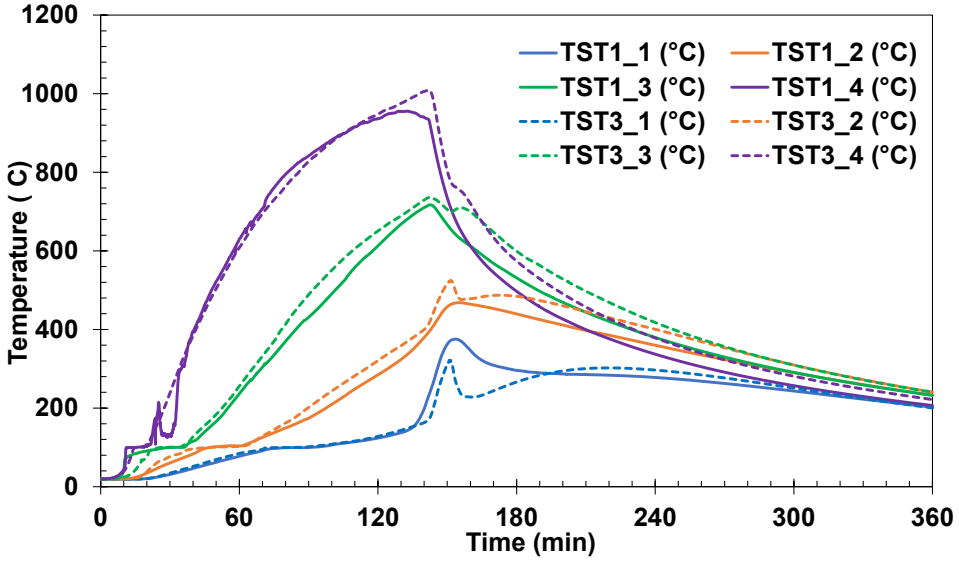
TST1_1 (°C)
TST1_2 (°C)
TST1_3 (°C)
TST1_4 (°C)
TST3_1 (°C)
TST3_2 (°C)
TST3_3 (°C)
TST3_4 (°C)
Temperature (C)
Time (min)
0
200
400
600
800
1000
1200
0
60
120
180
240
300
360

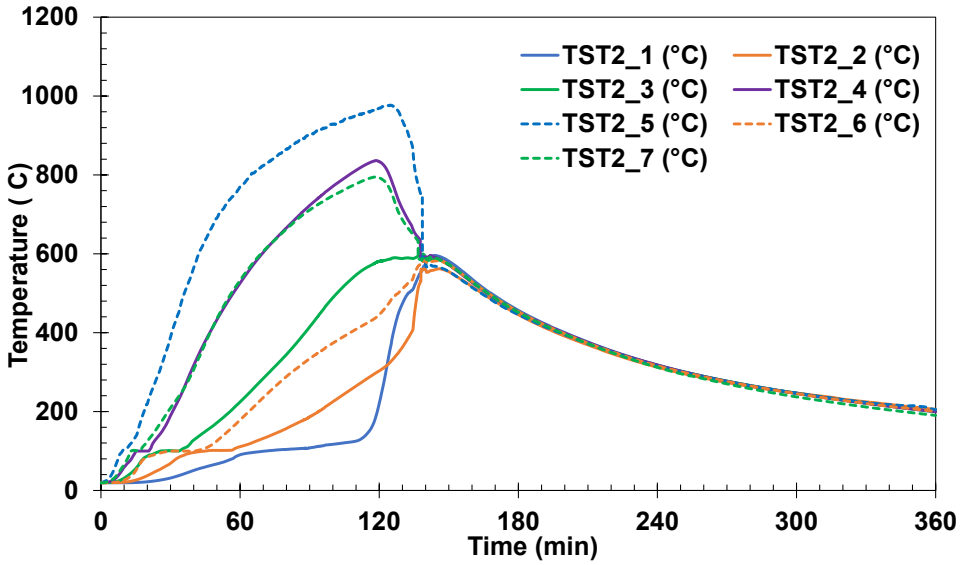
TST2_1 (°C)
TST2_2 (°C)
TST2_3 (°C)
TST2_4 (°C)
TST2_5 (°C)
TST2_6 (°C)
TST2_7 (°C)
Temperature (C)
Time (min)
0
200
400
600
800
1000
1200
0
60
120
180
240
300
360

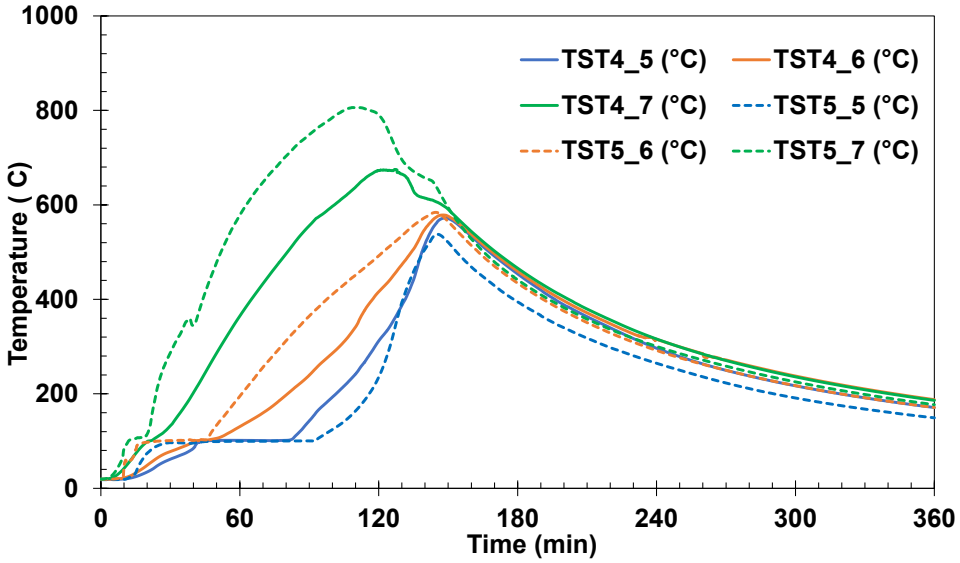
TST4_5 (°C)
TST4_6 (°C)
TST4_7 (°C)
TST5_5 (°C)
TST5_6 (°C)
TST5_7 (°C)
Temperature (C)
Time (min)
0
200
400
600
800
1000
0
60
120
180
240
300
360

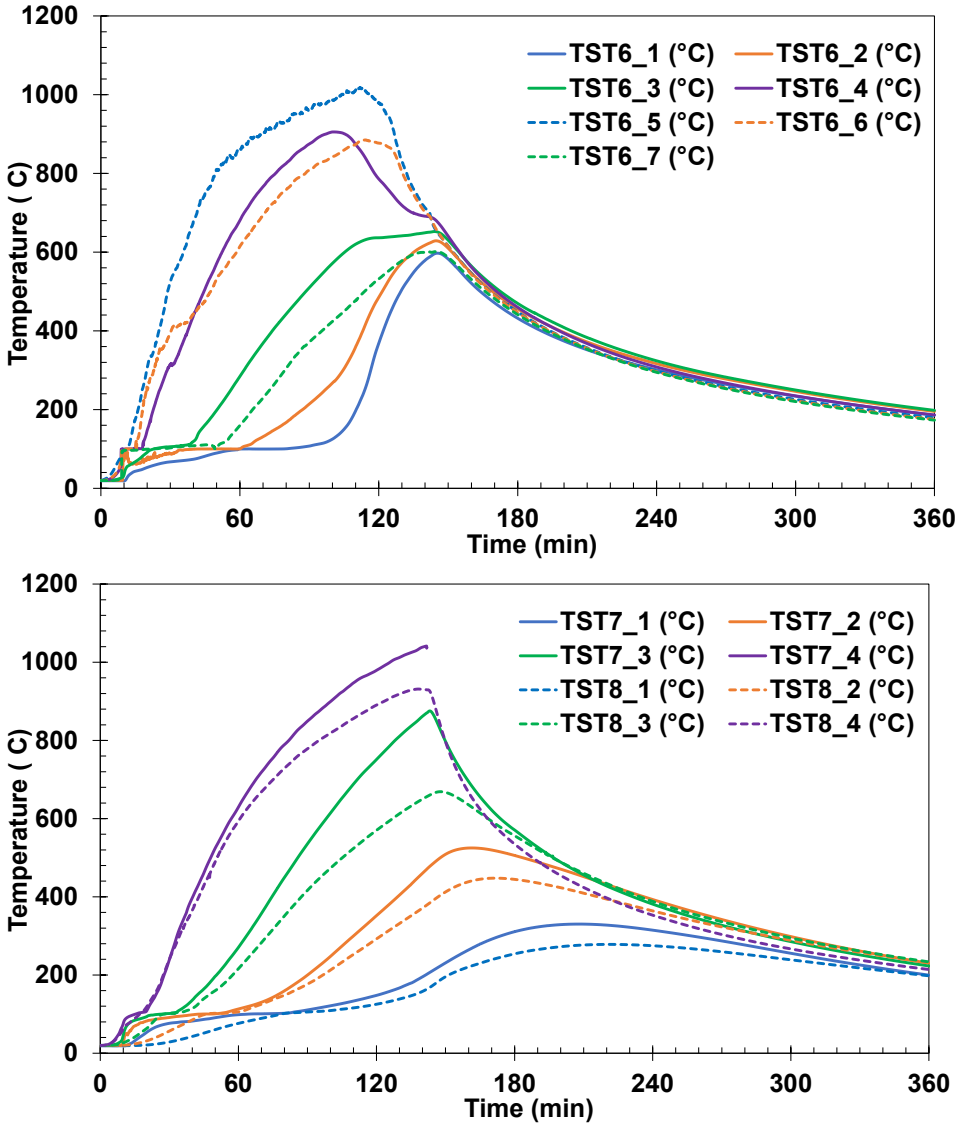

Fig. 51. Concrete temperatures through the depth of the test floor slab.

A total of twelve thermocouples (labeled with TopSlab1 through TopSlab12) were mounted 3 mm below the top (unexposed) surface of the test bay slab. Locations of these thermocouples and raw temperature data are provided in Fig. 52 and Fig. 53, respectively. As shown, temperatures continued to rise during the cooling phase of the test fire (up to 110 min into cooling). The peak temperatures were in a large range of 160 °C to 230 °C because of the use of the profiled steel decking. Table 13 shows the list of thermocouple probes used to estimate the average temperatures at specific depths which are plotted in Fig. 21.

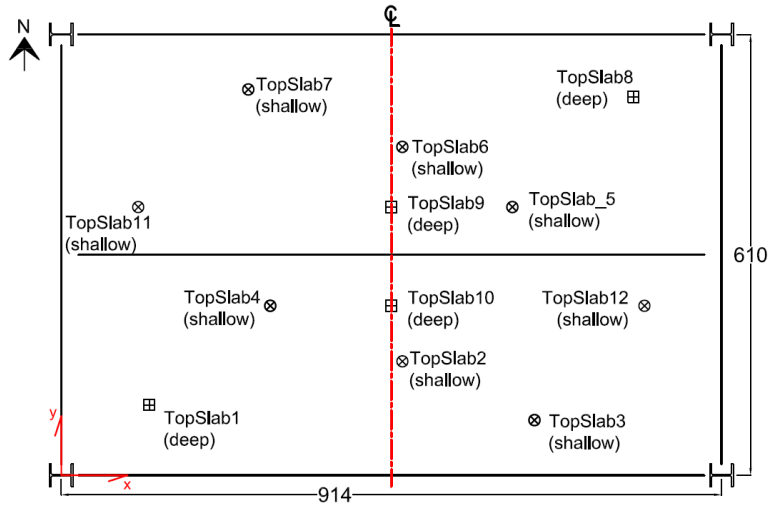

Section	Name/ID	X East+ (cm)	North+ (cm)
Deep	TopSlab1	122	97
Shallow	TopSlab2	472	157
Shallow	TopSlab3	655	76
Shallow	TopSlab4	290	234
Shallow	TopSlab5	625	371
Shallow	TopSlab6	472	454
Shallow	TopSlab7	259	533
Deep	TopSlab8	792	523
Deep	TopSlab9	457	371
Deep	TopSlab10	457	234
Shallow	TopSlab11	107	371
Shallow	TopSlab12	808	234

Fig. 52. Locations of thermocouple probes used for temperature measurements of top (unexposed) surface of the test floor slab. Dimensions are in cm.

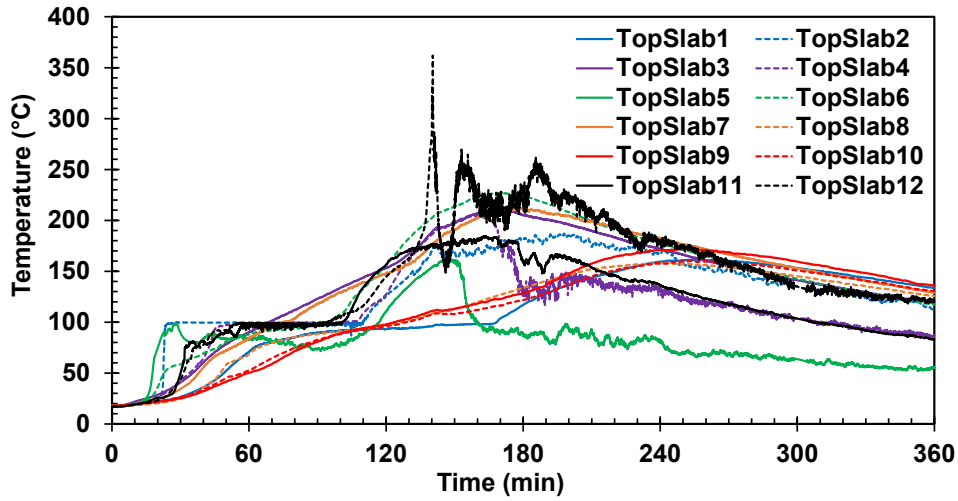

Fig. 53. Top surface temperatures of the test floor slab. Fire was extinguished at 142 min.

Table 13. List of thermocouples used to estimate the average temperatures plotted in Fig. 21a.

Plot legend	Channel ID	Maximum standard deviation, °C
Shallow	TopSlab2, TopSlab3, TopSlab4, TopSlab5, TopSlab6, TopSlab7, TopSlab11	10
Deep	TopSlab1, TopSlab8, TopSlab9, TopSlab10	20

A.4. Reinforcing Bar Temperature

Glass sheathed thermocouples (model: GG-K-24) [32] were used to measure temperatures of embedded No. 3 bars in the test-bay floor slab. Locations of thermocouples and raw data are presented in Fig. 54 and Fig. 55, respectively. Temperatures of the No. 3 bars above the steel beams and girders at midspan are also measured using the S group thermocouples as described in Sect. A.5.

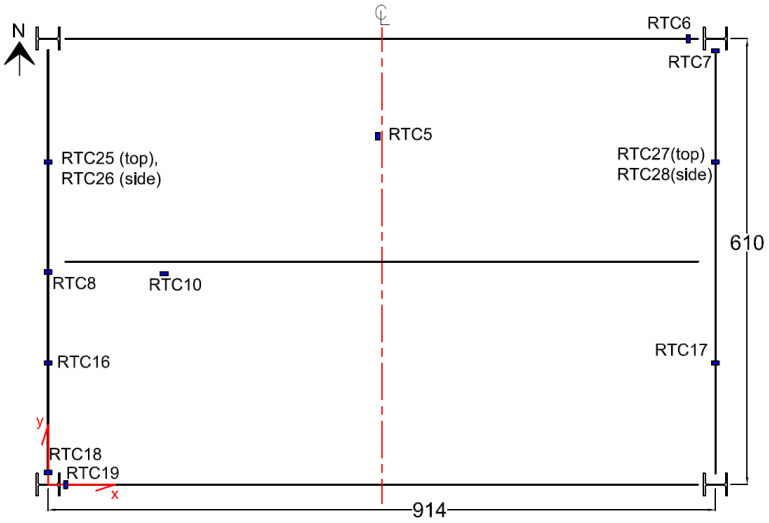

Name/ID	X East+	Y North+	Z Up+	Bar Orientation	Concrete Section
RTC5	452	476	11.6	Transverse	Deep
RTC6	877	610	11.6	Transverse	Deep
RTC7	914	593	10.6	Longituidnal	Deep
RTC8	0	291	10.6	Longituidnal	Deep
RTC10	159	288	10.6	Longituidnal	Deep
RTC16	0	167	10.6	Longituidnal	Deep
RTC17	914	167	10.6	Longituidnal	Deep
RTC18	0	17	10.6	Longituidnal	Deep
RTC19	24	0	11.6	Transverse	Deep
RTC25	0	441	11.1	Longituidnal	Deep
RTC26	0	441	10.6	Longituidnal	Deep
RTC27	914	441	11.1	Longituidnal	Deep
RTC28	914	441	10.6	Longituidnal	Deep

Fig. 54. Distribution of thermocouple probes mounted on No. 3 deformed bars. Dimensions and coordinates are in cm.

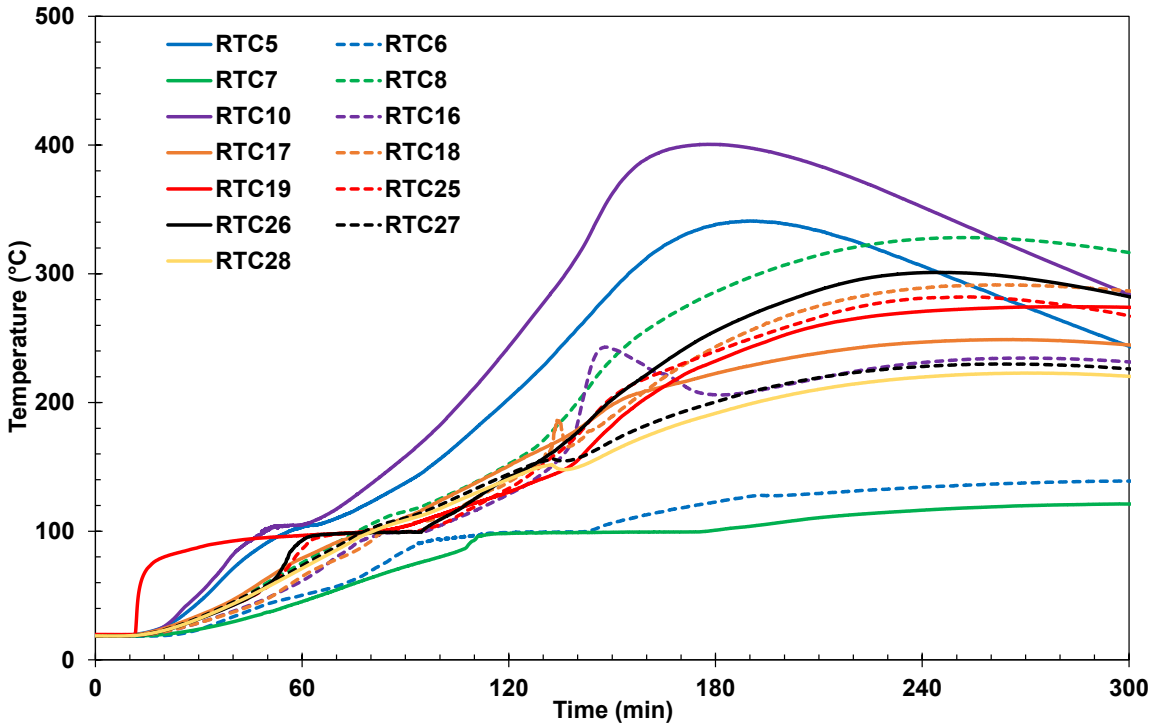

Fig. 55. Temperatures of No. 3 deformed bars placed inside the test floor slab.

Table 14 shows the list of thermocouple probes used to estimate the average temperatures of bars at specific depths which are plotted in Fig. 21b. For this estimation, thermocouples mounted on the bars not directly placed above the steel beams and girders as well as some TST group thermocouples mounted at a similar depth within the test slab (Refer to Sect. A.3) were used. Raw data used to estimate the average temperatures of bars at deep and shallow sections of the slab are presented in Fig. 56a and Fig. 56b, respectively.

Table 14. List of thermocouples used to estimate the average bar temperatures plotted in Fig. 21b

Plot legend	Channel ID	Maximum standard deviation, °C
Deep Section	TST1_1, TST2_1, TST3_1, TST6_1, TST7_1, TST8_1, RTC5	180
Shallow Section	TST2_6, TST4_6, TST5_6, TST6_6	250

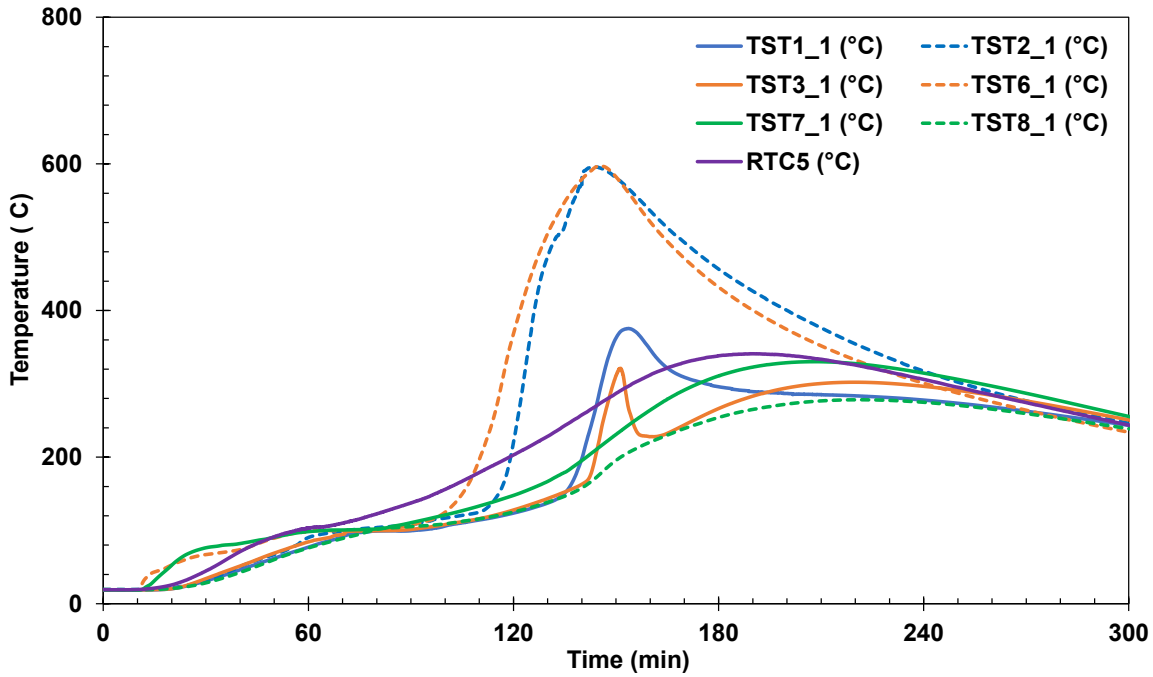

(a)

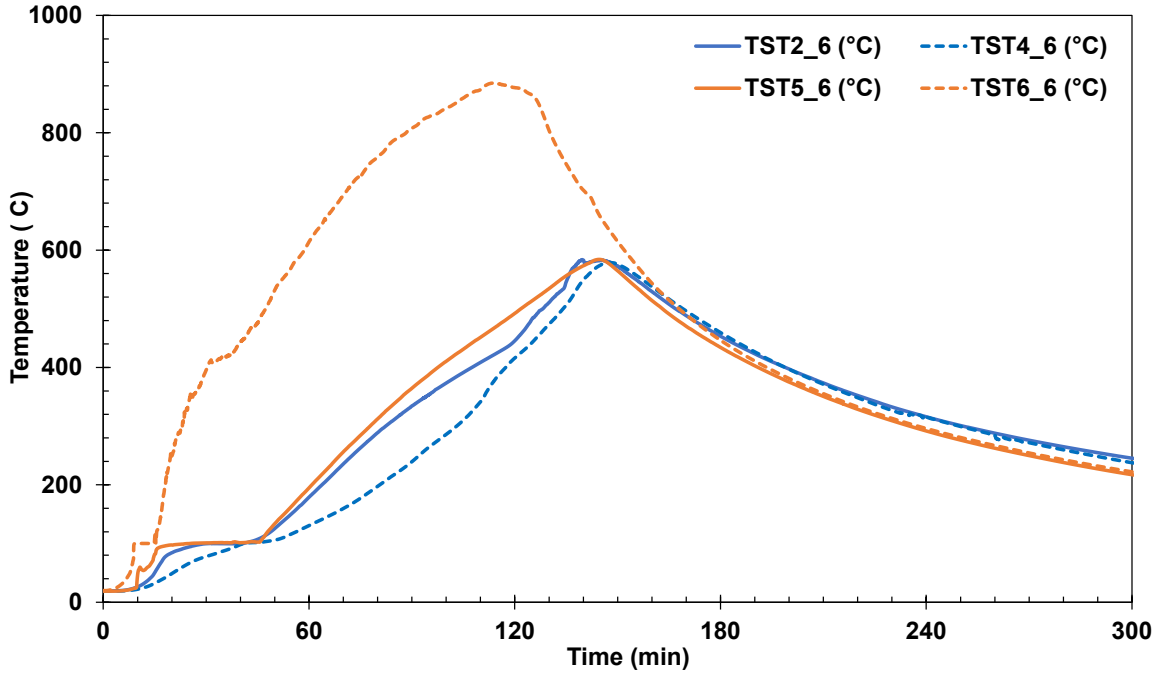

(b)

Fig. 56. No. 3 deformed bar temperatures (a) at deep sections and (b) at shallow sections of the slab.

A.5. Composite Section Temperature

For the composite beam sections, temperature measurements were performed using K-type thermocouples with two different wire insulation techniques: glass sheathed thermocouples (model: GG-K-24) mounted within the concrete slab and the ceramic sheathed thermocouples (model: XT-K-20-SLE) [33] directly peened on the surface of the steel beam shapes. An example of thermocouples installed prior to the slab cast and fireproofing spray is shown in Fig. 57. Locations of thermocouples and raw data are provided in Fig. 58 through Fig. 61. The temperature readings of the secondary beam at midspan (TB6 group at section 6) became unreliable due to failure of the thermocouple probes after about 70 min into heating. Table 15 shows the list of thermocouple probes used to estimate the average temperatures at specific depths across the composite beam section, which are plotted in Fig. 23.

Fig. 57. Photographs of typical thermocouples installed in the composite girder near its midspan.

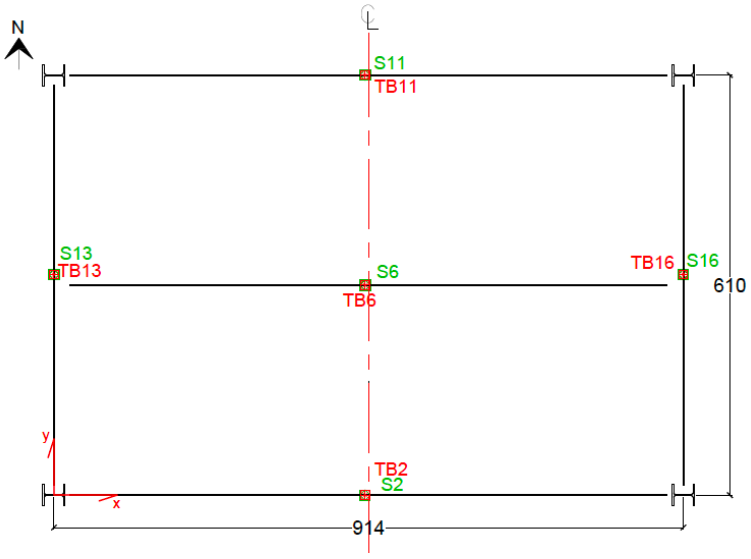

Name/ID	X East+ (cm)	Y North+ (cm)
S2, TB2	452	0
S6, TB6	452	305
S11, TB11	452	610
S13, TB13	0	320
S16, TB16	914	320

Fig. 58. Labels and locations of the group of thermocouples installed at the midspan composite beams (W16×31) and girders (W18×35). Dimensions and coordinates are in cm.

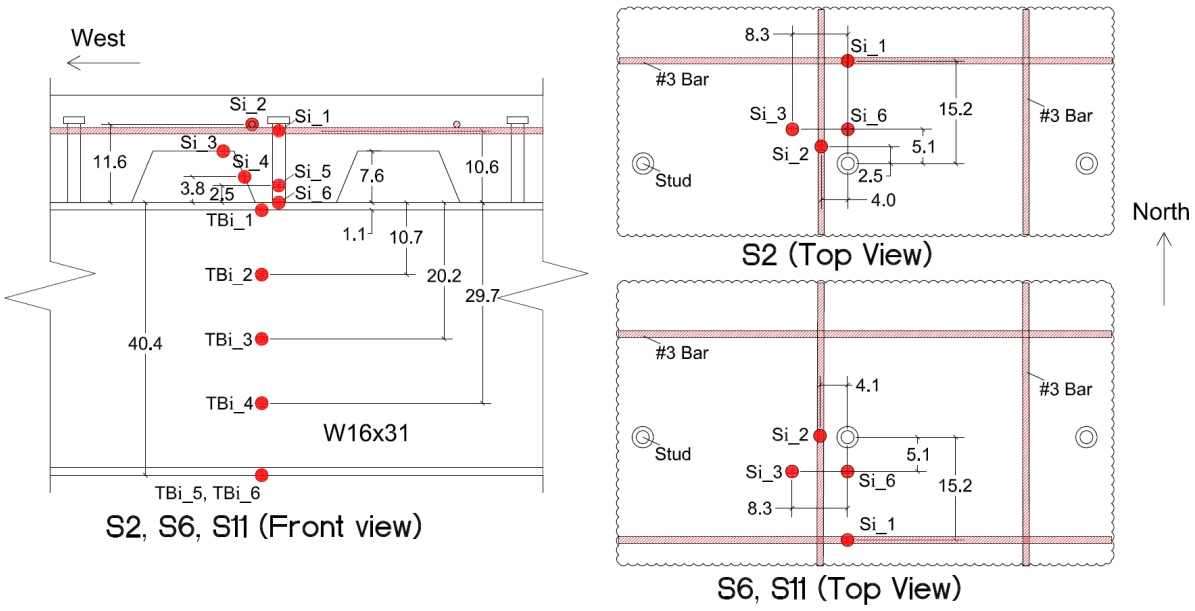

Fig. 59. Locations of individual thermocouples mounted at midspan of W16×31 composite beams, where i = thermocouple group number, 2, 6, or 11. Dimensions are in cm.

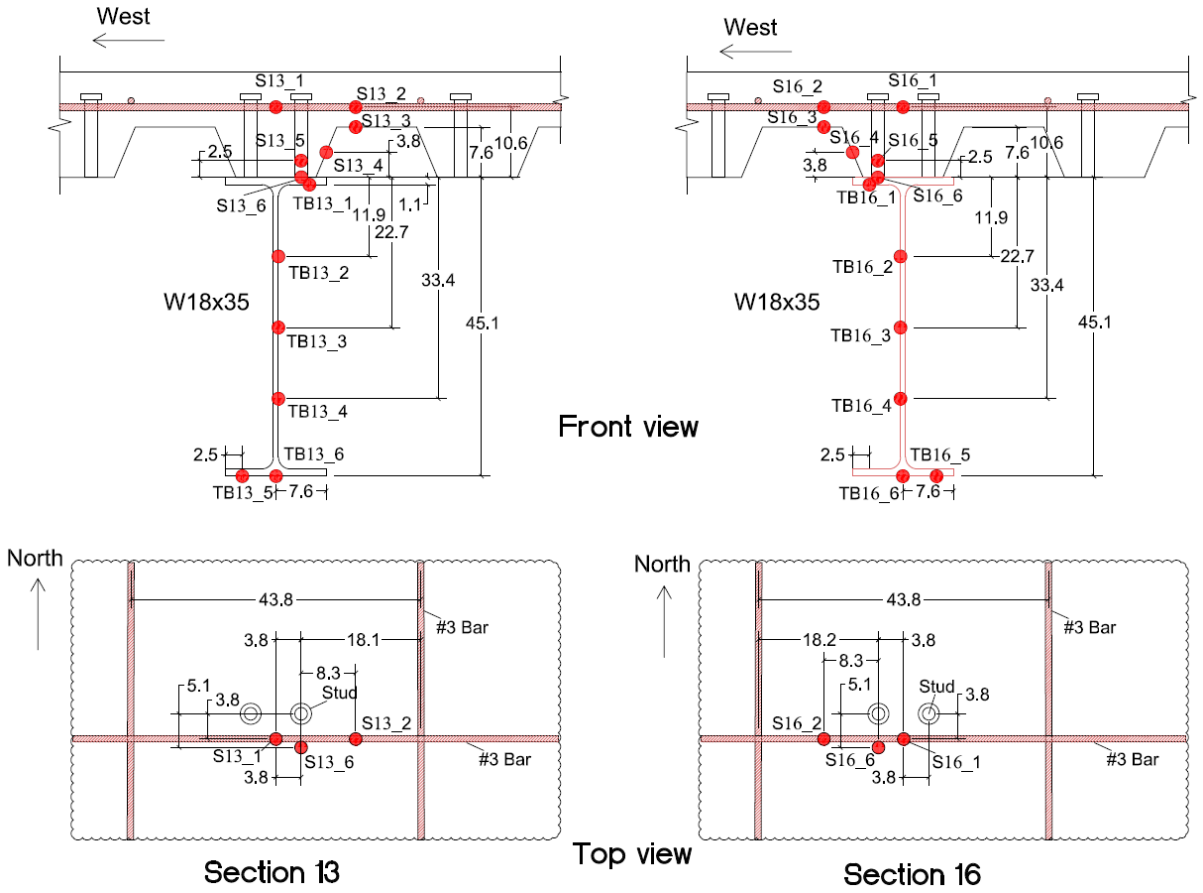

Fig. 60. Locations of individual thermocouples mounted at midspan of W18×35 composite girders, where i = thermocouple group number, 13 or 16. Dimensions are in cm.

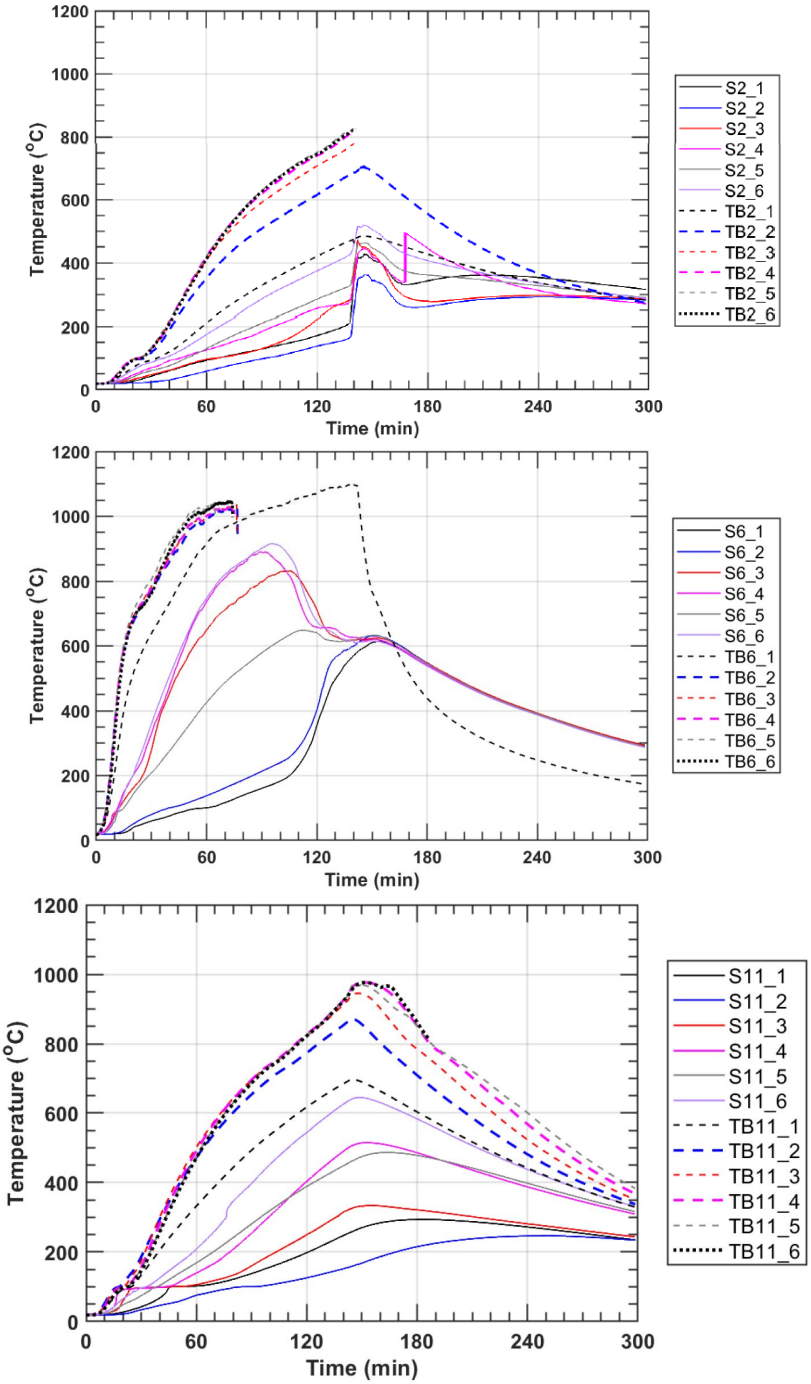
Temperature (°C)
Time (min)
S2_1
S2_2
S2_3
S2_4
S2_5
S2_6
TB2_1
TB2_2
TB2_3
TB2_4
TB2_5
TB2_6
S6_1
S6_2
S6_3
S6_4
S6_5
S6_6
TB6_1
TB6_2
TB6_3
TB6_4
TB6_5
TB6_6
S11_1
S11_2
S11_3
S11_4
S11_5
S11_6
TB11_1
TB11_2
TB11_3
TB11_4
TB11_5
TB11_6

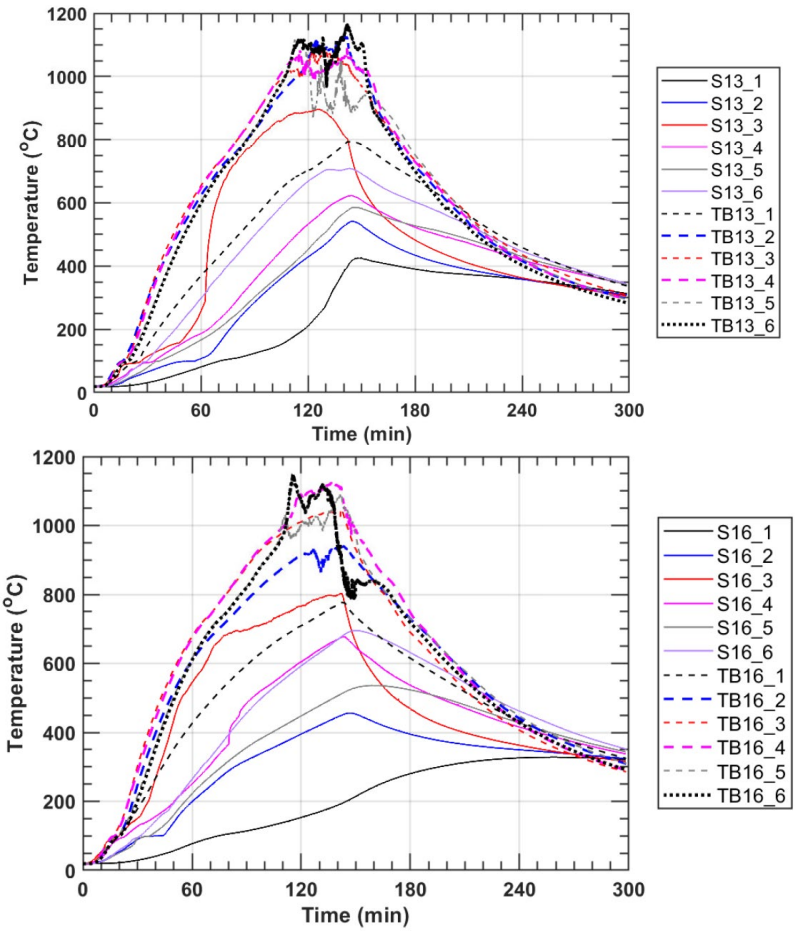

Fig. 61. Measured temperatures of mid-span composite beam and composite girder sections in the test bay.

Table 15. List of thermocouples used to estimate the average temperatures of composite beams and girders plotted in Fig. 23.

	Unprotected secondary Beam (W16×31)		Protected composite beams (W16×31)		Composite girders (W18×35)	
Plot legend	Channel ID	Max std, °C	Channel ID	Max std, °C	Channel ID	Max std, °C
(1)	S6_1, S6_2	150	S2_1, S2_2, S11_1, S11_2	110	S13_1, S13_2, S16_1, S16_2	150
(2)	S6_5	60	S2_5, S11_5	30	S13_5, S16_5	90
(3)	S6_3	110	S2_3, S11_3	40	S13_3, S16_3	20
(4)	S6_6	140	S2_6, S11_6	60	S13_6, S16_6	20
(5)	S6_4	120	S2_4, S11_4	60	S13_4, S16_4	40
(6)	TB6_1	60	TB2_1, TB11_1	160	TB13_1, TB16_1	40
(7)	TB6_3	50	TB2_3, TB11_3	100	TB13_3, TB16_3	40
(8)	TB6_5, TB6_6	30	TB2_5, TB2_6, TB11_5, TB11_6	60	TB13_5, TB13_6, TB16_5, TB16_6	120

A.6. Steel Beam and Girder Temperature

Ceramic sheathed thermocouples (model: XT-K-20-SLE) [33] were used to measure temperatures of the steel beams and girders in the fire test bay. Temperatures of the SFRM-protected steel beams (W16×31) and steel girders (W18×35) were measured at various locations. Temperatures measured in the sections TB2, TB6, TB11, TB13, and TB16 are presented in Sect. 3.3.2. Locations of remaining thermocouples and raw data are provided in Fig. 62 and Fig. 63, respectively.

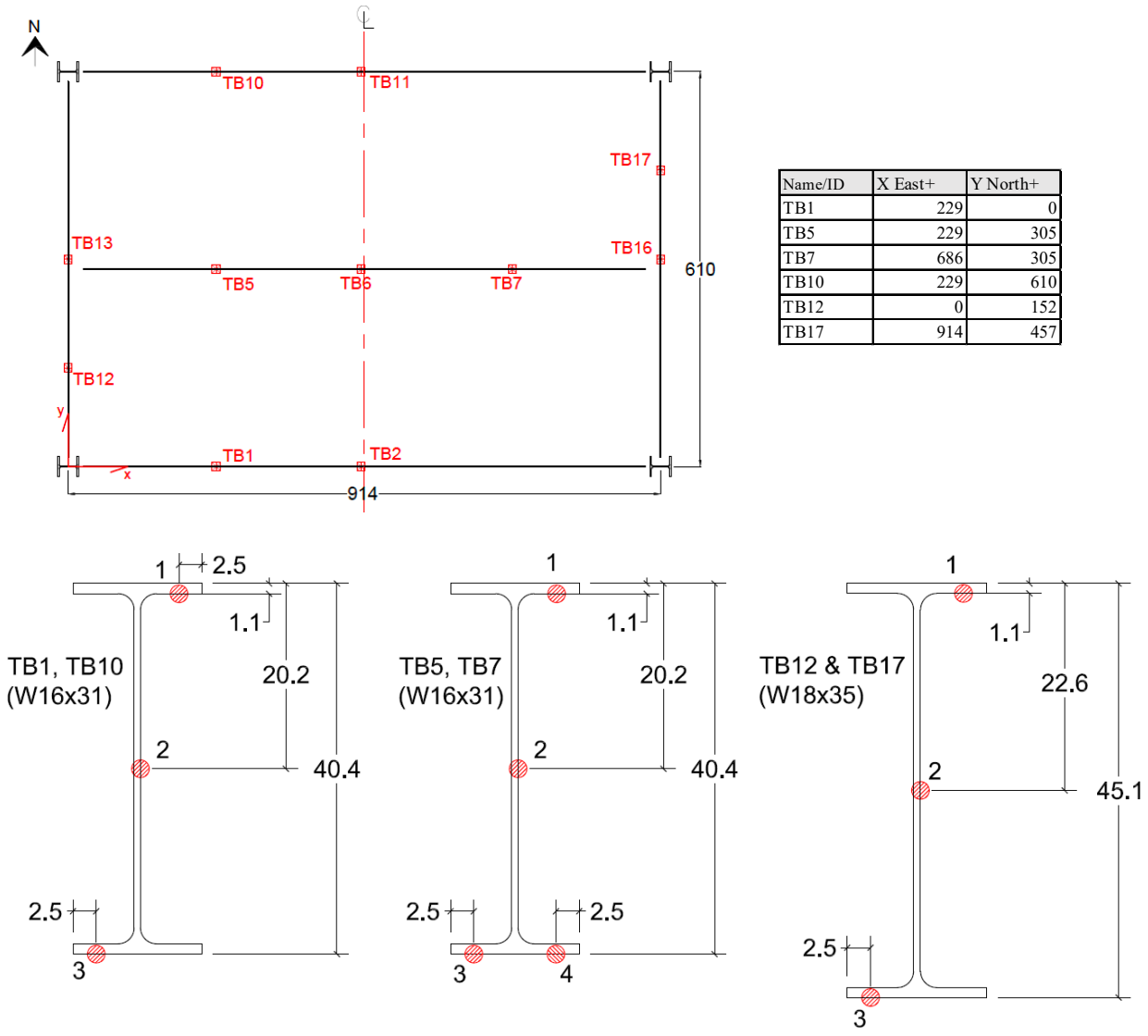

Name/ID	X East+	Y North+
TB1	229	0
TB5	229	305
TB7	686	305
TB10	229	610
TB12	0	152
TB17	914	457

Fig. 62. Locations of thermocouples mounted on steel beams and girders of the test floor assembly. Dimensions and coordinates are in cm.

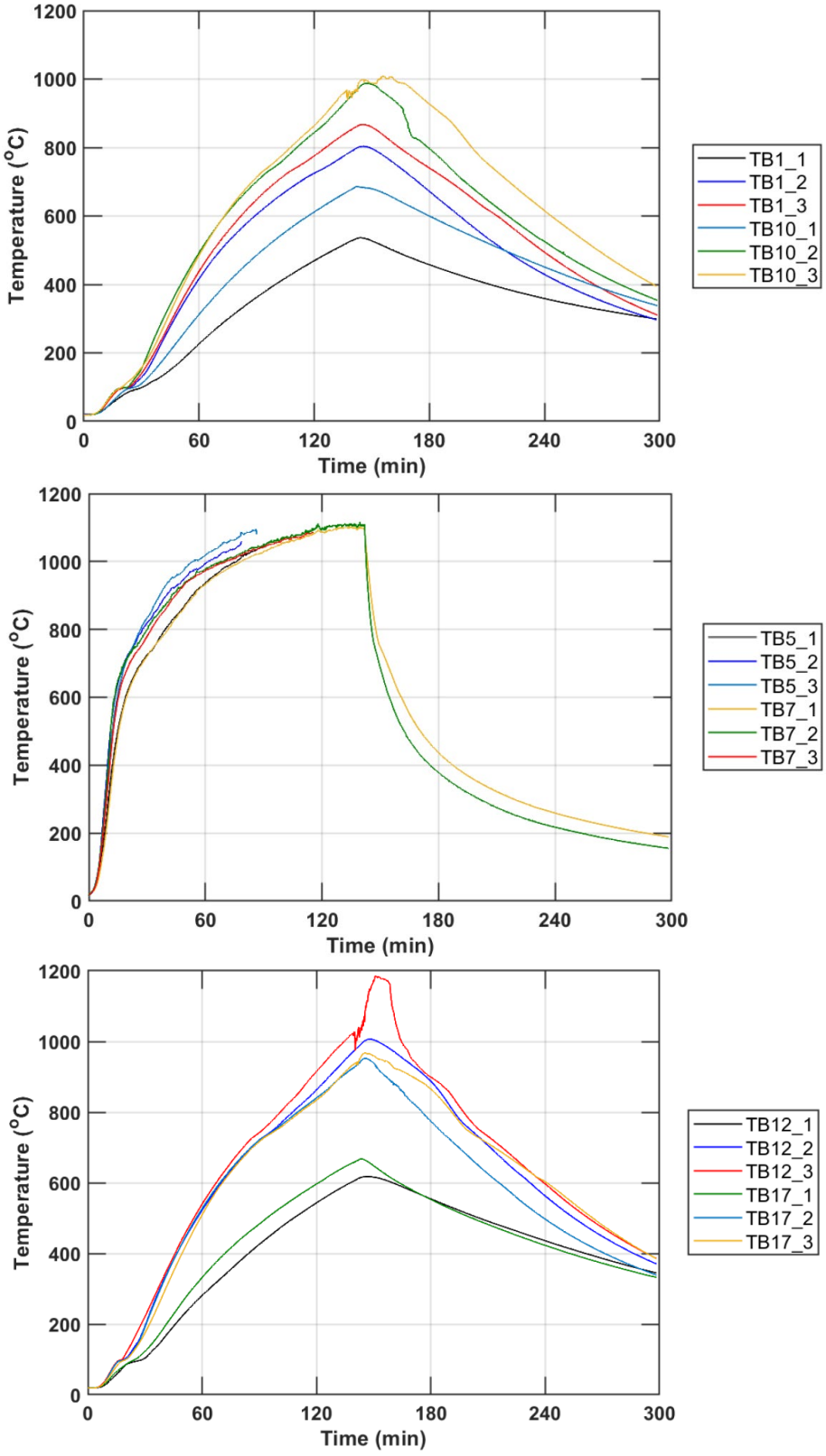

Fig. 63. Measured temperatures of steel beams and girders. Fire was extinguished at 142 min.

A.7. Steel Connection Temperature

Ceramic sheathed thermocouples (model: XT-K-20-SLE) [33] were used to measure temperatures on the beam-end connection regions. As shown in Fig. 64 (p. 76-79), the C group thermocouples were mounted on the steel connection elements protected with SFRM; the SC group thermocouples were installed inside the concrete slab and on the steel deck pan above the steel connections. Measured temperatures are plotted in Fig. 65 as a function of the fire exposure time.

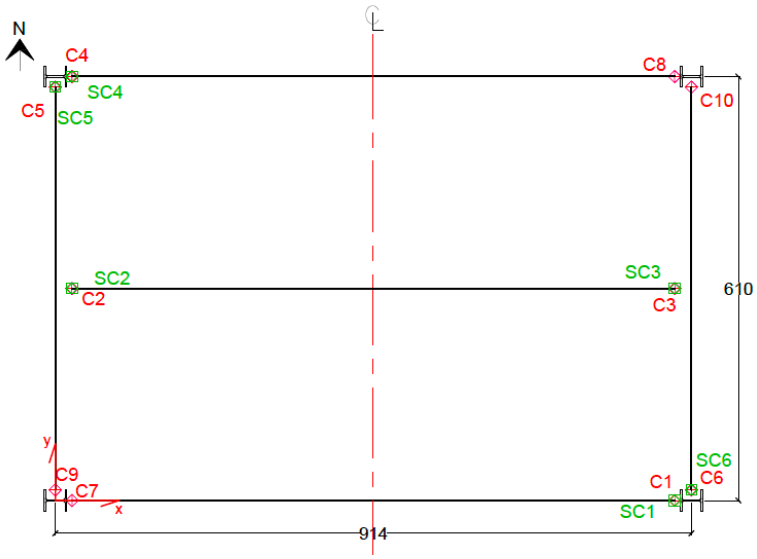

Name/ID	X East+	Y North+
C1, SC1	884	0
C2, SC2	8	305
C3, SC3	906	305
C4, SC4	30	610
C5, SC5	1	588
C6, SC6	914	22
C7	30	0
C8	884	610
C9	0	22
C10	914	588

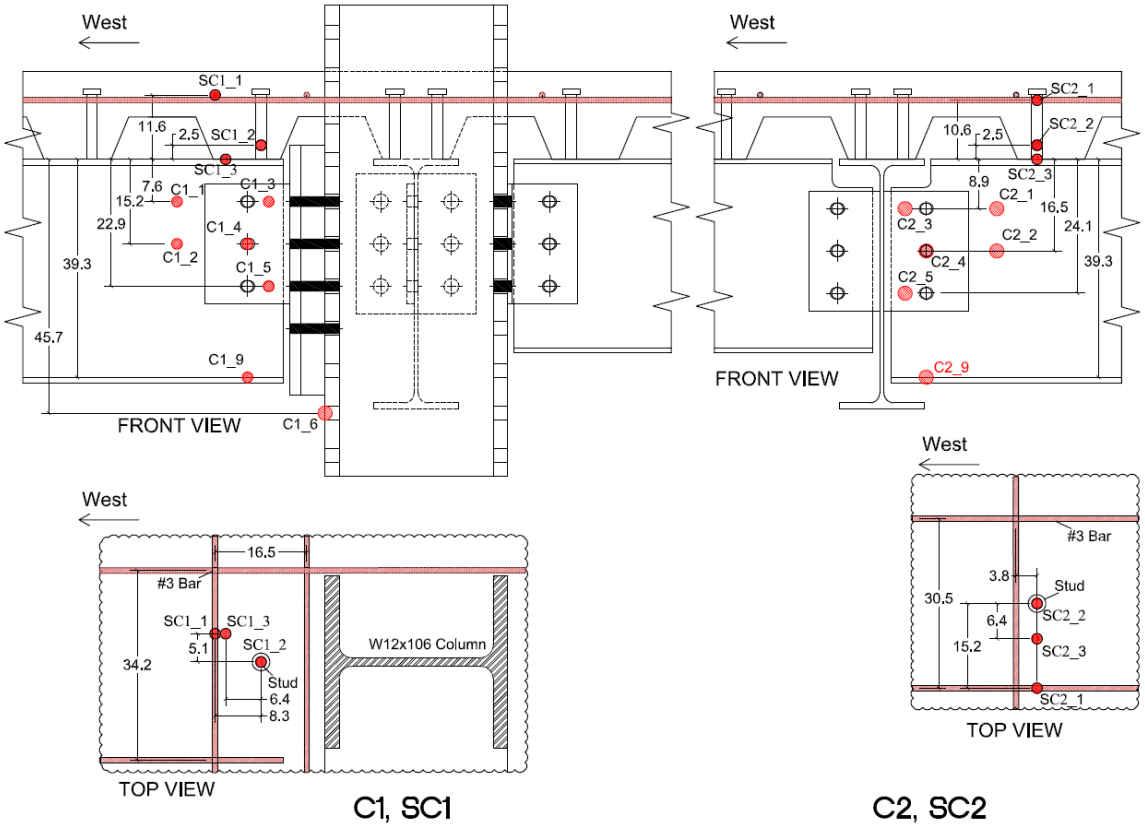

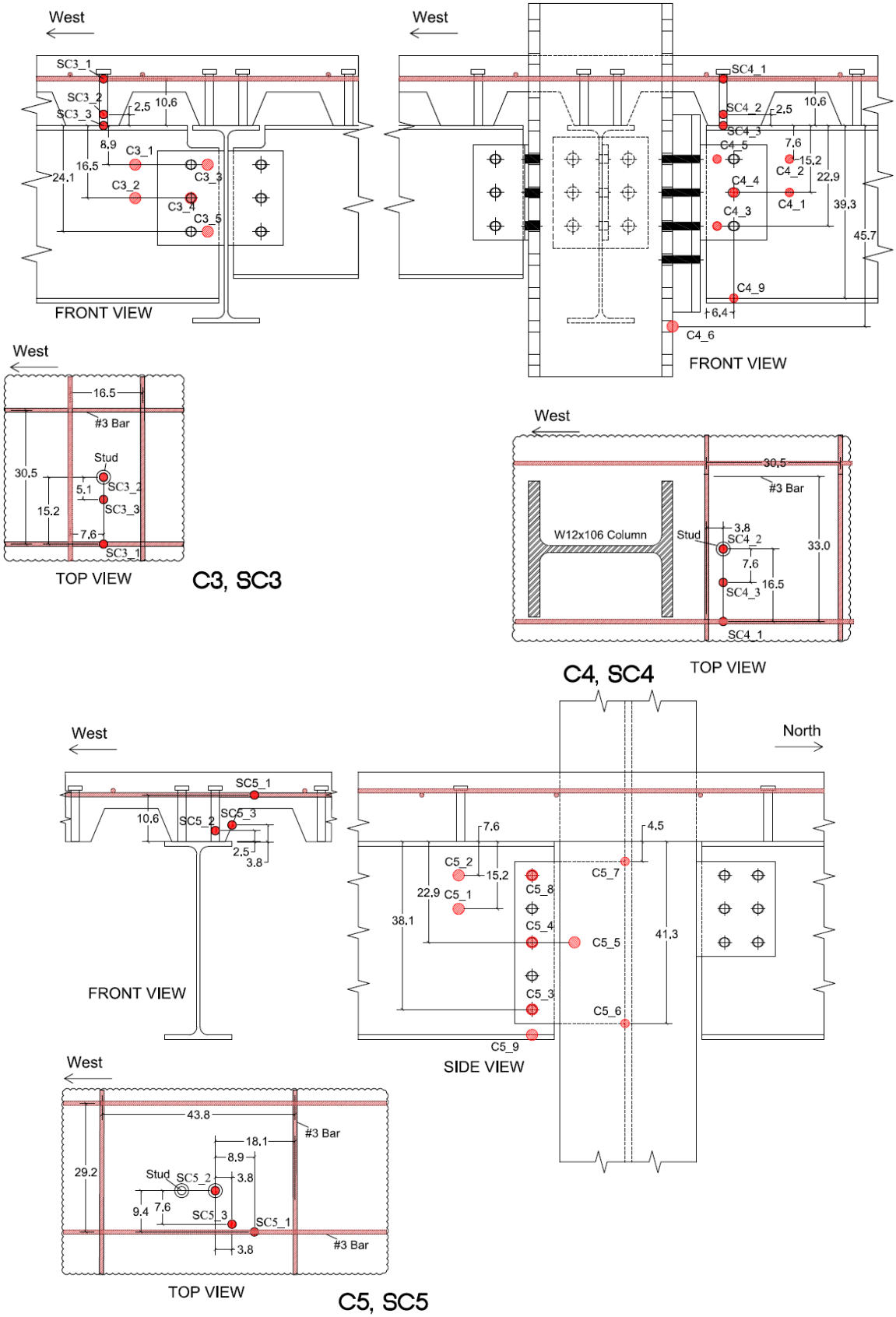
West
SC3_1
SC3_2
SC3_3
2.5
10.6
8.9
C3_1
16.5
C3_3
24.1
C3_2
C3_4
C3_5
FRONT VIEW
West
SC4_1
SC4_2
2.5
10.6
SC4_3
C4_5
7.6
15.2
C4_2
22.9
C4_4
C4_1
39.3
C4_3
45.7
C4_9
6.4
C4_6
FRONT VIEW
West
16.5
#3 Bar
Stud
30.5
5.1
SC3_2
SC3_3
15.2
7.6
SC3_1
TOP VIEW
C3, SC3
West
30.5
#3 Bar
W12x106 Column
Stud
3.8
SC4_2
33.0
7.6
16.5
SC4_3
SC4_1
C4, SC4
TOP VIEW
West
North
SC5_1
10.6
SC5_2
SC5_3
2.5
3.8
FRONT VIEW
7.6
4.5
C5_2
15.2
C5_7
C5_8
22.9
C5_1
38.1
C5_4
C5_5
41.3
C5_3
C5_6
C5_9
SIDE VIEW
West
43.8
#3 Bar
18.1
8.9
29.2
Stud
SC5_2
3.8
9.4
7.6
SC5_3
SC5_1
3.8
#3 Bar
TOP VIEW
C5, SC5

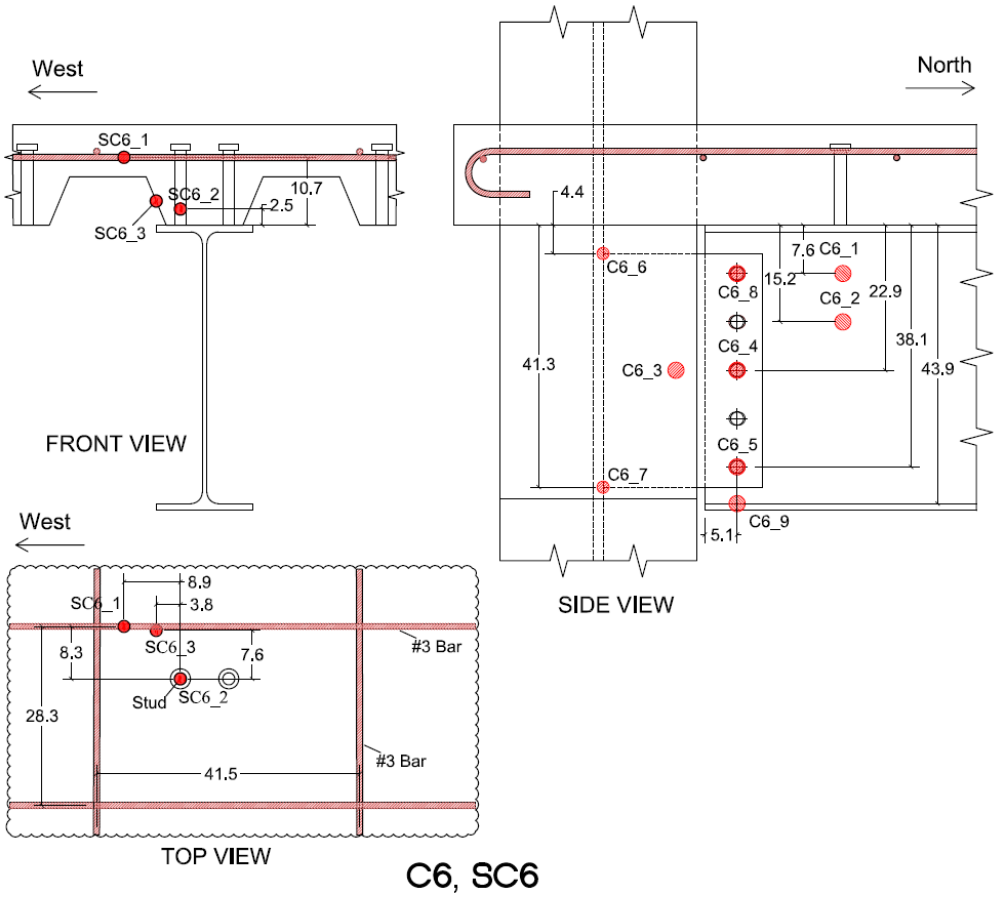
West
North
SC6_1
SC6_2
SC6_3
10.7
2.5
FRONT VIEW
4.4
C6_6
7.6
C6_1
15.2
C6_8
C6_2
22.9
C6_4
38.1
41.3
C6_3
43.9
C6_5
C6_7
C6_9
5.1
SIDE VIEW
West
8.9
SC6_1
3.8
SC6_3
#3 Bar
8.3
7.6
Stud
SC6_2
28.3
#3 Bar
41.5
TOP VIEW

C6, SC6

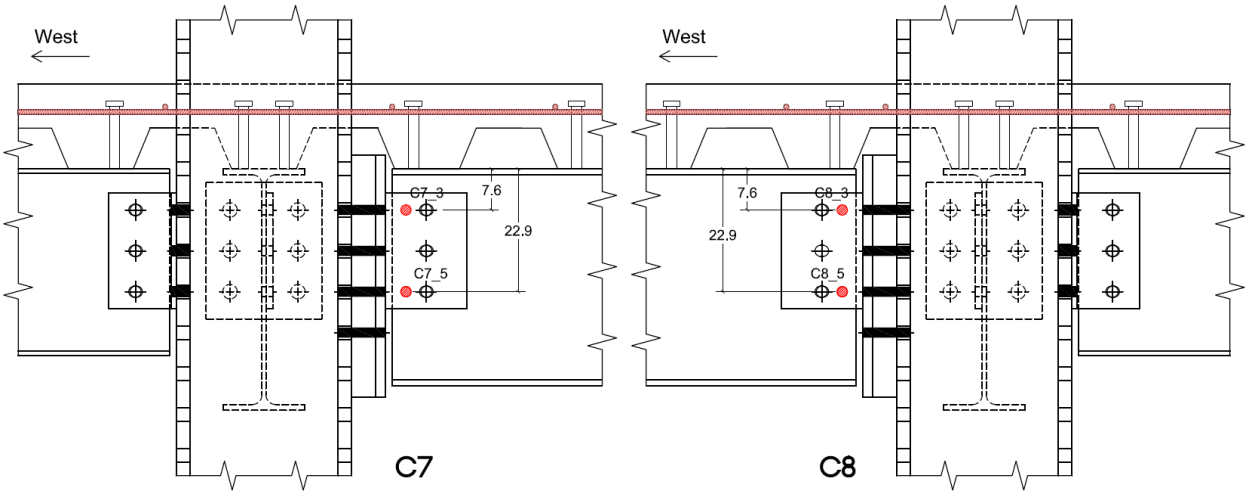
West
C7_3
7.6
22.9
C7_5
C7
West
7.6
C8_3
22.9
C8_5
C8

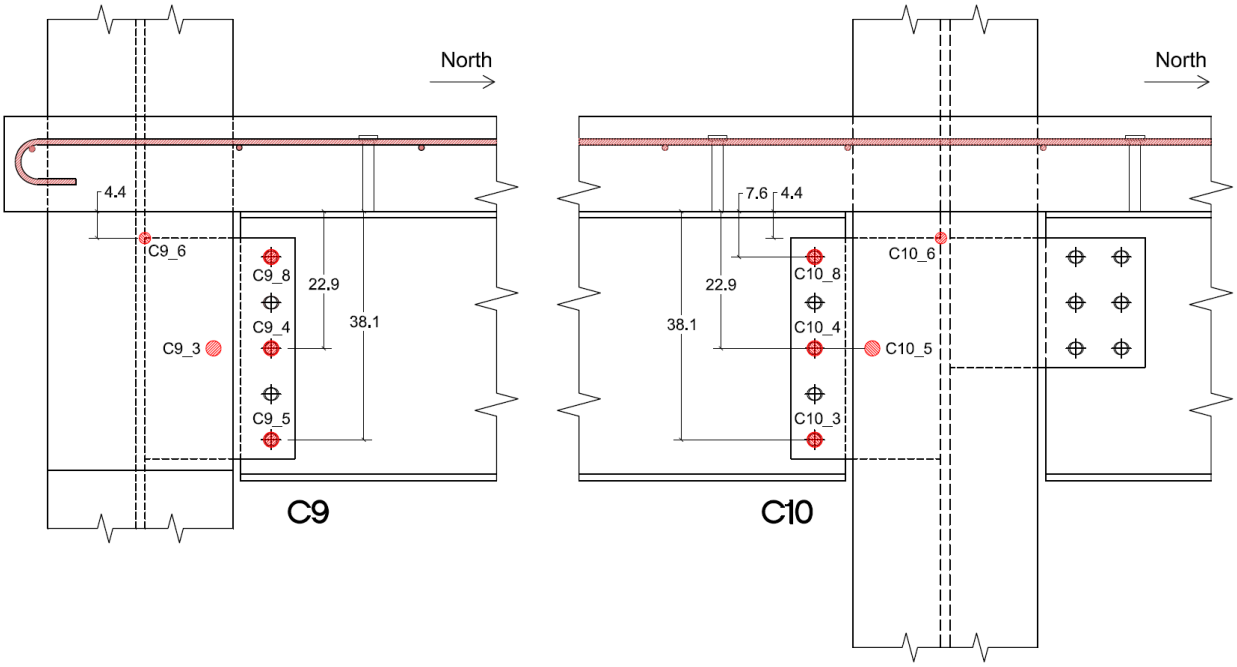

Fig. 64. Locations of thermocouples mounted on the beam-end connection regions. Dimensions and coordinates are in cm.

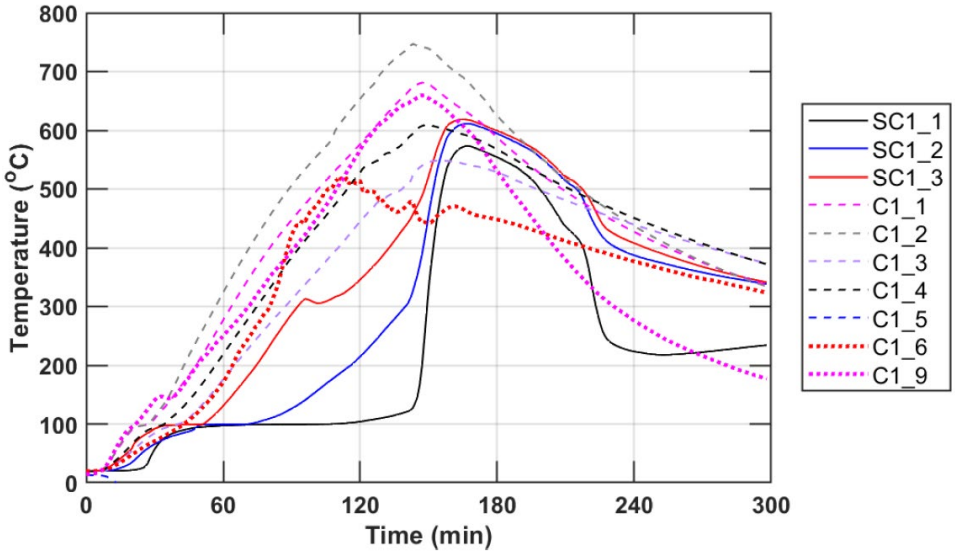

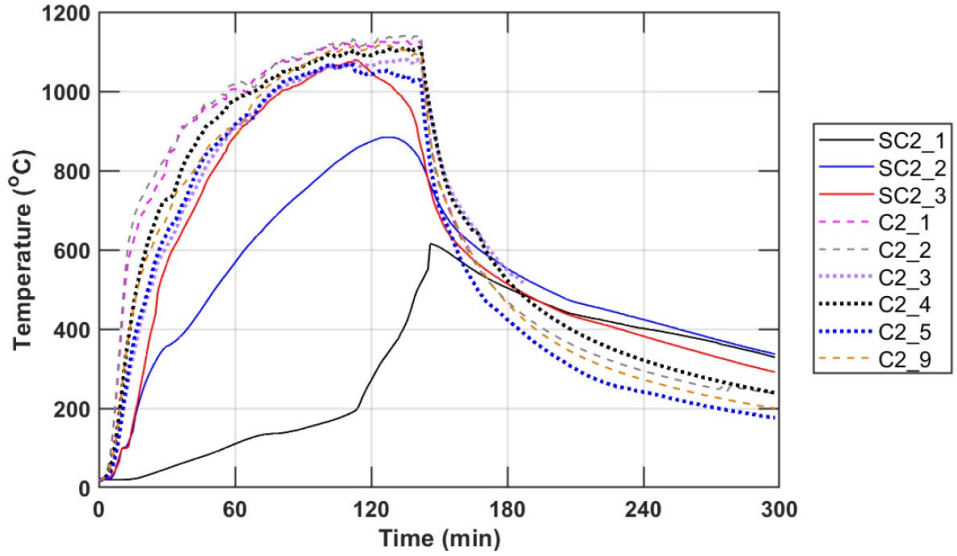
Temperature (°C)
Time (min)
SC2_1
SC2_2
SC2_3
C2_1
C2_2
C2_3
C2_4
C2_5
C2_9

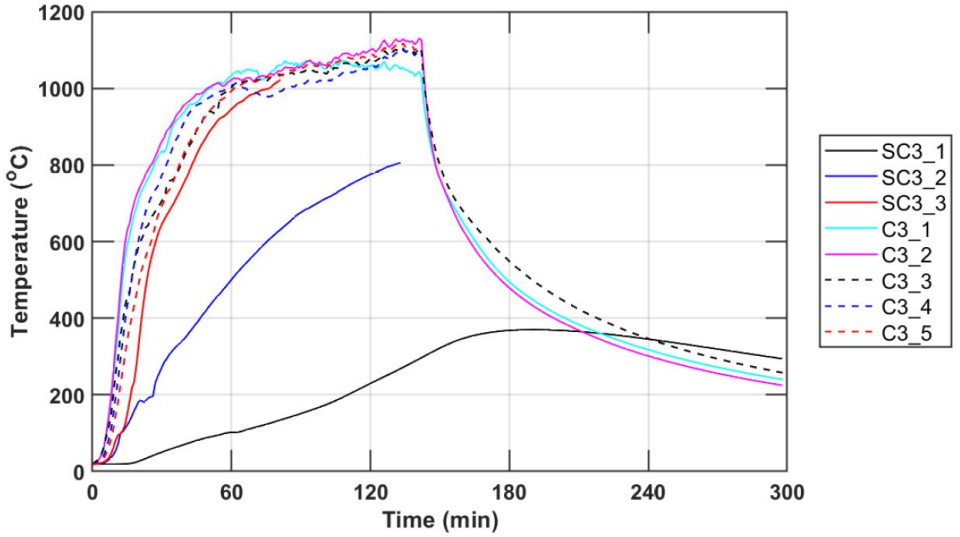
Temperature (°C)
Time (min)
SC3_1
SC3_2
SC3_3
C3_1
C3_2
C3_3
C3_4
C3_5

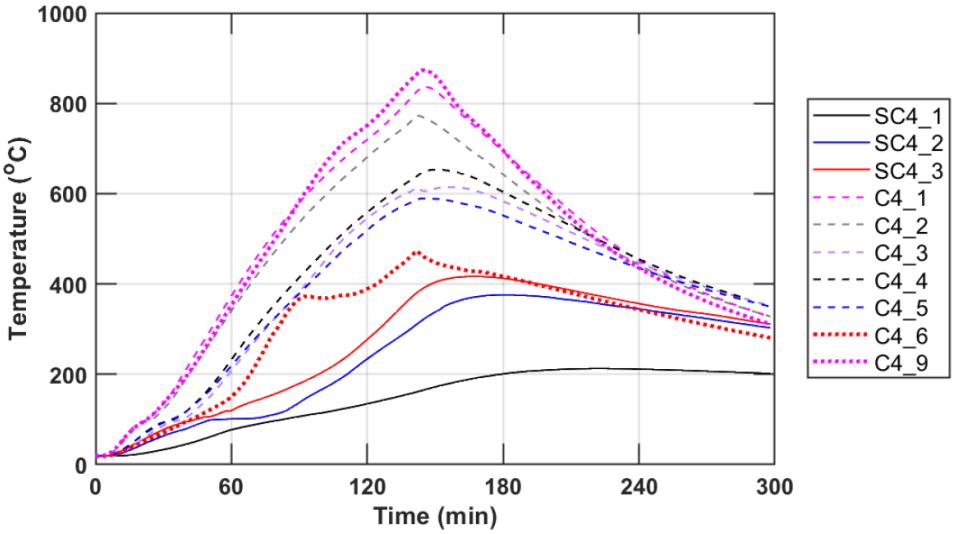
Temperature (°C)
Time (min)
SC4_1
SC4_2
SC4_3
C4_1
C4_2
C4_3
C4_4
C4_5
C4_6
C4_9

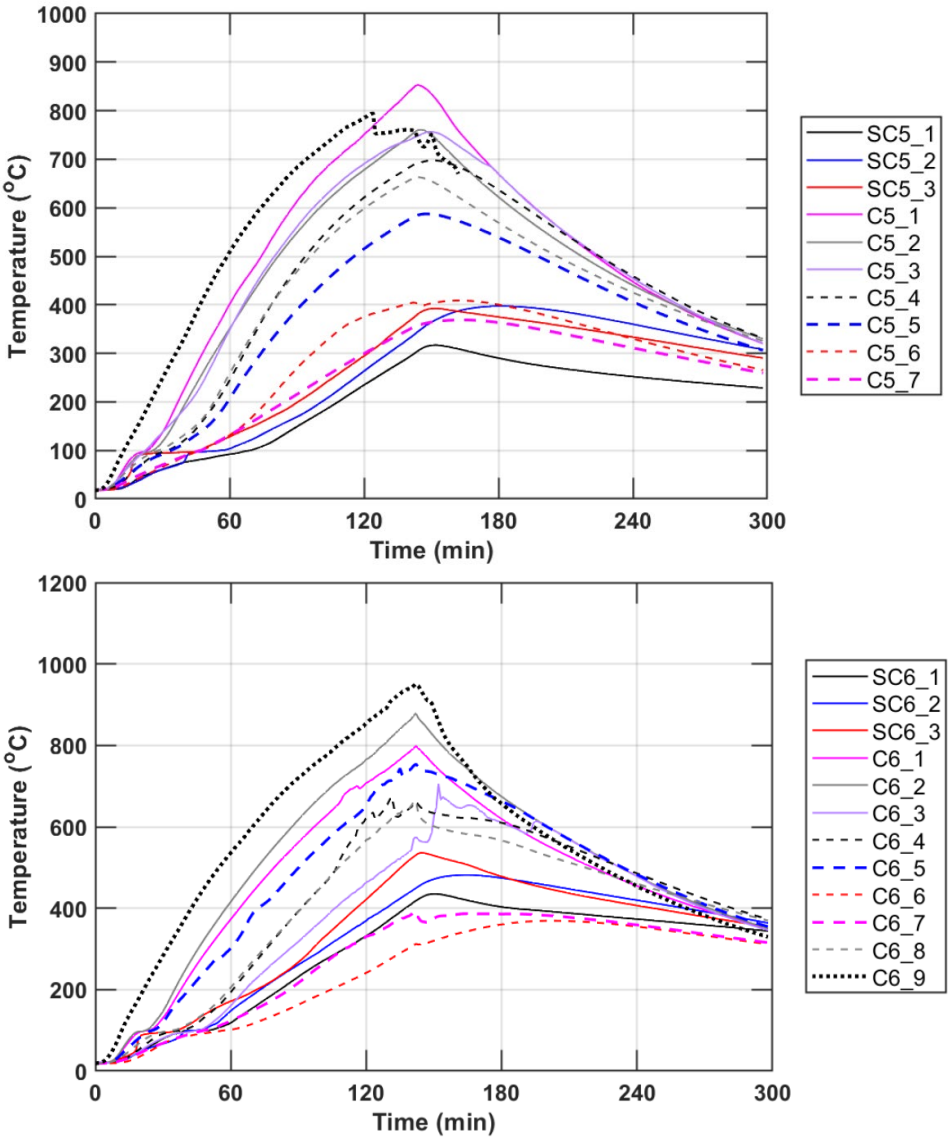
Temperature (°C)
Time (min)
SC5_1
SC5_2
SC5_3
C5_1
C5_2
C5_3
C5_4
C5_5
C5_6
C5_7
Temperature (°C)
Time (min)
SC6_1
SC6_2
SC6_3
C6_1
C6_2
C6_3
C6_4
C6_5
C6_6
C6_7
C6_8
C6_9

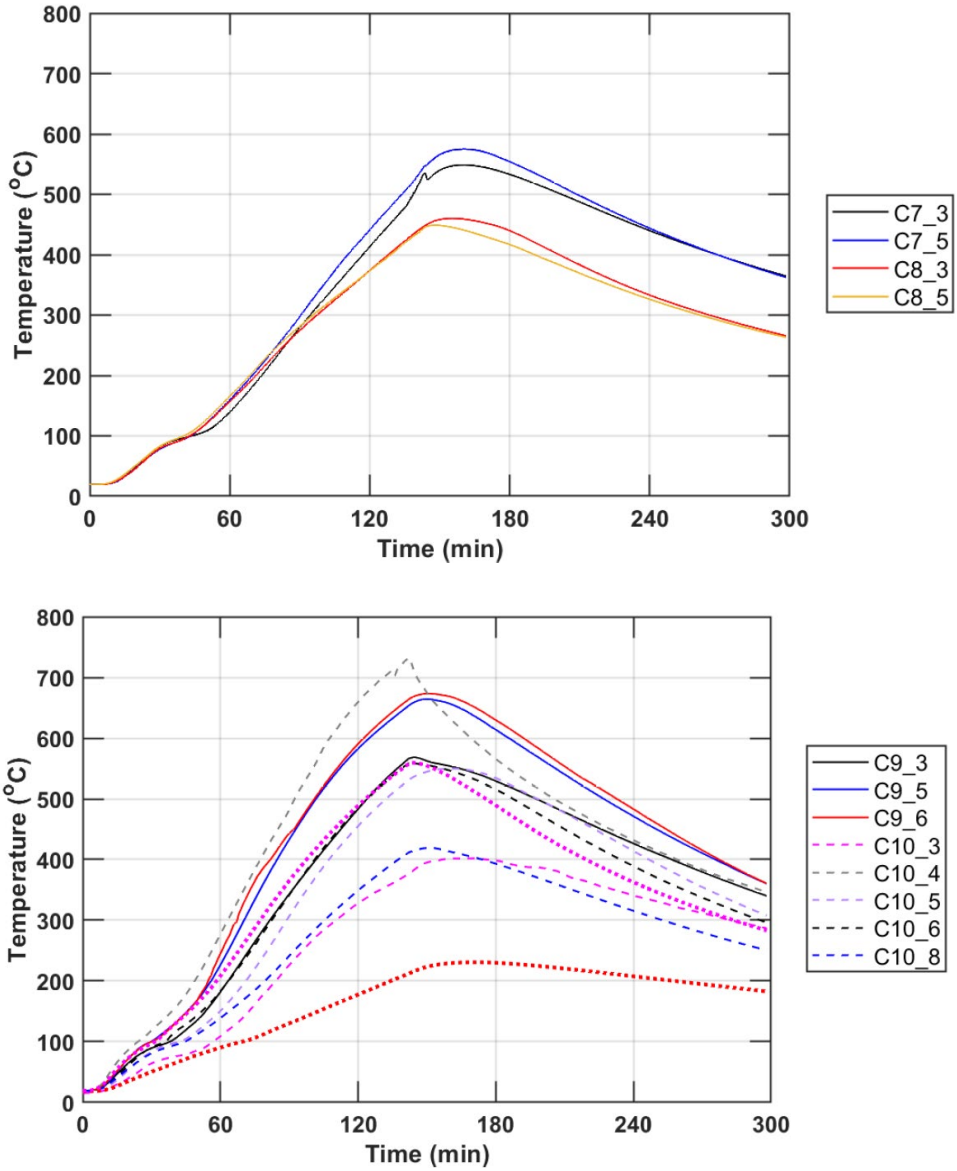

Fig. 65. Measured temperatures of the beam-end connection regions. Fire was extinguished at 142 min.

A.8. Displacement

Displacement measurements were performed using string potentiometers (model: PA series manufactured by UniMeasure [34]) All sensors were installed using mounting frames isolated from the test structure, except for VD11 which was used to measure the relative vertical displacement between the first and second story girders at midspan. Refer to Sect. 3.4 for locations of installed sensors. Fig. 66 shows the displacement data not presented in Sect. 3.4. The positive values on the y axes of the graph charts below indicate either the vertical displacement (VD) downward or the horizontal displacement (HD) at various locations of the test building in response to thermal expansion of the test floor during fire.

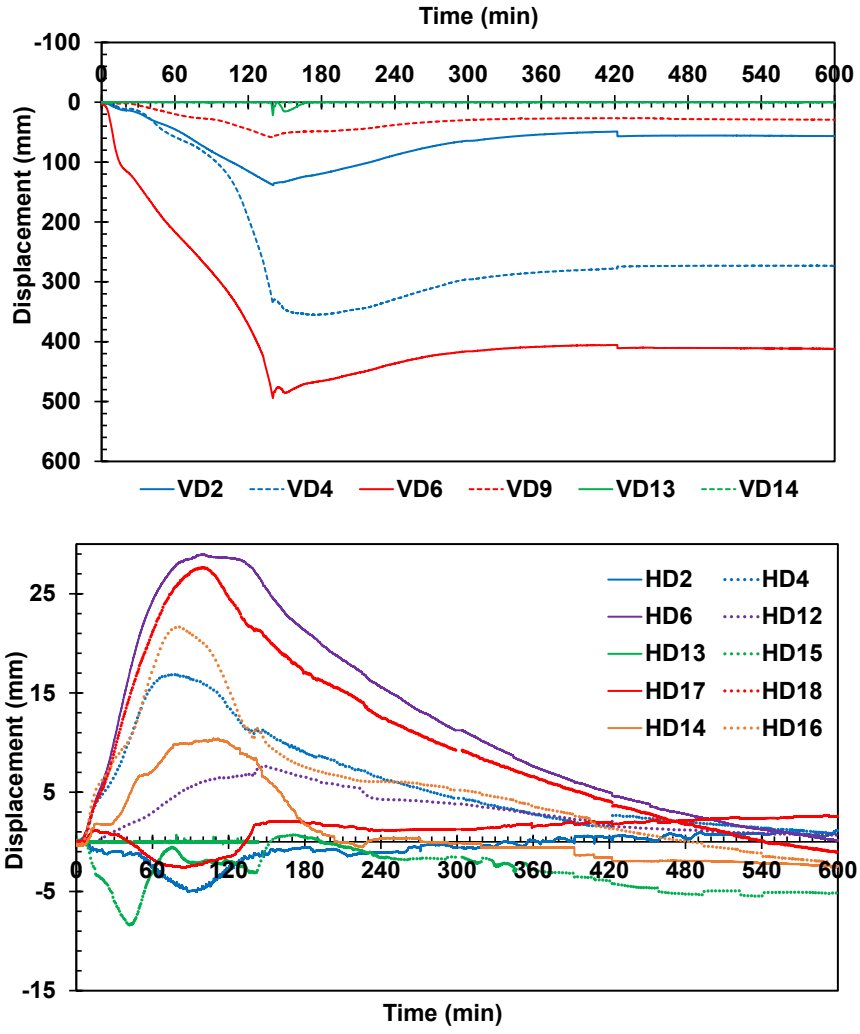

Fig. 66. Additional displacement data not included in Sect. 3.4.

A.9. Strain Measurements

Two different 120-ohm strain gauges, FLA-5-11 and QFLA-6-11 models [35] manufactured by Tokyo Measuring Instruments Lab., were mounted on the support columns and the surrounding beams to measure the change in strains in response to a compartment fire in the middle bay of the test building. Temperatures of those gauges remained below 50 °C. Locations of strain measurements are provided in Fig. 67. Column strains were measured at two levels. Strain gauges labeled with 0 through 3 were installed at 10 cm from the strong floor, and the remaining column strain gauges were installed at 34 cm from the strong floor.

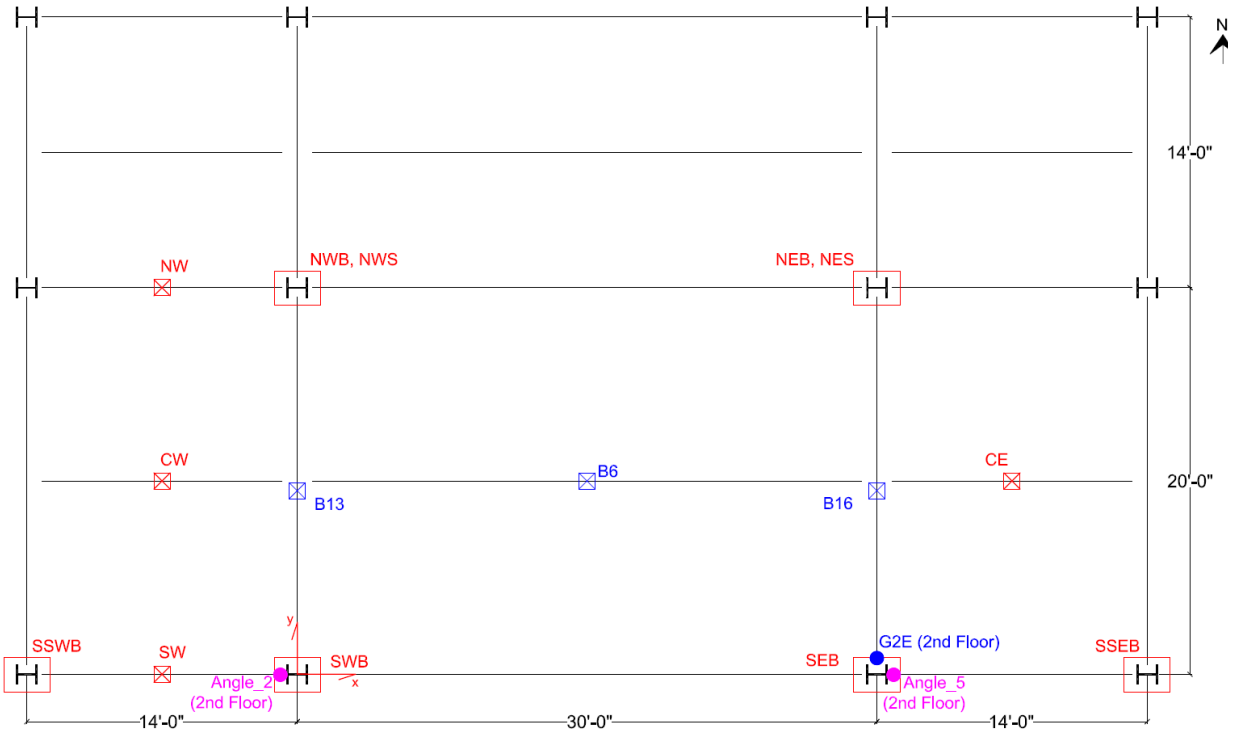

(a)

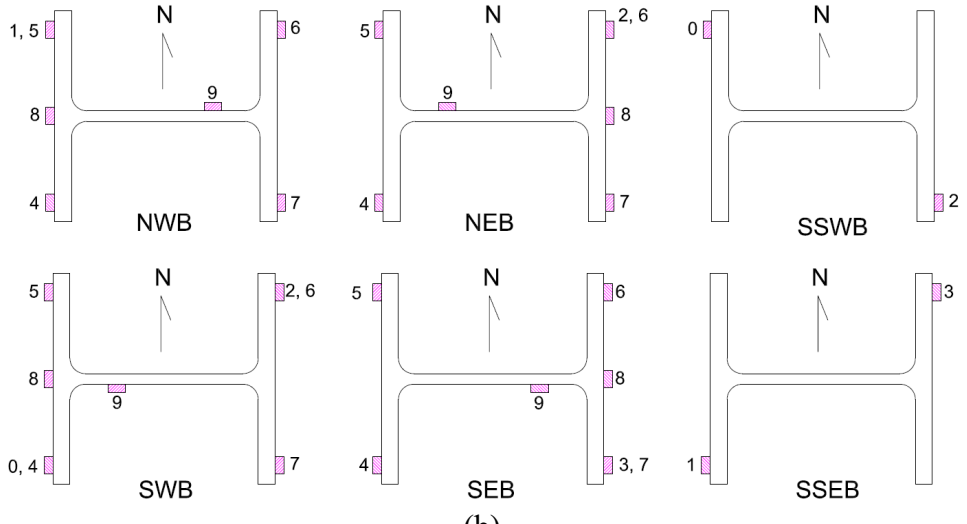

(b)

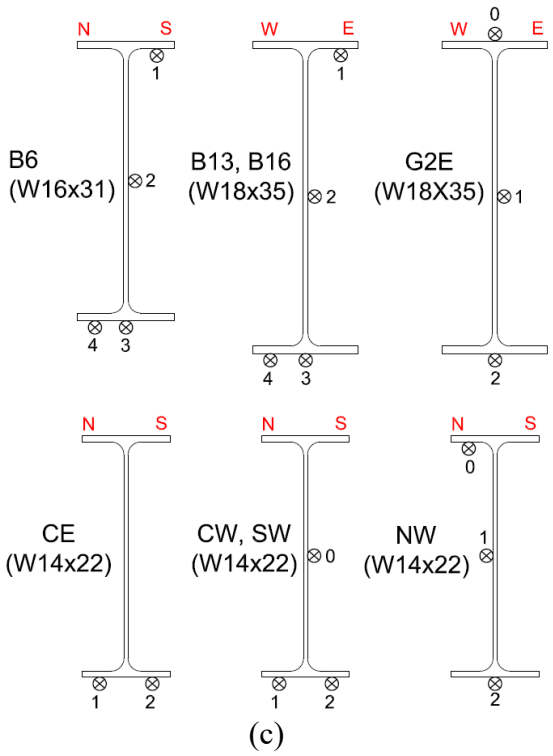

Fig. 67. (a) Locations and labels of strain measurements, (b) strain gauges installed at column base, and (c) strain gauges on the surrounding beams at the test floor level. Dimensions are in cm.

The column strains at a variety of locations are plotted in Fig. 68. As shown, the columns were subjected to variable bi-directional bending moments in response to thermal expansion or contraction of the test floor assembly. Based on the magnitude of strains, the northeast and northwest columns of the fire test bay were subjected to thermally induced lateral forces relatively smaller than those applied to the southeast and southwest columns. Local buckling of the north edge beam at their ends likely occurred around 70 min after ignition of the test fire as NWB and NEB reached their peak value at that time. Web local buckling of the girders at their ends likely occurred around 100 min when SWB and SEB reached their peak values. The strains in the west-bay beams at midspan are shown in Fig. 69. In the west-bay secondary beam, compressive forces increased until 60 min into heating and then began to decrease due to local buckling of the test-bay secondary beam.

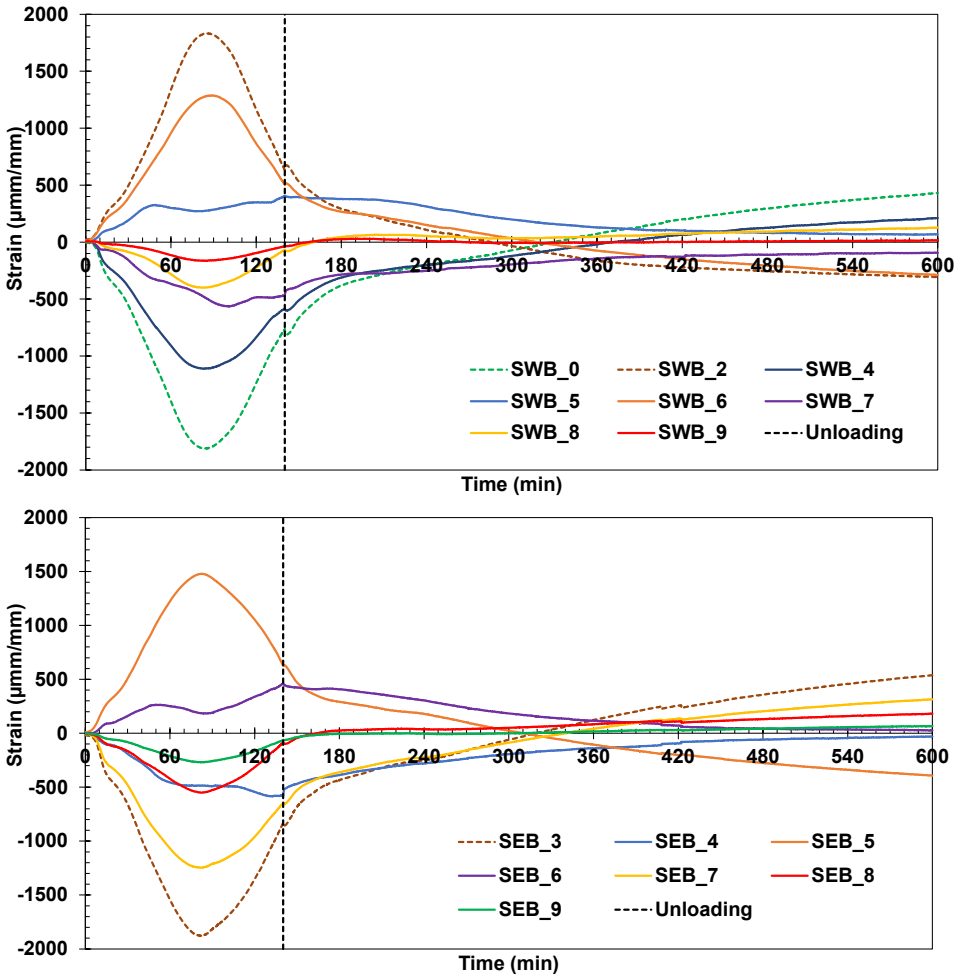
Strain (μmm/mm)
Time (min)
SWB_0
SWB_2
SWB_4
SWB_5
SWB_6
SWB_7
SWB_8
SWB_9
Unloading
Strain (μmm/mm)
Time (min)
SEB_3
SEB_4
SEB_5
SEB_6
SEB_7
SEB_8
SEB_9
Unloading

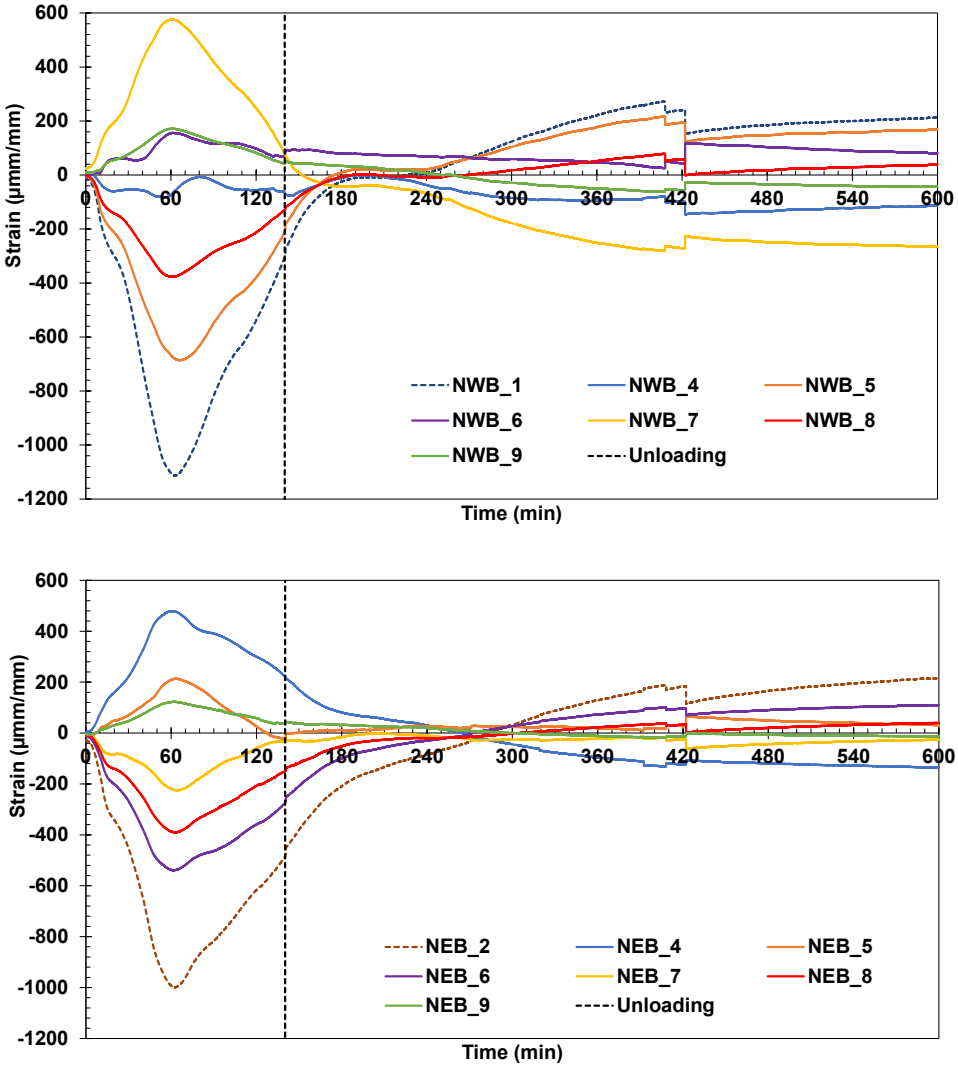

Fig. 68. Strains of test bay columns.

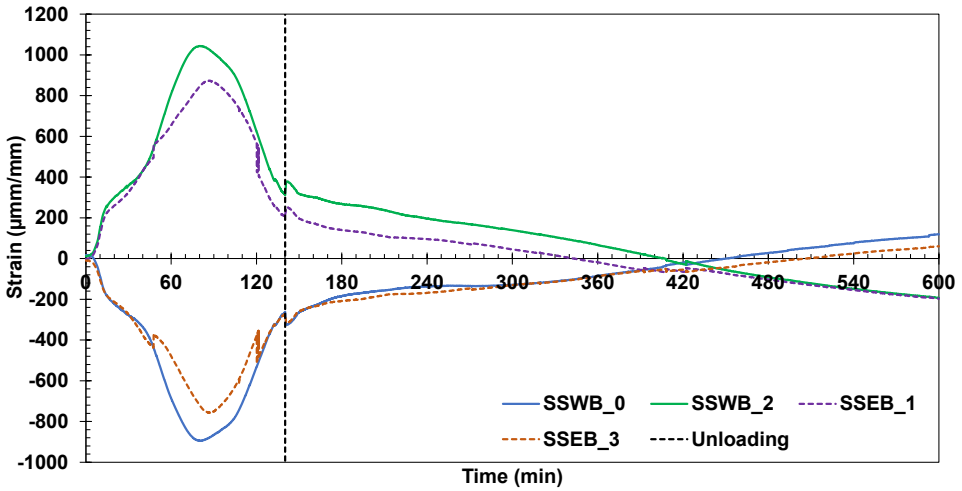
Strain (μmm/mm)
Time (min)
SSWB_0
SSWB_2
SSEB_1
SSEB_3
Unloading

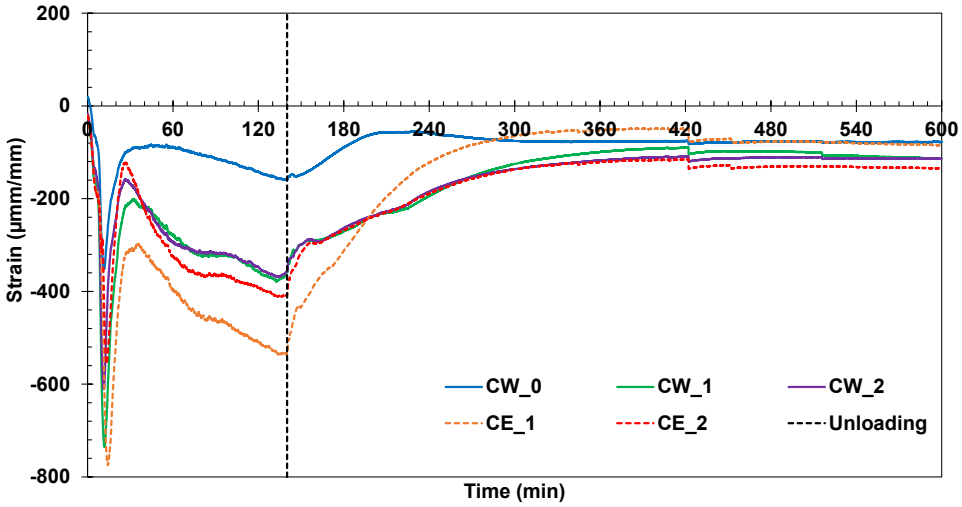
Strain (μmm/mm)
Time (min)
CW_0
CW_1
CW_2
CE_1
CE_2
Unloading

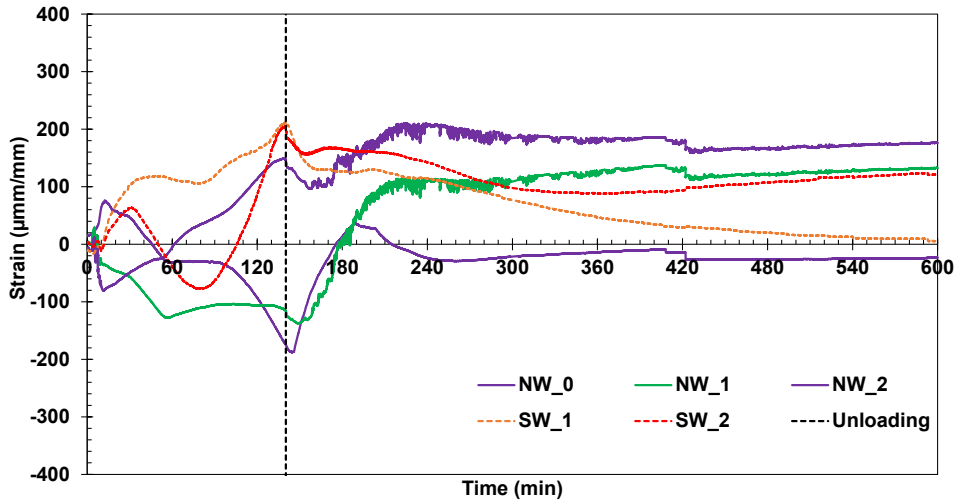
Strain (μmm/mm)
Time (min)
NW_0
NW_1
NW_2
SW_1
SW_2
Unloading

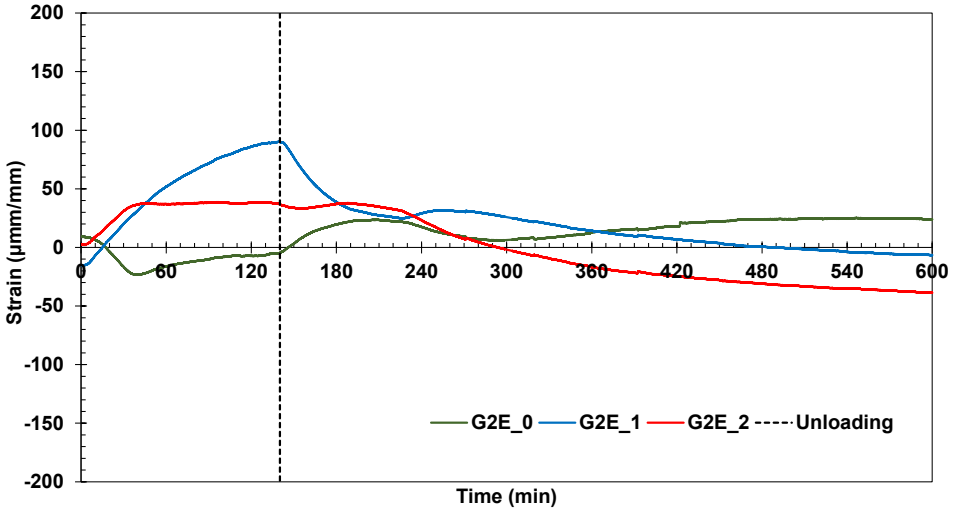

Fig. 69. Strains of surrounding columns and steel beams.

A.10. Compartment Opening Velocity and Temperature

The fire induced flow of gasses was measured at the large (southeast and southwest) and small (northeast and northwest) vents. A vertical array of bare bead thermocouples (Type-K) was used to estimate gas temperature at each vent. Gas velocity at selected locations was determined using bi-directional probes placed adjacent to the thermocouples. Four velocity probes were placed in the large vents and one velocity probe in the small vents, as shown in Fig. 70 and Fig. 71. The pressure differential across the bi-directional probes was measured using precision capacitance manometers (MKS 220CD Baratron) [36]. Refer to Zhang et al. [20] for details on the velocity measurement.

Gas temperatures and velocities measured at the large (south) and small (north) openings are shown in Fig. 72, along with the average upper layer gas temperature (Avg. UGL) measured using twelve TCC thermocouples. Positive velocity indicates hot gases flowing out of the compartment, while negative velocity indicates ambient air flowing into the compartment.

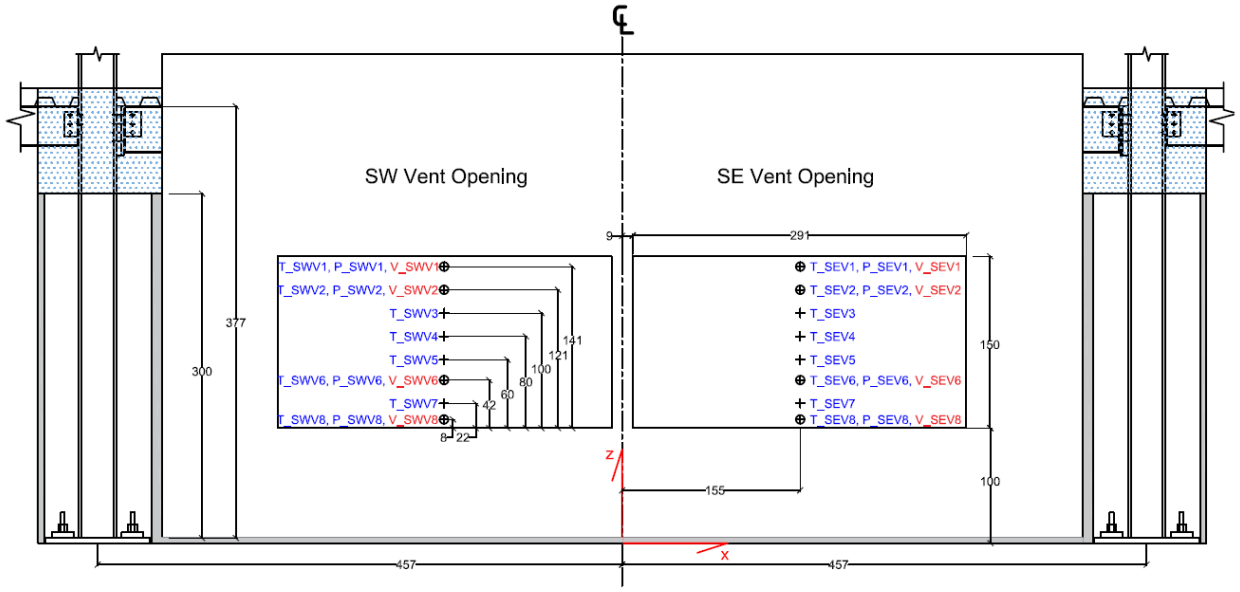
SW Vent Opening
SE Vent Opening
T_SWV1, P_SWV1, V_SWV1
T_SWV2, P_SWV2, V_SWV2
T_SWV3
T_SWV4
T_SWV5
T_SWV6, P_SWV6, V_SWV6
T_SWV7
T_SWV8, P_SWV8, V_SWV8
T_SEV1, P_SEV1, V_SEV1
T_SEV2, P_SEV2, V_SEV2
T_SEV3
T_SEV4
T_SEV5
T_SEV6, P_SEV6, V_SEV6
T_SEV7
T_SEV8, P_SEV8, V_SEV8
9
291
377
300
141
121
100
80
60
42
22
8
150
100
155
z
x
457
457

(a)

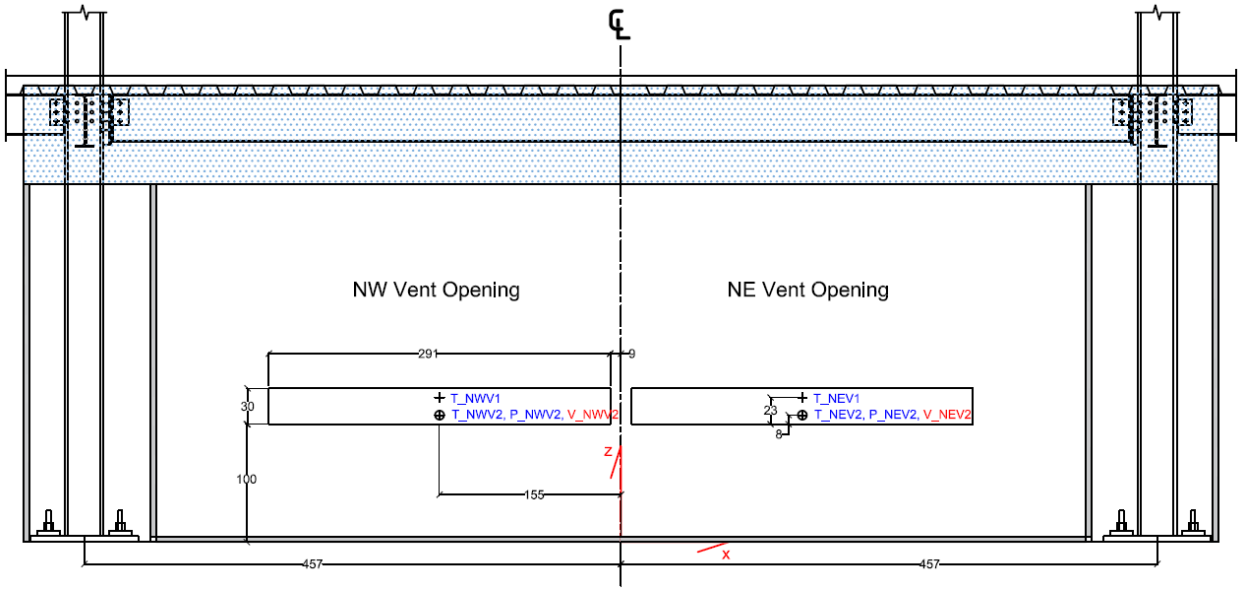
NW Vent Opening
NE Vent Opening
T_NWV1
T_NWV2, P_NWV2, V_NWV2
T_NEV1
T_NEV2, P_NEV2, V_NEV2
291
9
30
100
155
23
8
z
x
457
457

(b)

Name/ID	X East+	Z Up+
T_SWV1, P_SWV1, V_SWV1	-155	241
T_SWV2, P_SWV2, V_SWV2	-155	221
T_SWV3	-155	201
T_SWV4	-155	180
T_SWV5	-155	160
T_SWV6, P_SWV6, V_SWV6	-155	142
T_SWV7	-155	122
T_SWV8, P_SWV8, V_SWV8	-155	108

Name/ID	X East+	Z Up+
T_SEV1, P_SEV1, V_SEV1	155	241
T_SEV2, P_SEV2, V_SEV2	155	221
T_SEV3	155	201
T_SEV4	155	180
T_SEV5	155	160
T_SEV6, P_SEV6, V_SEV6	155	142
T_SEV7	155	122
T_SEV8, P_SEV8, V_SEV8	155	108

Name/ID	X East+	Z Up+
T_NWV1	-155	123
T_NWV2, P_NWV2, V_NWV2	-155	108

Name/ID	X East+	Z Up+
T_NEV1	155	123
T_NEV2, P_NEV2, V_NEV2	155	108

Fig. 70. Thermocouple and bi-directional probe locations in the south ventilation opening of the compartment (a) south opening; (b) north opening. Dimensions are in cm.

(a)

(b)

Fig. 71. Thermocouple Installed bi-directional probes and thermocouples on (a) south and (b) north vent openings of the test compartment during the fire test.

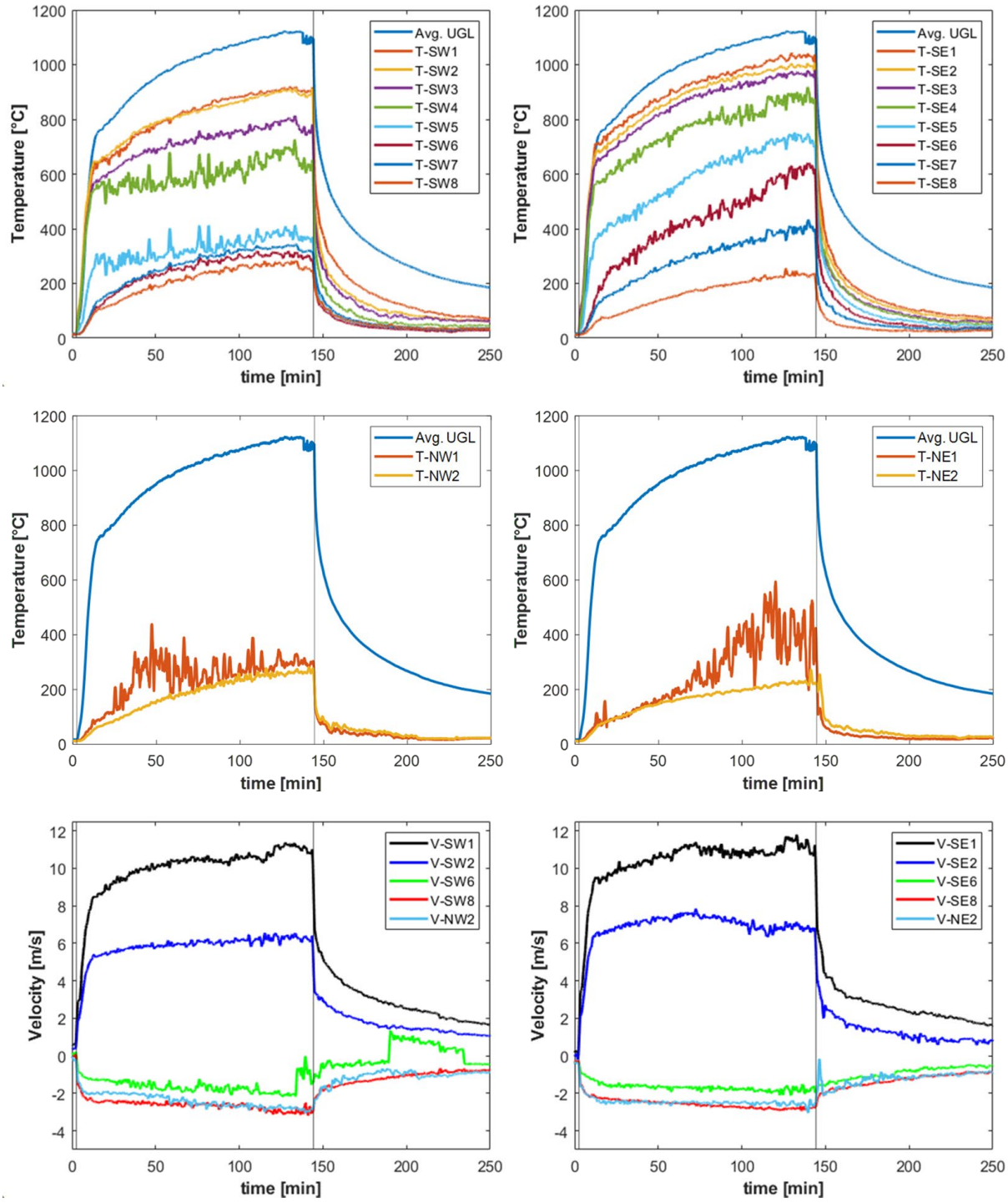

Fig. 72. Vent opening temperatures (top and middle) and gas flow velocities (bottom). Values shown are a 120s moving average.

A.11. Additional Post-Test Photographs

After the test, the concrete slab was removed to examine the headed stud anchors and the steel deck. Section 3.5.1 details the structural failure of the shear studs along the unprotected secondary beam. Most of the shear studs in the west half of the secondary beam as well as in the east end of the secondary beam exhibited stud fracture or large bending. Figure 73 through Figure 75 shows the shear studs along the other test bay beams. These shear studs did not exhibit any rupture or large bending.

Figure 76 shows some post-test photographs of the fire damaged steel deck under the concrete slab. As shown, the test fire caused extensive damages to the steel decking across the entire test bay. As shown in Fig. 76, large steel deck ruptures developed in parallel to the secondary beam as well as at the west side of the slab, where bolt ruptures at the shear tab connection, at the west end of the secondary beam, was observed.

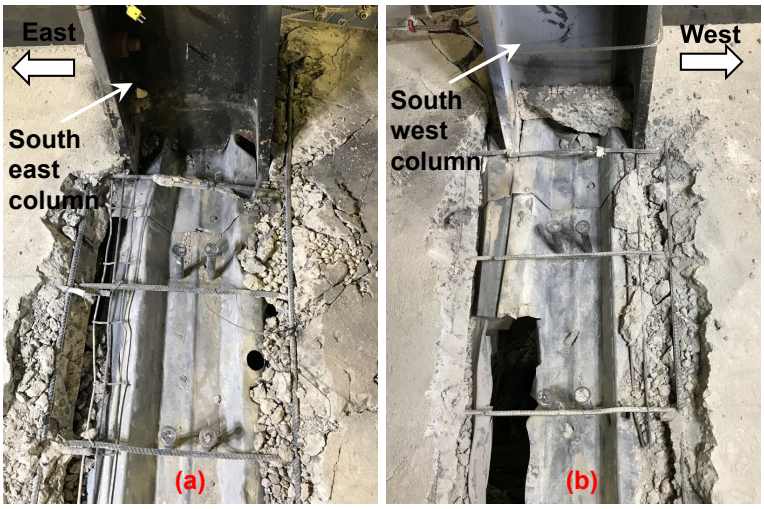

Fig. 73. Post-test photographs of headed studs after concrete removal (a) at the south end of east girder; (c) at the south end of west girder in the test bay.

Fig. 74. Post-test photographs of headed studs (a) at the east end of north beam before concrete removal; (b) at the east end of north beam after concrete removal; (c) at the west end of north beam before concrete removal; (d) at the west end of north beam after concrete removal.

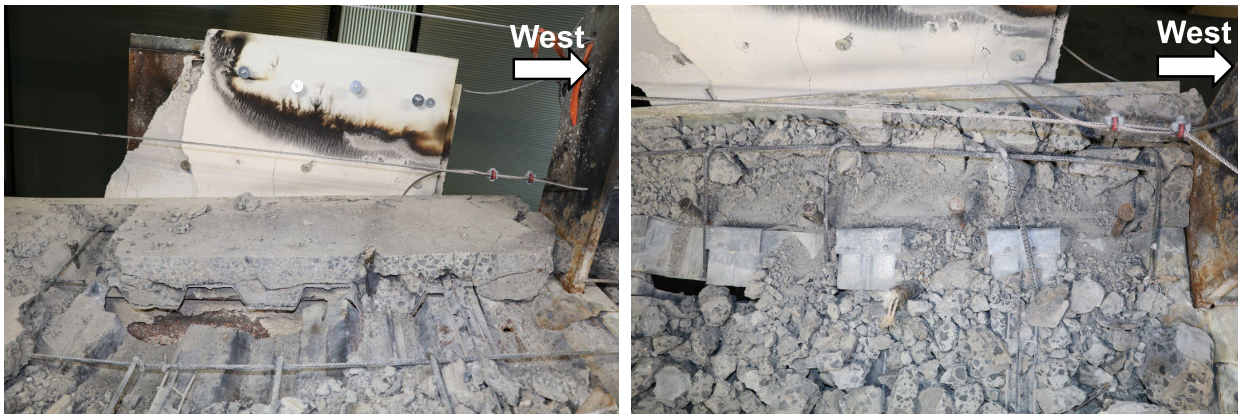

(a)

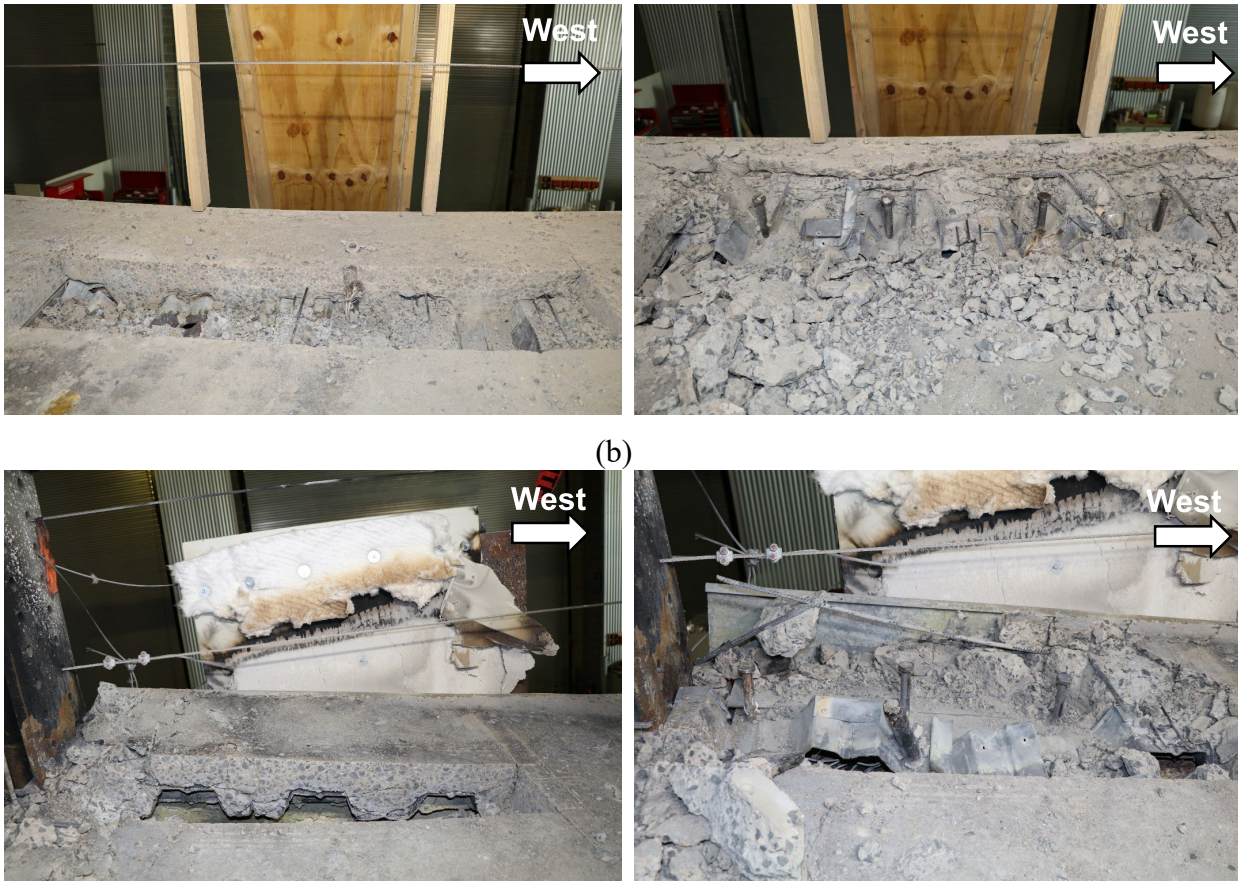

Fig. 75. Post-test photographs of headed studs before and after concrete removal (a) at the west end of south beam; (b) at the mid-span of south beam; (c) at the east end of south beam.

Fig. 76. Post-test photographs of steel deck ruptures (a) at the west side; (b) at the mid-span.

Some photographs of the shear tab connections after the fire test are shown in Fig. 77. As detailed in Section 3.5.2, all three bolts in the unprotected shear tab connection between the unprotected secondary beam and girder fractured during heating. The west shear tab connection of the north primary beam exhibited bolt fracture during the cooling phase. As shown in Fig. 77,

severe flange and web local buckling were present at the ends of the north and south beams of the test bay. This was because the bottom flange of the W16×31 beams was bearing against the web of the girder or the column flange introducing large compressive forces as these beams expanded under fire loading. The girders had local web buckling only at their ends since the girder flange never put into contact with the web of the support columns due to a large initial setback distance.

Fig. 77. Post-test photographs of test bay connections (a) at the north east corner; (b) at the north west corner; (c) at the south east corner; (d) at the south west corner of the test bay.

A.12. Engineering Stress-Strain Curves of Steel Material Used in the Test

Figure 78 shows the measured engineering stress-strain diagrams of the steel materials used in Test #3. Where the data end, the operator removed the extensometer. Table 2 provides the average values of the 0.2 % offset yield strength (S_y), the ultimate tensile strength (S_u), and percent elongation at fracture (δ_u). The values after ± symbols indicate one standard deviation estimated using a uniform distribution of the two or more measured values. A gauge length of 51 mm was used to measure the strains in the flat coupons. The gauge length of the round coupons (bolts and wires) was four times the diameter of the specimen. The elongation (δ_u) was equal to a ratio of the final elongation after testing to the initial gauge length.

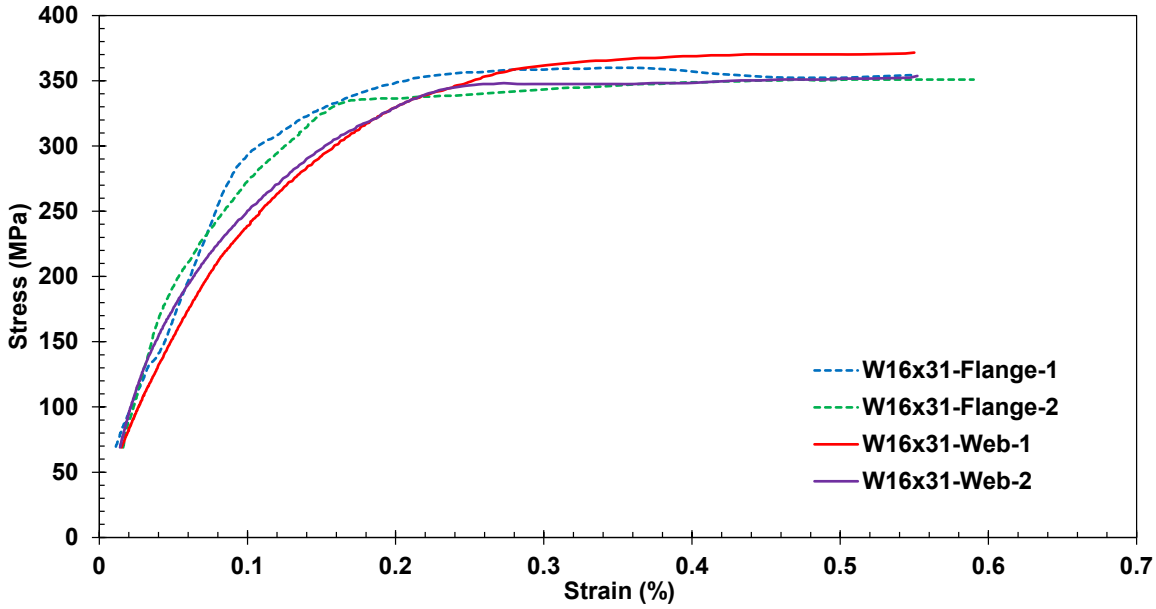

(a)

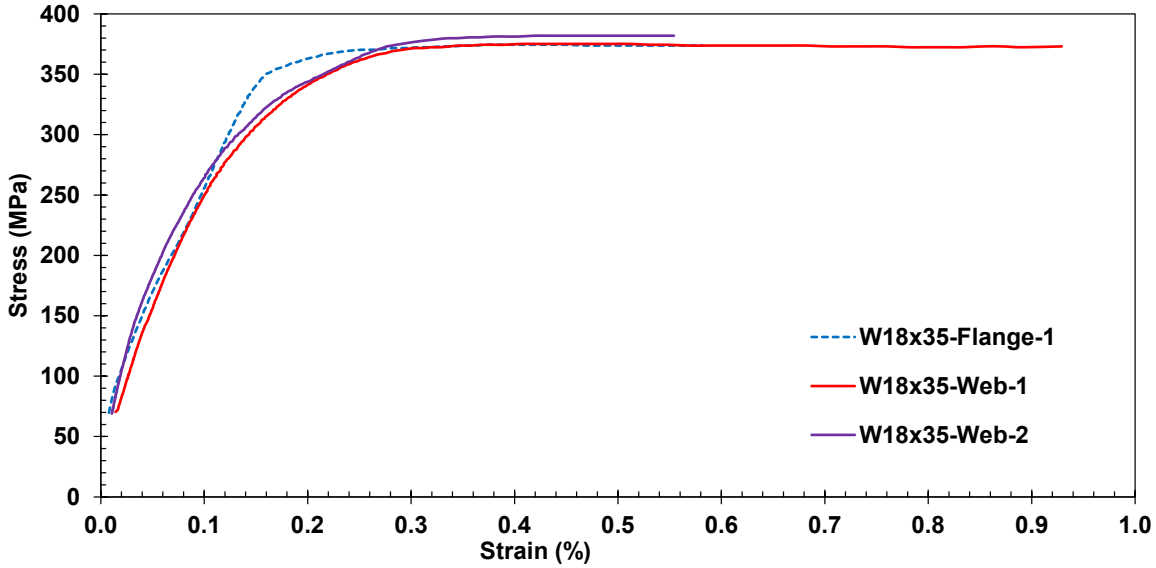

(b)

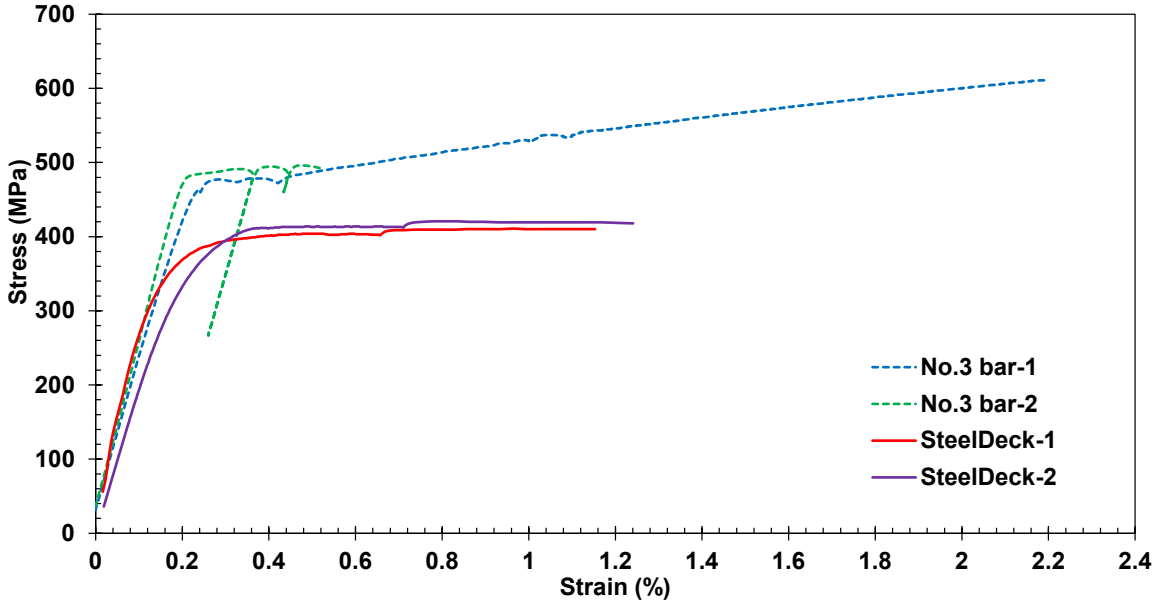
Stress (MPa)
Strain (%)
No.3 bar-1
No.3 bar-2
SteelDeck-1
SteelDeck-2

(c)

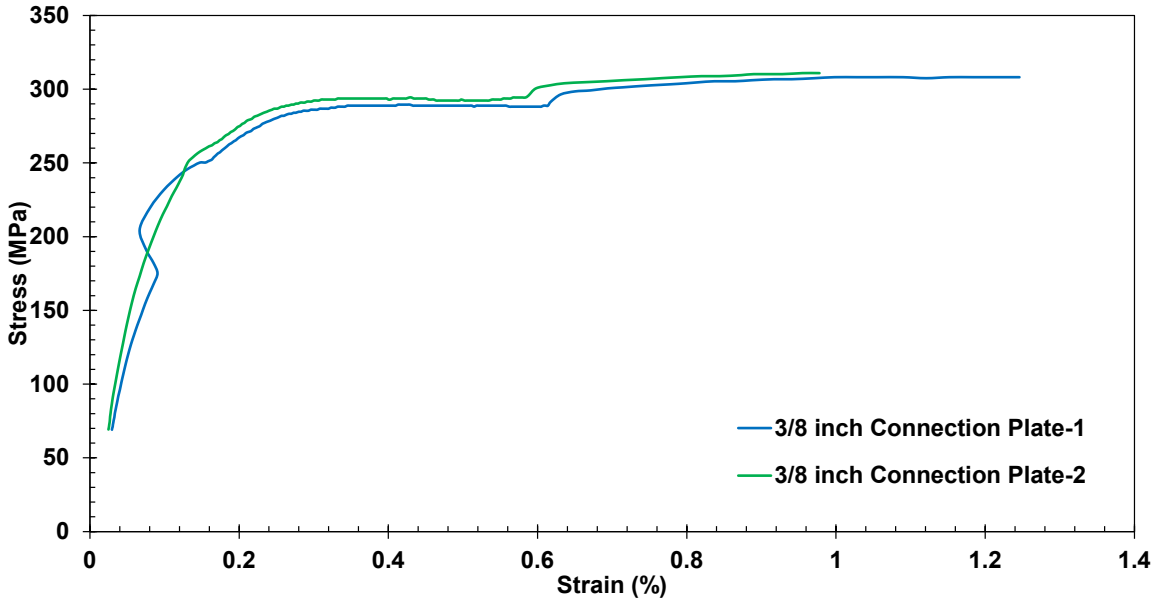
Stress (MPa)
Strain (%)
3/8 inch Connection Plate-1
3/8 inch Connection Plate-2

(d)

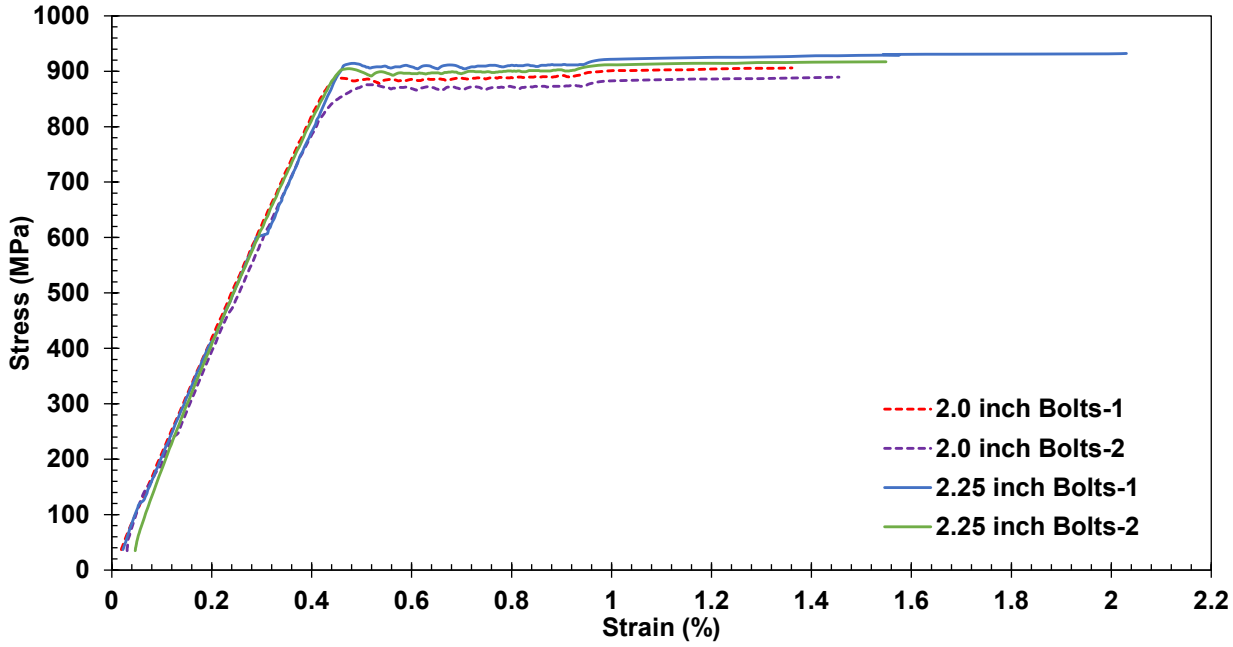

(e)

Fig. 78. Stress-strain curves of steel materials used in the test (a) W16×31 steel beams; (b) W18×35 steel beams; (c) No. 3 deformed bars and steel deck; (d) 3/8 inch plates used for standard and extended shear tab connections; (e) 2.0 inch long bolts used in standard shear tab connections and 2.25 inch long bolts used in extended shear tab connections.

A.13. Boundary Conditions at the Base of the Columns in the 2-story Test Frame

A total of twelve 7.34 m (289 in) tall W12×106 columns (ASTM A992 Grade 50 with a minimum specified yield strength of 50 ksi) were used in the two-story test frame shown in Fig. 4. Each W12×106 column had a 91 cm × 91 cm × 5 cm (36 in. × 36 in. × 2 in.) steel plate (ASTM A572 Grade 50 with a minimum specified yield strength of 50 ksi) welded to the base of the column. These base plates were anchored to the strong floor using four 3.5 cm (1-3/8 in.) diameter high strength steel bars (DYWIDAG Grade 150 with a minimum specified tensile strength of 150 ksi) post-tensioned to 445 kN (100 kip) each.

A separate laboratory test, named "lateral stiffness of the column test", was conducted at the NFRL to define the boundary condition at the base of the W12×106 column as the boundary condition is needed to accurately model the test structure for computational modeling. It may also be used in the calculation of axial forces developed at the ends of the test bay beams during the test using the lateral deflections of the columns (refer to Appendix A.8) and strains measured near the base of the columns (refer to Appendix A.9) during the test.

Figure 79a shows the test setup used for lateral stiffness of the column test. The columns were anchored to strong floor simulating the same anchoring conditions used in the composite floor tests. The 5 cm thick base plates welded to the columns were anchored to the strong floor using four high strength bars post-tensioned to 445 kN (100 kip) each as shown in Fig. 79b. A servo-hydraulic actuator (Model: MTS 201.35TS) was used to apply lateral load in the strong axis of the column at a height of 159 cm (62.5 in.) above the base plates. The lateral deflections (v_L) of the columns were measured at the height (L) of 159 cm above the base plates as shown in Fig. 79a. The slip of the base plate during the lateral loading of the column was measured at the mid-height of the 5 cm thick plate, 2.5 cm above the strong floor (Fig. 79b).

Figure 80 shows the variations in displacement measurements with applied actuator load. During the test, first, tensile load in the actuator was gradually increased to 224 kN (50.36 kip) and then gradually decreased to zero. Then, compressive load was gradually increased to 268 kN (60.32 kip). The average slip measured a peak value of 0.07 mm (0.003 in.). Figure 81 shows the average lateral displacement after deducting the slip. It reached 16.7 mm (0.656 in.) at the compressive load of 268 kN (60.32 kip) and 13.3 mm (0.524 in.) at the tensile load of 224 kN (50.36 kip). As shown in Fig. 81, the gradient of the graph, that indicates the ratio of lateral load/lateral displacement, is 103.3 kip/in. (18.1 kN/mm). It is to be noted that the lateral stiffness of the column test was conducted only in the strong axis of the column (Fig. 79).

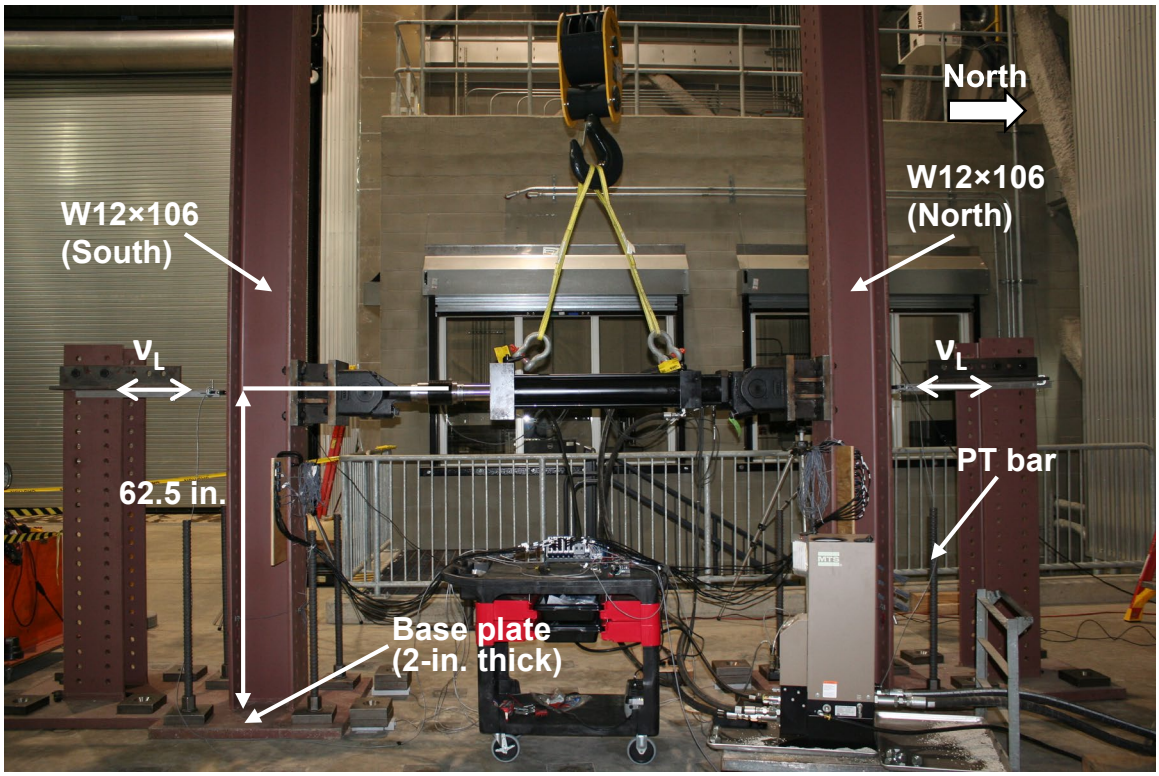

(a)

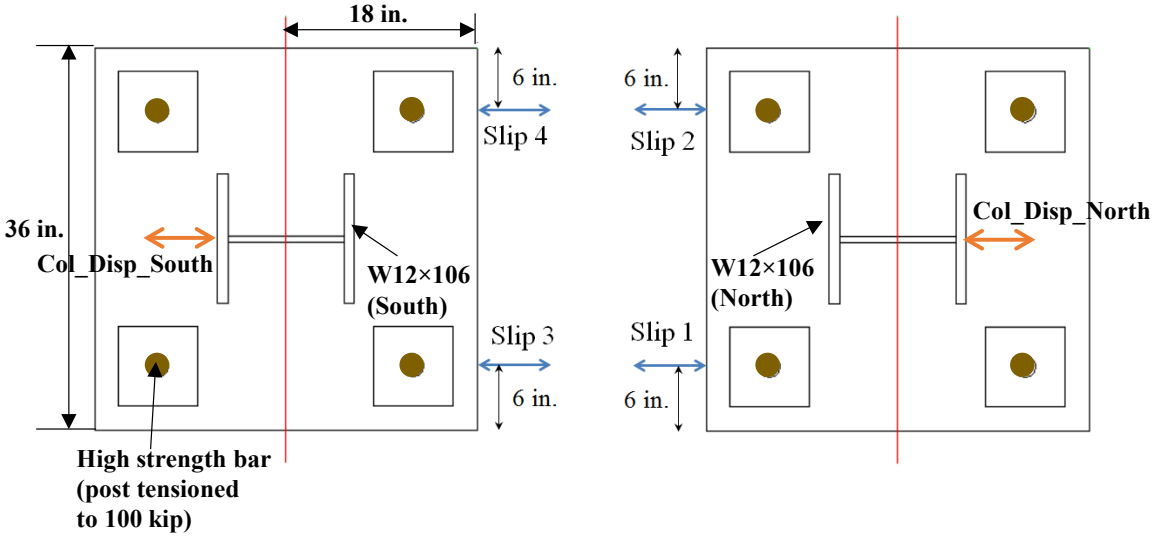

(b)

Fig. 79. Lateral stiffness of the column test: (a) test setup; (b) column base plates

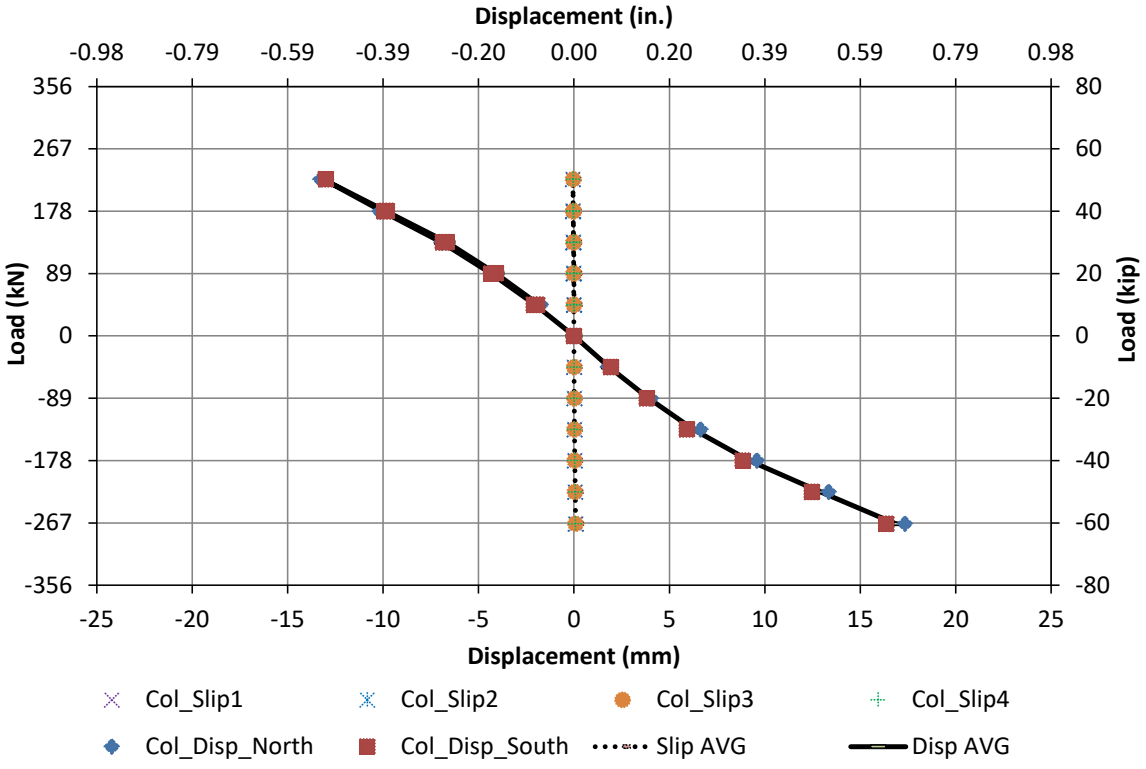

Fig. 80. Displacement and slip measurements-Lateral stiffness test

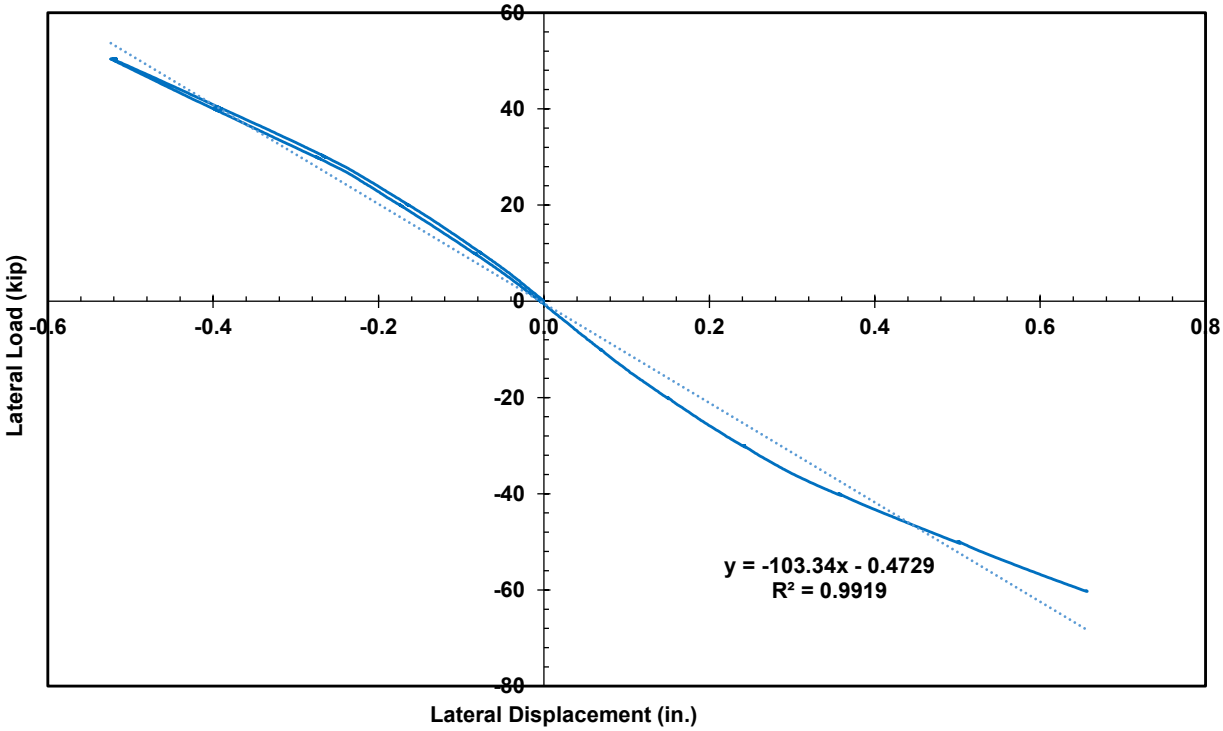

Fig. 81. Applied load vs average displacement-Lateral stiffness test

Calculation of rotational stiffness of the column base from the lateral stiffness test

For W12 x 106 column (from AISC Steel Construction Manual)

$I_x := 933\ in^4 \qquad I_y := 301\ in^4 \qquad E := 29000\ ksi$

From the lateral stiffness test of the column, the lateral stiffness in the strong axis (denoted by Ix) of the column at the height of 62.5 in. above the base plate,

$K_{cx} := 103.34\ \frac{kip}{in} \qquad L := 62.5\ in$

If the column is assumed to have fixed boundary condition at the base, the lateral stiffness would be

$$K_{x.fixed} := \frac{12 \cdot E \cdot I_x}{L^3}$$

$$K_{x.fixed} = \left(1.33 \cdot 10^3\right)\ \frac{kip}{in}$$

$K_{cx} < K_{x.fixed}$

$$\frac{K_{x.fixed}}{K_{cx}} = 12.869$$

This shows that fixed boundary condition cannot be assumed at the base of the column

Defining boundary condition at the base of the column

In order to define the boundary condition at the base, a rotational spring with a rotational stiffness of Kr is introduced at the base of the column.

The following assumptions are made for the calculation of rotational stiffness of the column base:

1. The stress-strain behaviors of the column and the base plate steel are in the elastic range during the test.
2. The base of the column can be represented by an elastic rotational spring so that the rotation is proportional to the applied moment at the base.
3. There is no moment transfer between the actuator and the column.

Figure 82 shows the applied and reaction forces on the column. "x" indicates the distance along the column above the base plate.

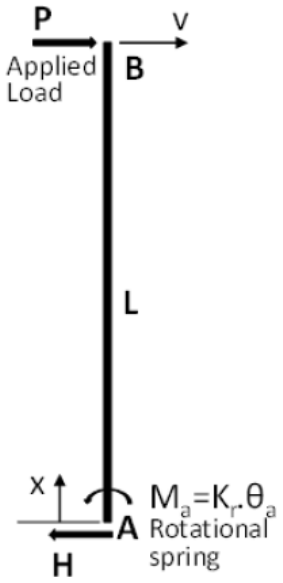

Fig. 82. Forces acting on column-Lateral stiffness test

For the forces acting on the column as shown in Fig. 82, Curvature-deflection equation

$$\frac{\mathrm{d}^2}{\mathrm{d}x^2}v=\frac{M}{E\cdot I}=\frac{P}{E\cdot I}\cdot(L-x)$$

Where, E=Young's modulus of steel;
I = Second moment of area

Slope-deflection equation

$$\frac{\mathrm{d}}{\mathrm{d}x}v=\frac{P}{E\cdot I}\cdot\left(L\cdot x-\frac{x^2}{2}\right)+C_1$$

Where, C_1=a constant

Deflection equation

$$v=\frac{P}{E\cdot I}\cdot\left(\frac{L\cdot x^2}{2}-\frac{x^3}{6}\right)+C_1\cdot x+C_2$$

Where, C_2=a constant

Boundary condition, at x=0, v=0

$$C_2=0$$

Boundary condition, at x=L, v=v_L

$$v_L=\frac{P}{E\cdot I}\cdot\left(\frac{L^3}{3}\right)+C_1\cdot L$$

$$C_1=\frac{v_L}{L}-\frac{P\cdot L^2}{3\cdot E\cdot I}$$

Slope-deflection equation

$$\frac{\mathrm{d}}{\mathrm{d}x}v=\frac{P}{E\cdot I}\cdot\left(L\cdot x-\frac{x^2}{2}\right)+\left(\frac{v_L}{L}-\frac{P\cdot L^2}{3\cdot E\cdot I}\right)$$

Eq.(1)

Deflection equation

$$v=\frac{P}{E\cdot I}\cdot\left(\frac{L\cdot x^2}{2}-\frac{x^3}{6}\right)+\left(\frac{v_L}{L}-\frac{P\cdot L^2}{3\cdot E\cdot I}\right)\cdot x$$

Eq.(2)

Boundary condition, at x=0, dv/dx=θa , M=Ma

$$\theta_a = \frac{v_L}{L} - \frac{P \cdot L^2}{3 \cdot E \cdot I}$$

$$M_a = K_r \cdot \theta_a$$

$$K_r = \frac{M_a}{\theta_a}$$

Rotational stiffness of the column base

$$K_r = \frac{P \cdot L}{\left(\frac{v_L}{L} - \frac{P \cdot L^2}{3 \cdot E \cdot I}\right)} \qquad \text{Eq.(3)}$$

Re-arranging the equation provides

$$P = \left(\frac{v_L}{L} - \frac{P \cdot L^2}{3 \cdot E \cdot I}\right) \cdot \frac{K_r}{L}$$

$$P = \left(\frac{K_r}{L^2 + \frac{K_r \cdot L^3}{3 \cdot E \cdot I}}\right) \cdot v_L$$

$$P = K_c \cdot v_L$$

Where Kc= Lateral stiffness of the column

Lateral stiffness of the column at height L

$$K_c = \left(\frac{K_r}{L^2 + \frac{K_r \cdot L^3}{3 \cdot E \cdot I}}\right) \qquad \text{Eq.(4)}$$

Rotational stiffness of the column base in terms of lateral stiffness of the column at height L

$$K_r = \left(\frac{K_c \cdot L^2}{1 - \frac{K_c \cdot L^3}{3 \cdot E \cdot I}}\right) \qquad \text{Eq.(5)}$$

From the lateral stiffness test, for L=62.5 in, in the strong axis of the column

$K_{cx} = 103.34 \ \frac{kip}{in}$ $L = 62.5 \ in$ $E := 29000 \ ksi$ $I_x = 933 \ in^4$

Rotational stiffness of the column base, from Eq.(5)

$$K_{rx} := \left(\frac{K_{cx} \cdot L^2}{1 - \frac{K_{cx} \cdot L^3}{3 \cdot E \cdot I_x}}\right)$$

$$K_{rx} = \left(5.857 \cdot 10^5\right) \ kip \cdot in$$

$$K_{rx} = \left(6.618 \cdot 10^4\right) \ kN \cdot m \qquad \text{(in SI units)}$$